Contactless Heat Measurement System for Retinal Coagulation

Design and Evaluation

Lisa Grooten

Delft University of Technology

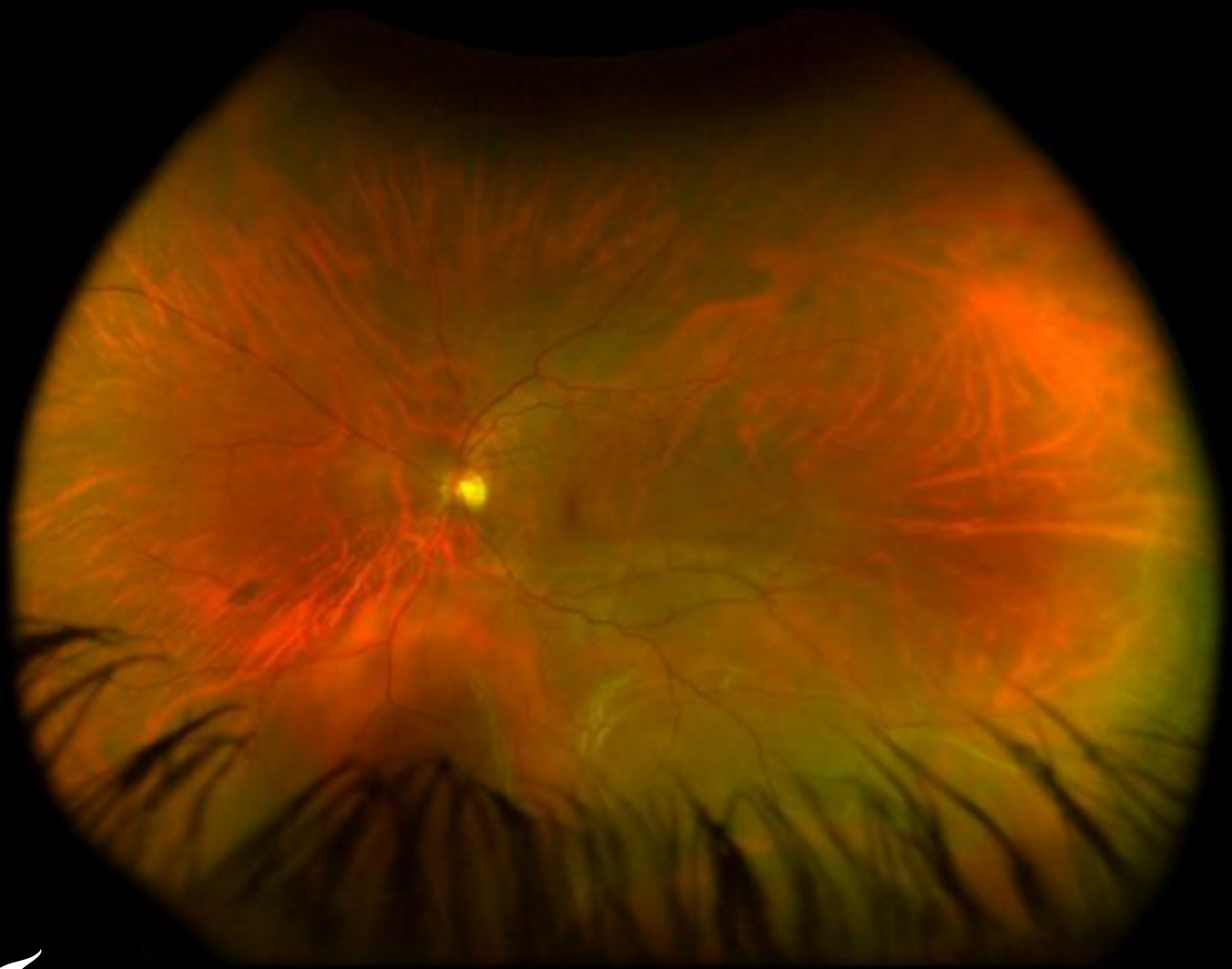

TU Delft

Contactless Heat Measurement System for Retinal Coagulation

Design and Evaluation

by

Lisa Grooten

in partial fulfillment of the requirements for the degree of

Master of Science
in Biomedical Engineering

at the Delft University of Technology,
to be defended publicly on Tuesday August 16, 2022 at 9:30 A.M.

Student Number	4501373
Examination committee:	Dr. D. Dodou, supervisor
	Prof. Dr. B.H.W. Hendriks
	Ir. P.D. Robertson
Faculty:	Faculty of Mechanical, Maritime and Materials Engineering, Delft

Cover: Retinal detachment, figure adapted from [1]

TU Delft

Design and Evaluation of a Contactless Heat Measurement System for Retinal Coagulation

L. Grooten
Student Number: 4501373
Biomedical Engineering, Delft University of Technology

***Abstract*—*Introduction:* Current heat measurement systems for retinal coagulation are insufficient to demonstrate the safety of intraocular diathermy instruments. Therefore, this paper aims to design and test a novel coagulation heat measurement system that attempts to infer direct retinal tissue temperature using contactless thermal measurements. *Methods:* In four experiment conditions, the direct temperature on the lower surface of the tissue is measured from below with a thermography camera measuring the temperature through a semi-transparent window that holds the tissue, and contactless measurements are made with a multi-sensor containing vertically aligned micro sensors located in the fluid medium above the sample. *Results:* The lowest mean temperature increase at both the thermography measurements (1.52°C) and sensor measurements (0.08°C), is found in the condition of 2.2 J (2.2 W and 1"). At thermography, the highest mean increase (8.67°C) resulted from the condition of 4 J (4 W and 1") and positive. At the sensor, the highest mean increase (0.25°C) is found in the condition of 4 J (2 W and 2"). *Discussion:* The use of 2.2 J appears too low for proper sensor measurement. For the two conditions of 4 J there is a contradictory indication of the influence of application time in thermography measurements versus sensor measurements, as the sensor is expected to be more sensitive to changes in the application time than the thermal camera. *Conclusion:* Since no similar trends have been observed between the thermography and multi-sensor measurements, the contactless sensor cannot infer the direct tissue temperature.**

***Index Terms*—Coagulation, Diathermy, Electrosurgery, Intraocular, Retina, Sensor, Temperature, Thermography**

I. Introduction

In electrosurgery, electrocoagulation results from the passing of radio frequency alternating electrical current through tissue. The surgical effect of electrocoagulation, which is defined as "the tissue is heated below the boiling point and undergoes thermal denaturation" [1, Tab. 1], is used to achieve hemostasis, which is the control of vessel bleeding.

Following Joule's law of heating, depicted in Equation 1 [2, p. 256], the heat generated (Q) for tissue denaturation depends on the resistance of the conductor (R), the current density (J) and the current duration (t). This heating effect was initially defined as diathermy in 1923 [3].

$$Q = J^2 \times t \times R \tag{1}$$

During vitreous surgery, a surgery whereat vitreous humour is removed from the eye by vitrectomy using a laparoscopic cutting instrument, vessel bleeding in the retina can occur [4]. The retina is the internal light-sensitive layer at the back of the eye. To stop active bleeding during vitreous surgery, an intraocular diathermy probe is applied on the bleeding vessel [5], as shown in Figure 1.

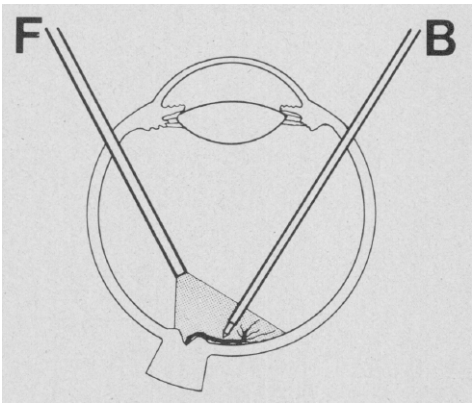

Fig. 1. Diathermy application with bipolar probe (B) and assisting fiber optic probe (F). Figure adapted from [5]

The intraocular diathermy instrument was initially developed as a monopolar system. As this configuration led to two cases of sight loss due to damage to the optic nerve [6], a bipolar probe was developed and implemented in 1983 [4]. To date, no changes have been implemented in the clinical use of the bipolar diathermy probe.

Figure 2 depicts the denaturation spots that result from a study by Van Overdam et al. [7], where the conventional diathermy probe is tested on perfluorodecalin perfused porcine cadaver eyes, with an ex-vivo open-sky approach (n=5). At this approach, open-sky implies that the cadaver eyes are are cut open from above and that the cornea, the lens and the vitreous humour are removed. This results in a clear open surgical site of the retina, as can be seen in Figure 2. In this figure, at the retinal vein (v), it can be seen that there is only blood flow until the denaturation spot. The perfluorodecalin only flows after the denaturation spot. This indicates that the coagulation has been succesfull. However, in the artery (a), the blood can still pass through the coagulation spot, indicating that this was an unsuccessful diathermy attempt. Results of all tests in that study with the conventional diathermy probe showed closure rates of 60% and 80% at the inferior retinal artery and the inferior retinal vein, respectively [7]. The authors argued that unsuccessful coagulation occurs because the diathermy probe can only coagulate vessels from one side. Moreover, it blocks the surgeons' view, since the probe tip is situated between the retina and the surgeon view [7]. The authors also suggested the need for a new intraocular diathermy instrument in an

earlier study, where the diathermy probe could completely shut engorged vessels [8].

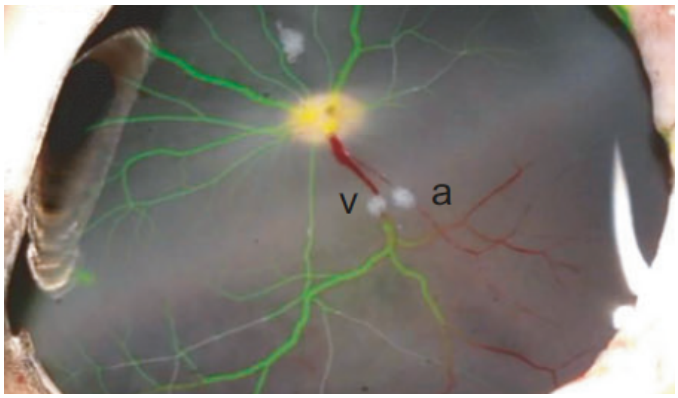

Fig. 2. Unsuccessful coagulation on retinal artery (a) and successful coagulation on retinal vein (v) in perfused porcine cadaver eye after diathermy with conventional bipolar probe. Figure adapted from [7]

In an attempt to provide mechanical compression at both sides of vessels and avoid instrument exchange, an intraocular diathermy forceps has been recently developed by modifying a peeling microforceps into a bipolar instrument [7]. Figure 3 depicts a cross-section of this instrument.

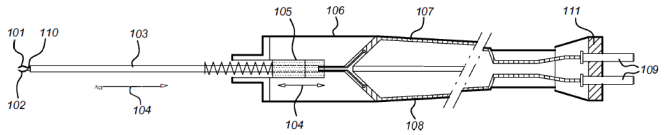

Fig. 3. Cross-section of intraocular diathermy forceps configuration. Adapted from [9]

Although patented and tested in an animal cadaver study (n=5) as well as in a clinical trial (n=5) resulting in a vessel closure rate of 100% [9, 7, 10], this instrument has not been introduced to the clinical market yet. One reason is that the safety of the instrument must still be validated, which can be done by means of thermal measurements.

At histological test methods, thermal spread is inspected visually on thermally-induced changes in cell and tissue morphology, spread away lateral from the actual heating location [11]. Hence, heat can be used as indicator for thermal damage, which can be used for validation of this new intraocular diathermy forceps. Therefore, there is need for a new heat measurement system.

The validation and recertification of new and existing instruments has a high priority nowadays and in the upcoming years, because of the entry of the new Medical Device Regulation (MDR) for which existing instruments must be recertified and new products must comply with the MDR [12]. This indicates that other instruments and developments could potentially benefit from a new heat measurement system as well.

In this new heat measurement system, a piece of retinal tissue from porcine eyes could be used as a test model of the human retina each time this system is used to validate an instrument. However, it is difficult, time consuming, and material demanding to separate and collect the retina on a sample. This retina test model can be used once to measure the thermal effects directly on the retinal tissue. To keep the retinal tissue intact and to keep the future possibility to use an altered version in an in vivo clinical setting in mind, an additional contactless thermal measurement which not interferes with surgical instruments used during diathermy, is preferred.

Hence, the aim of this thesis is to investigate whether and to what degree contactless heat measurements can be used to infer what thermal effects are arising at the coagulation site of a diathermy probe inside the eye.

For this purpose, a measurement system is developed and a series of in vitro measurements are conducted in which the correlation between contactless thermal measurements and the direct temperature in porcine retinal tissue is systematically investigated as a function of the distance of the thermal measurements from the coagulation site on the tissue.

A new thermography method is applied for the direct temperature measurement in this system, which measures the retinal temperature of its lower surface. The contactless thermal measurements are realized with a series of vertical micro sensors which measure fluid temperature above the retinal coagulation site.

A. Background Information

Literature which gave rise to the aim of this thesis is included in this section. This literature originates from a narrative literature review on the electrical engineering challenges of the intraocular diathermy forceps, conducted prior to this thesis (included here). Other contributions to the formation of the thesis aim and the project definition can be found in Appendix A.

1) Monopolar and Bipolar Intraocular Diathermy Probe: The conventional instrument used for the coagulation of vessels in the retina during intraocular surgery is the bipolar diathermy probe. Before the use of this bipolar instrument, a monopolar configuration was used which was introduced in 1974 by Parel et al [13]. In their approach, a simple metallic tube which is insulated except from the tip, is connected to the handle of a radio frequency (RF) unit. Subsequently, the tip acts as a monopolar electrode which emits RF electromagnetic waves. These waves travel through the body medium as return path back to the diathermy unit, while diathermizing nearby vessels directly [13].

The design of the bipolar diathermy probe was established by Parel et al. in 1983 [4]. The probe consists of an active platinum inner electrode core with a glass coaxial insulation layer around it, which allows for an outer coaxial electrode layer. In this case the return electrode is made of stainless steel. Except for the distal end, the probe tip has an additional surrounding layer of matt Teflon coating. At the distal end, the probe tip is conically shaped [5]. During diathermy, the produced current will flow from the emitting electrode towards the nearby located coaxial return electrode [4], which emits more directed RF waves. Currently, clinically used bipolar probes are still based on this bipolar configuration, but can differ in material, tip design, and reusability.

Figure 4 depicts a reusable diathermy probe. In addition to reusable probes, disposable designs are also used clinically. A probe similar to the bipolar probe of the company Kirwan Surgical Products [14] (depicted in Figure 5) is used in the experiment of this thesis. It consists of a stainless steel wire that is circumferentially insulated and surrounded by an outer stainless steel conducting tube, except from the distal end of the tip. Two energy connector terminals are located at the proximal end of the plastic exterior harness [15].

Fig. 4. Conventional diathermy probe (DORC, the Netherlands). Adapted from [16]

Fig. 5. Disposable bipolar probe (Kirwan Surgical Products, US). Adapted from [14]

II. Materials and Methods

In this section, the development, working principle, and validation of the measurement system are described, after which the materials and methods of the experiment are provided. Finally, the methods used for data analysis are described.

A. Development of the Thermal Measurement System

The measurement system has two parts: one that can measure temperature increase contactless at a specific distance from the retina in a test environment that emulates the surgical environment and another that can measure temperature increase directly in retina tissue itself; the temperatures at the two locations are then compared. Hence, the design of the measurement system can be divided into the direct tissue temperature measurement method, the design of the system environment, and the contactless temperature measurement method. The measured temperature increase is induced by coagulation of vessels inside the retina tissue using a disposable diathermy probe of of the company Bausch+Lomb, which is similar to the probe shown in Figure 5.

For the design of the subsystems, we consulted the following theory regarding heat measurements and eye anatomy.

At thermography, the distribution of surface temperature is used to inspect structural damage beneath the surface. This is often done with an infrared (IR) thermal camera which can measure surface temperature without direct contact [17]. It can also be performed in real time, but only during in situ surgery [18].

There are several infrared wave bands including short-wave infrared (SWIR), mid-wave infrared (MWIR), and long-wave infrared (LWIR) [19]. The wavelength ranges of these bands are 1-3 µm, 3-5 µm and 8-14 µm respectively. A FLIR E96 thermal camera operates in a spectral range of 7,5-14 µm. This camera has a thermal resolution of 640 by 480 pixels and an accuracy of 2% of the reading[20].

Dodde et al. [21] introduced another solution for measuring thermal spread in real time using thermistors placed on the electrosurgical instrument. Thermistors only depend on their own resistance, so no additional imaging or measurement instrumentation is needed. Therefore, the authors argued that they can also provide real-time data during laparoscopic surgery [21]. The resistance of a thermistor changes when its temperature changes, so it is a temperature-dependent resistance. The high change in resistance with temperature allows for a highly sensitive measurement [22, 23].

The dimensions of the human eye are used for several assumptions of the measuring systems. Figure 6 displays the inner eye dimensions measured by Hooge et al. [24]. They indicate that the inner width in the transverse horizontal plane is 22.91 mm and that the depth of the eye in the axial plane is 23.58 mm. The depth from the front side of the lens to the internal back of the eye is 19.98 mm [24].

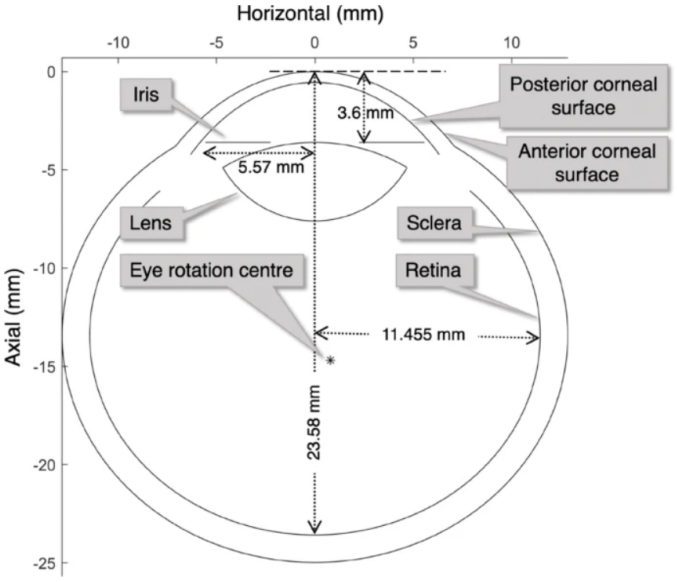

Fig. 6. Variations in retina thickness of the human eye. Figure adapted from [24]

The thickness of the retina varies, as can be seen in Figure 7. It is 0.320 mm thick at the foveal rim. At the foveal floor, the thickness is the lowest and ranges between 0.150 and 0.200 mm. The thickness of the other portion of the retina ranges from 0.120 mm to 0.280 mm [25]. The fovea is located in the center of the macula, which is also known as the yellow spot. The fovea center is avascular [26] and the vessel density at the macula is almost zero [27].

B. Tissue Temperature Measurement Method

For the direct tissue temperature measurement subsystem, we designed a method which measures the temperature of the retina during coagulation, while maintaining space for the contactless measurement of the same retina sample.

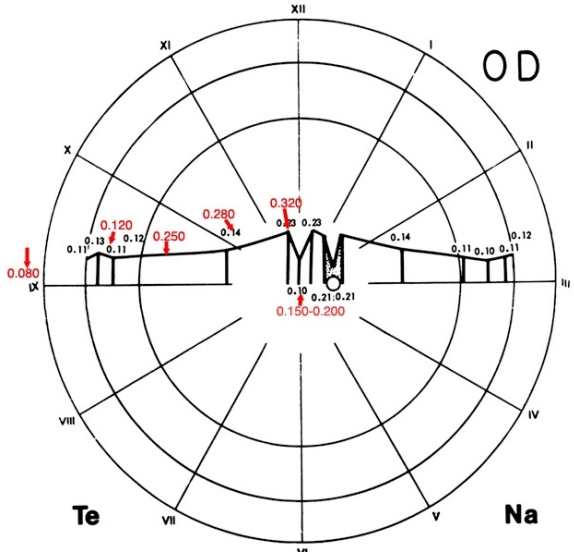

Fig. 7. Variations in retina thickness of the human eye. Figure adapted from [25]

The limitations of the Riemens study (described in section I) indicated that if a thermal camera were to be placed above a retina sample, the retina sample must be flat and the covering fluid layer must be kept to a minimum, to obtain accurate thermography data. In this case, there is no option to add an additional contactless temperature measurement system, because this would block the detection field of the thermal camera. Hence, we explored a different orientation of the thermal camera than from above.

Assuming that the temperature passes directly through the retina tissue during coagulation, since it has a small thickness, the tissue temperature could be measured with a thermal camera from below the retinal surface, rather than from the upper surface at which diathermy is applied. Because diathermy is only applied at vessels, and the macula and foveo are free from vessels, we assumed that the retina is only coagulated on regions where the retina has a maximum thickness of 250 µm.

1) Working Principle Lower Thermography Method: We realized this lower thermography method by placing a thermal camera beneath a window, which holds the retina sample, and measure the temperature through this window. This provides an empty space above the sample for the upper contactless temperature measurement system to be situated.

The working principle of the lower thermography method is based on the optical transmission rate of the material of the window on which the retina sample is placed. The material of the window is semi-transparent to IR waves in the spectral range of the thermal camera, so a large portion of the IR waves which radiate from the lower surface of the retina sample travel through the window and can be detected and converted to temperature by the thermal camera, as illustrated in Figure 8. The transmission rate of the window determines the portion of IR waves which can travel through the window.

2) Material of the Window: As the FLIR camera has a spectral range of 7.5-14 µm, a window with high transmittance

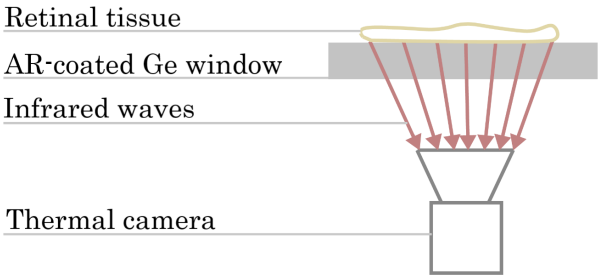

Fig. 8. Working principle of lower thermography method.

in the LWIR range was needed. Additional criteria for the choice of window material were that the window must be resistant to fluid for at least 12 hours, should not deform or break when fluid is deposited or when the window is removed from the test environment, should not have a high thermal expansion property and should have a minimum transmission rate of 85%.

Based on these criteria, we chose a germanium (Ge) window containing an anti-reflection (AR) coating with an apparent transmission rate of 90% in a spectral range of 8 to 14 µm. This AR-coating enhances the permeability of IR waves and makes the high transmission rate possible, since an uncoated Ge window only has a maximum transmission of 50% [28]. The complete selection process of this window and the exclusion of other materials can be found in Appendix B.

3) Window Correction Factor: Because not all IR waves can pass the window, the IR waves detected by the thermal camera must be corrected. In practice, the thermal camera correction factor differs from the apparent transmission rate of the window (90%).

A first simple test was conducted in attempt to determine the actual correction factor of the window. In this test, the temperature of a paper cup with electrical tape on the outer surface, filled with hot water, is measured. Figure 9A shows an example of the thermal images that are acquired during this test. The temperature difference before and after applying a correction factor in the thermal camera and placing the window in between the cup and the thermal camera, is noted for different correction factors. A detailed description of the test steps can be found in Appendix C. The test with the E96 thermal camera resulted in the lowest mean temperature difference, between the moment before window application and after window application, of 0.08 ± 0.10°C (n=4) at a factor of 90%. The test with the E75 thermal camera resulted in the lowest mean temperature difference of 0.13 ± 0.17°C (n=7) at a factor of 89%. A more detailed description, among other transmission factor results of this test, can be found in Appendix D. The two cameras result in a different correction factor. Additionally, in the time period that the factor is set in the camera, the actual temperature of the water can be decreased. Therefore, we performed a second test using a camera and a constant water temperature.

At this second test, the temperature of the water is kept constant using a heating magnetic stirrer. For this purpose, the water is heated slowly and stirred by the magnetic stirrer.

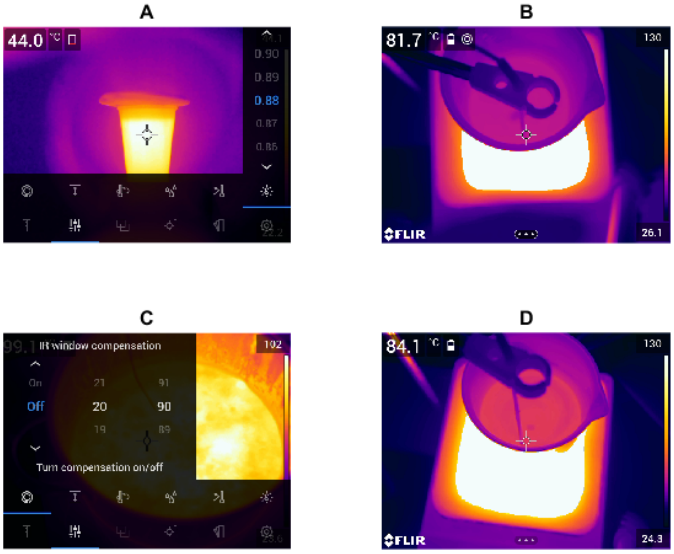

Fig. 9. Thermal image frame of first (A), second (B), third (C) and fourth (D) test to determine the correction factor and to validate the lower thermography method

In this way, the water should reach a constant and evenly distributed temperature when stabilized around the set temperature. In this test, which setup is displayed in Figure 10, the thermal camera is pointed at the water surface and the temperature of the center point of the thermal camera is shown on the thermal image frames (see Figure 9B). The temperature values are obtained from the thermal image frames using optical character recognition. During acquisition, the window is placed between the camera and the water surface, and different correction factors are applied to the thermal camera. Although the set temperature is set at 100°C, the temperature of the water heated to 84°C, cooled back to 80°C, and varied between this temperature range with a slow rate. A factor of 88% resulted in the least mean temperature difference of 0.27 ± 0.20°C (n=6) between 25 measurements before window application and 25 measurements after window application. A detailed description of the method and results of this test can be found in Appendix D.

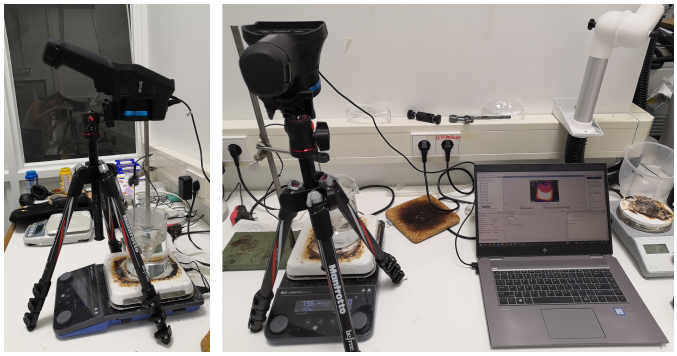

Fig. 10. Experiment setup of second test with heating magnetic stirrer

A third test is performed to verify whether a correction factor of 88% provides the most accurate heat measurements. In this test, water is heated to the boiling point, to create a reference temperature which is exactly 100°C. The test setup, as shown in Figure 11, consists of a hot water-filled cooking pan placed on an induction hob. Three window factors (88%, 89% and 90%) are tested with the same method as the second test using the heating magnetic stirrer described earlier. During the test, the boiling point of the water could not be determined because the water was not evenly heated and the bubbling formation started in a round pattern above the electrical heating element. This also leads to highly fluctuating temperature measurements. Furthermore, when the temperature is above 100°C, the thermal image frame (see Figure 9C) only displays rounded numbers which affected the results of this test. This test also indicated that 88% is the most fitting factor.

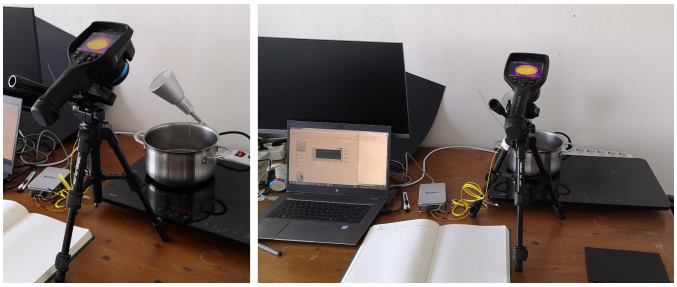

Fig. 11. Experiment setup of third test with boiling water

The high mean temperature difference of 1.06 ± 0.40°C (n=6) between 25 measurements before window application and 25 measurements after window application with a factor of 88%, together with affected results due to varying temperature and inaccurate measurement above 100°C, indicates that this test cannot validate that the lower thermography method provides accurate temperature. Nevertheless, because the test with the heating magnetic stirrer also indicated that 88% provides the most accurate temperature measurements, this factor was used as the window correction factor in the experiment of this thesis.

4) Validation of Lower Thermography Method: To validate the lower thermography method with a window correction factor of 88%, a fourth test is performed using the heating magnetic stirrer. Because this test is performed using the same test setup as the second test using the heating magnetic stirrer, the setup depicted in Figure 10 is used and the water is heated to 84°C, cooled back to 80°C and varied in between this temperature range with a slow rate. In this fourth test, an external thermometer inside the water is used to compare the water temperature with the water surface temperature measured with the thermal camera.

During the fourth test, the window is placed between the thermal camera and the water surface and the correction factor of 88% is applied to the thermal camera. At time periods at which the external temperature did not change, we measured the surface temperature at the center point of the thermal camera, which can be seen in Figure 9D.

Of each acquisition, the mean thermography temperature (T_t) of all thermal image frames in the period where the

TABLE I
RESULTS THERMOGRAPHY VALIDATION EXPERIMENT

#	T_e [°C]	$\bar{x}$ ± SD T_t [°C]	ΔT [°C]	T_a [°C]	FLIR Type	LOC_e [W,H]*	Center Distance [Δ,Δ]
1	83.20	83.75 ± 0.52	0.55	27	E75	311,251	10,-10
2	83.50	84.10 ± 0.50	0.60	29	E75	315,239	6,2
3	84.00	84.03 ± 0.54	0.03	29	E75	265,307	56,-66
4	83.90	83.96 ± 0.57	0.06	27	E75	265,307	56,-66
5	82.40	83.45 ± 1.11	1.05	27	E96	324,241	-3,0
6	82.40	83.56 ± 0.99	1.16	27	E96	286,254	35,-13
7	81.50	83.70 ± 0.84	2.20	29	E96	277,258	44,-17
8	81.30	83.46 ± 1.25	2.16	29	E96	313,243	8,-2

* Left upper corner is pixel 1,1.

external temperature does not change is shown in Table I. This table also includes the external thermometer temperature (T_e), the difference between this value and the thermal and the mean surface temperature of the thermal camera (Δt), the ambient temperature setting of the thermal camera (T_a), the thermal camera type (FLIR type), the location of the external thermometer (LOC_e) and the distance of the center point from the external thermometer (center distance).

The results of this test show that at acquisitions 2 and 4, the surface temperature is close to the external thermometer temperature (temperature differences of 0.03°C and 0.06°C). The temperature difference at the remaining acquisitions differ from 0.55°C to 2.16°C. These large differences can be explained by the fact that the depth of the external thermometer varies during the tests. As can be seen in Figure 12, the vertical thermometer position is close to the water surface during acquisition four (Figure 12A). At acquisition five, the thermometer is positioned lower (Figure 12B) and at acquisition seven, the thermometer is at the lowest (Figure 12C). This height difference is because, during the test, the thermometer is manually lowered to compensate for the decreasing water height due to water evaporation. This lowering is not done to equal positions below the water surface. As the mean surface temperature remains similar (83.75 ± 0.26°C), it is expected that the lowering of the external thermometer creates the greater temperature difference at acquisitions 5 to 8.

The distance of the center point of the camera to the external thermometer does not seem to affect the temperature measurements. Because there are too many changing variables in this test, the large temperature difference cannot be fully explained. However, as the height of the external temperature at acquisition four is the closest to the water surface, it can be concluded that this acquisition provides the most accurate validation of the lower thermography method. Therefore, we can conclude that the lower thermography method can measure the surface temperature with an accuracy of 0.06 ± 0.54°C.

The script 'StirrerValidation.m' provides all the results of the this fourth test and can be downloaded via this link.

C. Test Environment Design

To perform an experiment with the lower temperature measurement method and to add an upper contactless measurement method, we designed a test environment which provides experiment conditions close to the surgical setting.

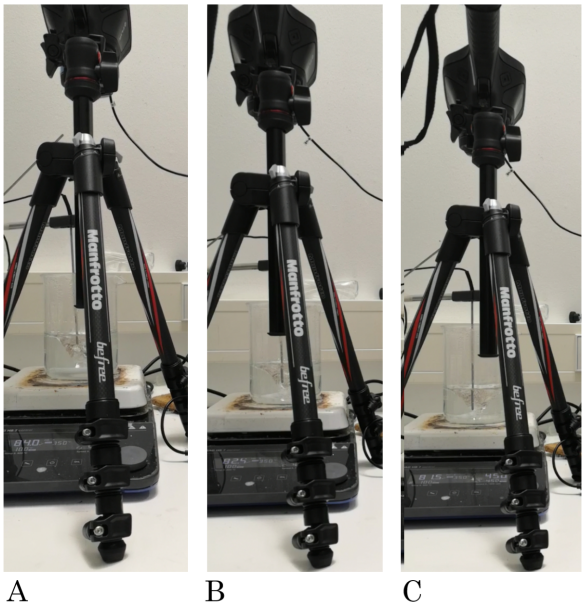

Fig. 12. Thermometer depth at test 4 (A), test 5 (B) and test 7 (C)

This section contains a description of the test environment in addition to the design of the test box, which combines the lower and upper temperature measurement methods into one measurement system.

1) Test Environment: Several design choices of the test environment are based on the dimensions of the human eye and the surgical setting of vitreous surgery, at which diathermy is applied. Perfluorodecalin (Decalin), a heavy liquid, can be used to stabilize and unroll the detached retina during this surgery [29].

The retinal sample is a piece of porcine retina separated from a pig eye. This porcine retina is suited as a test model for the human retina because the porcine eye has a similar anatomy and vascular structure [30, 31].

In the test environment, the piece of retina sample is not fixed on the window. When a liquid, water for instance, is deposited on top of a loose piece of retina, it rolls up and floats to the liquid surface. This effect was observed during the preliminary studies of retina sample preparation, as described in section H. Therefore, the retina sample must be stabilized and unrolled when a liquid is deposited on top of it. In the test environment, heavy-liquid Decalin is used for this purpose.

As can be seen in the concept illustration of the measurement environment in Figure 13, the Decalin fluid is used as a medium through which the heat produced by the diathermy probe is transferred to the upper measurement instrument.

In order to create this Decalin fluid medium, the window of the lower thermography method containing the retina sample (see Figure 14A) is fixated to a hollow box using double-sided tape with the same box profile (see Figure 14B). This box also serves to connect the lower thermography method with an upper contactless temperature measurement method.

When fixed to the window (see Figure 14C), the box can contain the Decalin fluid medium. Because the height of the Decalin fluid used during vitreous surgery cannot be higher

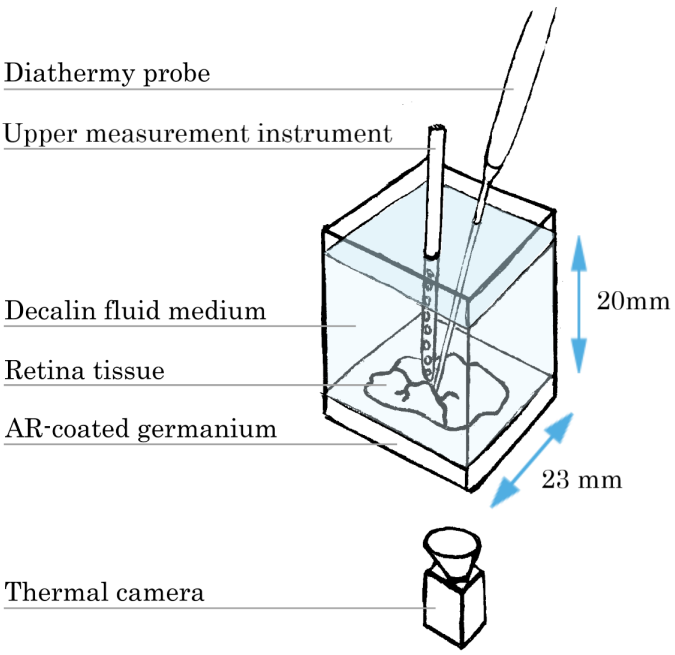

Fig. 13. Concept illustration of the measurement system

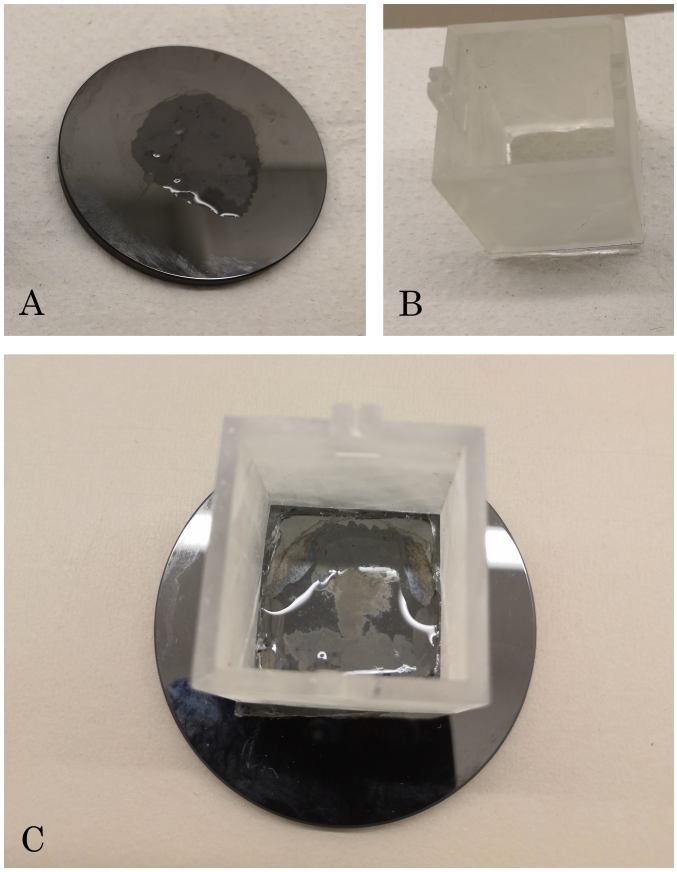

Fig. 14. AR-coated Germanium window containing a retina sample (A), the hollow test environment box (B) and the hollow box fixated on the window (C)

than the vitreous cavity, we based the height of the Decalin fluid medium (20 mm) on the depth from the lens to the internal back of the eye (19.98 mm).

Because Decalin is not heated to body temperature before insertion during vitreous surgery (Van Overdam, personal conversation, November 26, 2021), the Decalin fluid medium is not heated before the experiment either.

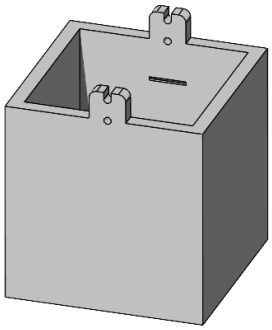

Fig. 15. Design of the hollow box

2) Hollow Box Design: Figure 15 displays the design of the hollow box that connects the two measuring subsystems. It is printed with resin using stereolithography, which is watertight [32].

The box has a hollow squared profile with inner dimensions of 23 mm*23 mm and a wall thickness of 2 mm. The inner dimensions are based on the width of the human eye.

In order to add the upper contactless measurement instrument, there is a hole and a guiding inlet at the same height on two opposite edges of the hollow box, with a diameter of 1 mm, to connect guide rods of the upper measurement instrument.

3) Upper Contactless Temperature Measurement Method: In order to define the correlation between this measurement system and the direct temperature in the retina as a function of the distance to the retina, the upper contactless temperature measurement method is developed. For this purpose, we designed a multi-sensor, with sensors at different vertical distances from the coagulation site.

In virtuous surgery, all instruments must fit through 23 gauge trocar cannulas that are placed through the eyeball [33]. To be able to use the sensors of the upper contactless measurement system, the sensors of each measure point should ideally be smaller than 0.6 mm so it may be used in future research where the sensor can to fit through the trocars as well.

Based on the benefits of thermistors, micro NTC (Negative Temperature Coefficient) thermistor sensors (denoted as sensors) with a maximum diameter of 0.5 mm are chosen for this purpose. The material of a sensor quickly takes up heat from the environment because of its small size. Therefore, the temperature of the sensor can be assumed to be representative of the surrounding temperature.

A multi-sensor is designed containing a vertical sensor array and an electrical module is designed to read these sensors,

translate it to temperature and to save the temperature data for further processing.

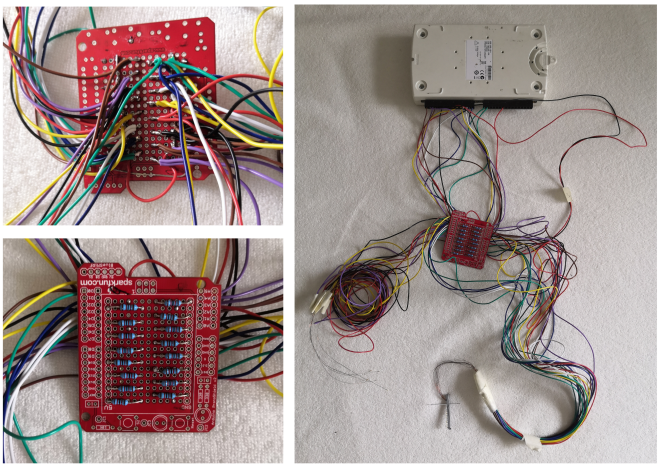

Fig. 16. Electronics of the multi-sensor

As can be seen in Figure 16, sixteen 12 kilo ohm resistors are soldered to the back side of the multi-sensor circuit board. On the front side of the circuit board, sixteen sensors are soldered to these resistors in series. In between each resistor and sensor, a wire is soldered, of which the other end is put into an analog port of an input module which can be connected to a USB port of a laptop or computer. Finally, a power input and output wire is soldered to the circuit and put into the module.

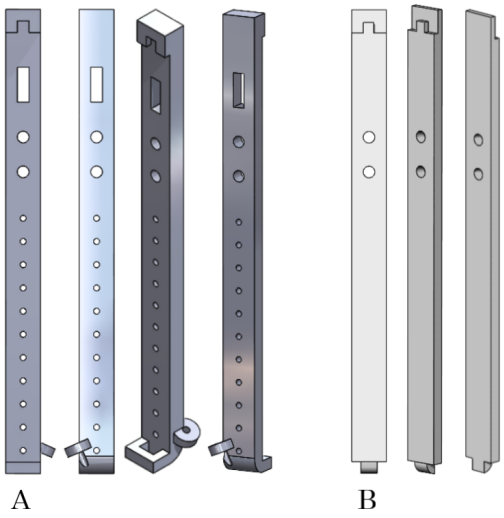

Fig. 17. Different views on design of the sensor holder (A) and back plate (B)

Eleven of the sensors, which have a diameter of 0.5 mm, are put through the guiding rectangle and placed in the holes of the polylactic acid 3D-printed holder that is displayed in Figure 17A. The sensors are vertically aligned with a distance of 2 mm between them, and the lowest sensor is located at a height of 2 mm above the bottom of the holder. The sensors are fixed in this holder by an additional back plate (Figure 17B), which can be hooked into the sensor holder part. To fixate the back plate to the holder, the tops are taped to each other with single-sided nano-grip tape. To complete the multi-sensor, two guide rods are inserted through the remaining two holes. During the experiment, the multi-sensor can be moved along these guide rods while maintaining a fixed vertical position. The upper guide rod has marked steps of 2 mm, so the coagulation position along the retina can be managed. These guide rods can be inserted in the holes and inlets of the hollow box to complete the test environment of the two measurement systems. As the guide rods must have a diameter less than 1mm, thin needles are used for this purpose. This results in the multi-sensor assembly displayed in Figure 18. Previous design iterations are described in Appendix E

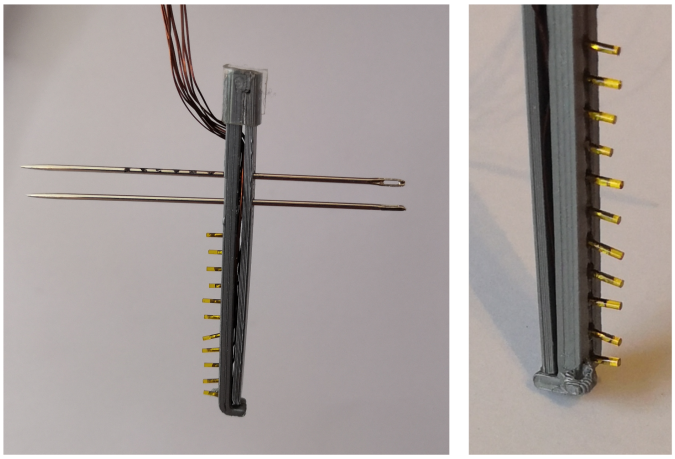

Fig. 18. Multi-sensor assembly

As can be seen in the technical drawing in Figure 19, the bottom of the sensor holder contains a ring with an inner diameter of 0.6 mm and is positioned at an angle of 23.57°. This ring guides the diathermy probe tip to a predefined position of 1.5 mm below the sensor holder on the vertical sensor axis. Hence, the distance between the lowest sensor and the intended probe tip at the coagulation surface is 3.5 mm. To move the probe to this position, the diathermy probe must lean against the edge of the hollow box wall, which is located 12 cm from the center of the hole of the upper guide rod. Hence, the diathermy probe guiding ring angle is based on this predefined position and the distance between the edge of the hollow box and the upper multi-sensor guide rod.

As the thickness of the holder is 1.5 mm in the sensor region and the sensors have a maximum length of 3.3 mm [34], the maximum portion of the sensors that is outside the holder is 1.8 mm. The location of the metal oxide head of the sensor, which is heated and changes in resistance during measurement, is within the portion of the sensor that is outside the holder, as is illustrated in Figure 20. This metal oxide head is connected to a Solid Nickel Bifilar wire (38 AWG) insulated with polyester. Together, the component is potted in a polyimide tube filled with epoxy resin [34].

There are five other sensors which are not cooperated into

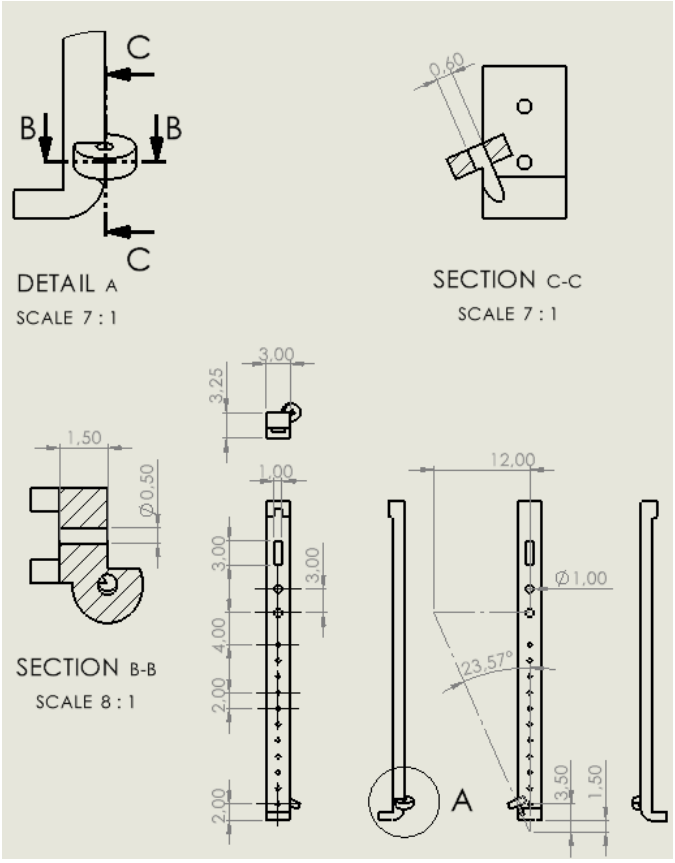

Fig. 19. Technical drawing of the sensor holder design

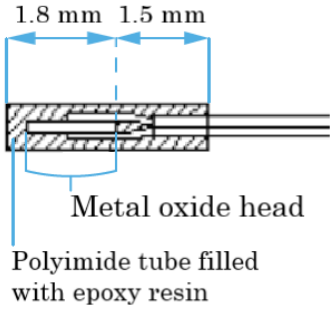

Fig. 20. Dimensions of inner components of NTC sensor. Figure adapted from [34]

the multi-sensor. These other sensors are used to create a reference sign to downsample the sensor data points to the thermography data points, for the identification of external noise, for Decalin fluid temperature check, and for air temperature measurement close to the setup. The latter is used to check whether visual temperature peaks in the sensor data were actually at the moment that the tissue was coagulated, during which the air temperature increases because of the presence and breath of the researcher in that area during coagulation.

4) Multi-Sensor Working Principle: In this section, the working principle of the sensors is described.

Before the sensors are soldered in series to the resistors, the evident resistance values of the resistors are measured. When operating, the voltage through the resistors on the circuit board is measured. These resistor voltage values are used as input of a calculation program in LabView software. In this program, the current through each resistor is calculated by dividing its measured voltage by its evident resistance. As the resistors and sensor are placed in series, the current through the sensors is equal to the current through the corresponding resistors. The module is tested on its output voltage, which is 10 volt. The voltage through the sensors is calculated by subtracting the measured resistor voltage values from the module output voltage. The remaining sensor voltage values through the sensors are divided by the corresponding calculated sensor current values, which gives the apparent sensor resistance values. These calculations are incorporated in the LabView program, which is included in Appendix F.

The resistance values correspond to temperatures from -40ºC to 125ºC [34]. In Figure 21, 17 of these temperature values between 18ºC and 58ºC are plotted against the corresponding resistance values. This temperature range is based on a realistic coagulation heat range (30.1ºC to 47.4ºC) that resulted in a study that evaluated thermal spread during intraocular diathermy [35]. To the plotted graph, a 3rd-order polynomial trend line is fitted. This function (displayed in Equation 2), with x as sensor resistance value, is implemented in the calculation program in LabView in order to compute the temperature of each sensor. The R-squared value of this function is 0.9995.

$$y = -0.0286x3 + 0.9719x2 - 12.889x + 85.454 \quad (2)$$

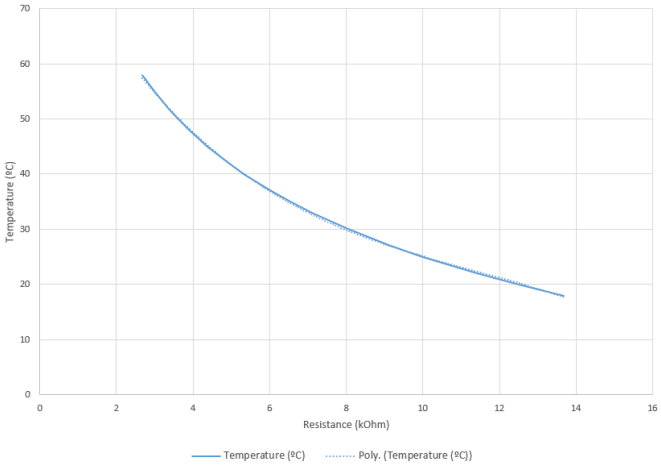

Fig. 21. Plot of sensor resistance values with corresponding temperature values (Temperature) and fitted polynomial trend line (Poly.). (Van Driel, personal communication, December 6, 2021)

The performance specifications of the sensors are shown in Table II. The resistance tolerance at a temperature of 25ºC is ± 0.2ºC and the time response in liquids is 200 ms [34].

5) Validation of Multi-sensor: To test the evident order of the sensors in the multi-sensor, we performed a test in which the sensors are cooled apart from each other, from the lowest sensor in the sensor holder to the highest sensor in the holder.

TABLE II
PERFORMANCE SPECIFICATIONS OF NTC SENSORS

Parameters	Units	Value
Resistance @ +25°C	Ohms	10,000
Resistance tolerance @ 25°C	°C	± 0.2
Alpha Value @ 25°C	%/°C	- 4.39
Beta Value 25/85	K	3976
Tolerance on Beta Value 25/85	%	± 0.5
Time response in Liquids	msec	200
Dissipation Constant in still air	mW/°C	0.3

Note. Table adapted from [34]

From the graph in Figure 22 it can be seen that the first cooled sensor is the second analog port of the input module. Because we first cooled the lowest sensor in the holder, this observation means that during the assembly of the multi-sensor, we placed the sensor which is put into the second analog port of the input module into the lowest hole of the sensor holder. The sensors that are put into the ninth and tenth analog port are also exchanged during the assembly of the multi-sensor. The remaining sensors are placed in the right order. To provide a clear notation, the order of the sensors placed in the sensor holder is used. Hence, the sensor which is placed in the lowest hole of in the multi-sensor is denoted as sensor 1.

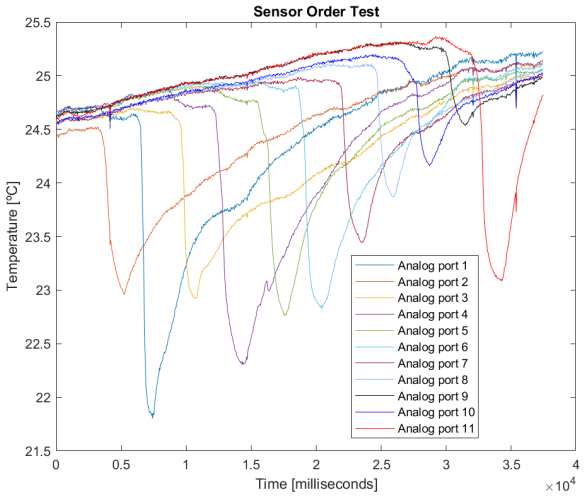

Fig. 22. Results of test which identifies the order of the sensors

We performed a test to determine the accuracy of the multi-sensor. As can be seen in Figure 23, we placed the multi-sensor and an external thermometer inside water and slowly heated this water to 40°C with a heating magnetic stirrer so the water temperature is evenly distributed. A thermocouple is also inserted into the water but is not used because this instrument does not measure temperature accurately (see Appendix D. At time periods at which the external temperature did not change, we measured the temperature of sensor 1 of the multi-sensor.

The mean temperature difference between the sensors and the external thermometer of four measurements is 0.14 ± 0.02°C, which is defined as the accuracy of the multi-sensor. The relative temperature increases within the thermometer measurements is compared with the relative temperature increases within the corresponding sensor measurement is calculated. The mean difference between these relative differences is 0.16 ± 0.14°C, which is defined as the accuracy at which sensor 1 can measure temperature increases. Detailed results of this test can be found in Appendix G.

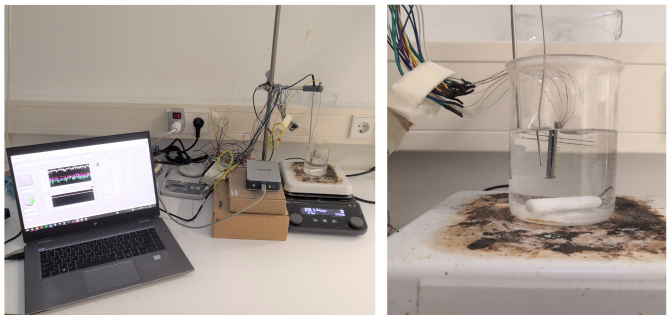

Fig. 23. Experiment setup to test the accuracy of the multi-sensor

D. Instrumentation

The lower thermography method as direct retinal temperature measurement method and the multi-sensor as contactless thermal measurement are combined in the experiment setup using the hollow box design. In this section, the required materials and the experiment setup are described, as well as the materials and the setup of the sample preparation.

1) Experiment Materials: The materials and designed components needed for the experiment setup are listed below.

- Hollow box
- Multi-Sensor
- AR-coated Germanium window
- FLIR E96 thermal camera and connection cable
- Camera tripod
- Vacuum grasper
- Laptop with Matlab and LabView
- Scissors
- Stopwatch
- Laboratory standard with clamp
- Ruler
- Two vials of 7mL Decalin
- Aluminum foil
- Cardboard paper
- Double-sided nano-grip tape
- Single-sided nano-grip tape
- Masking tape
- External hard drive

2) Experiment setup: The complete experiment setup, as depicted in Figure 24, includes all described systems. The hollow box is clamped in a laboratory standard, with the semi-transparent window containing the retina sample fixed at the bottom. The FLIR E96 thermal camera is positioned beneath the retina sample. This part of the setup provides the thermography data. The box is filled with Decalin fluid, which provides the test environment for the multi-sensor. The multi-sensor is located in into the box, which provides the sensor temperature measurements during the experiment.

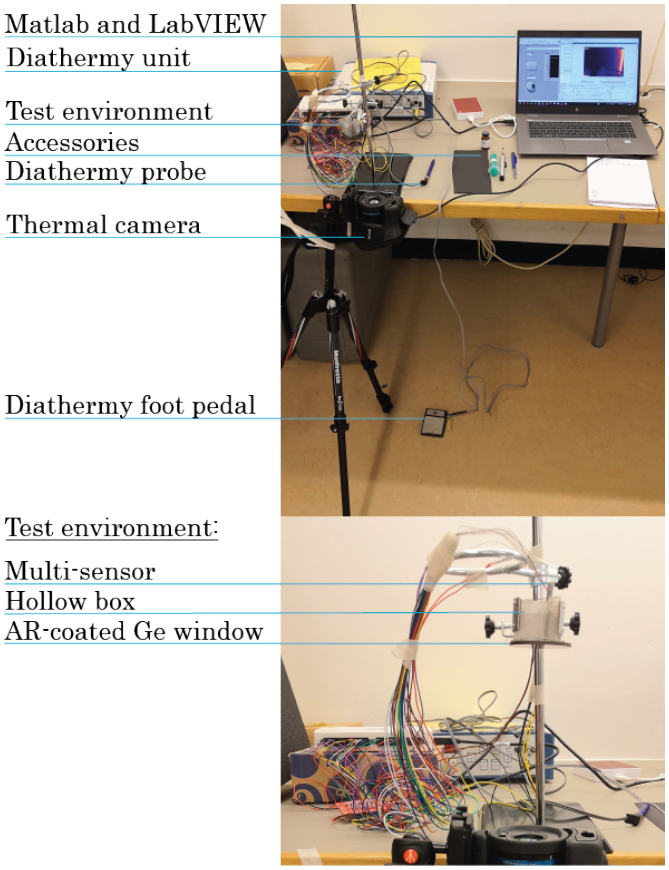

Fig. 24. Complete experiment setup

One of the additional sensors is taped to the laboratory stand to function as a reference sign sensor to align the sensor data with thermography data (Figure 25C). Another sensor is placed near the hollow box to measure the air temperature (Figure 25D). One additional sensor is taped inside the hollow box and bend horizontally at a height of 9 mm above the bottom of the box (Figure 25E), to see if there are temperature changes in the Decalin fluid which are not induced by coagulation. This height is only used as an indication of Decalin depth in case that the Decalin is lost during experiments. The remaining two sensors are taped to the laboratory stand away from the box, but on the same height as the box (Figure 25F). These external sensors can be used to identify noise induced by the environment apart from the Decalin liquid and the heated air temperature resulting from the researcher's presence.

The diathermy unit (Aesculap GN60, US), the connected diathermy probe and the diathermy foot pedal of which is located beneath the camera, provide the heat generation.

The accessories, including the syringe, the Decalin vial, a vacuum grasper, a writing pen, a note book and piece of cardboard paper, which is used to create a reference sign for alignment of the thermal camera recordings with the sensor data, near the laptop complete the experiment setup.

3) Sample Preparation Materials: The following materials needed for the preparation of retina samples.

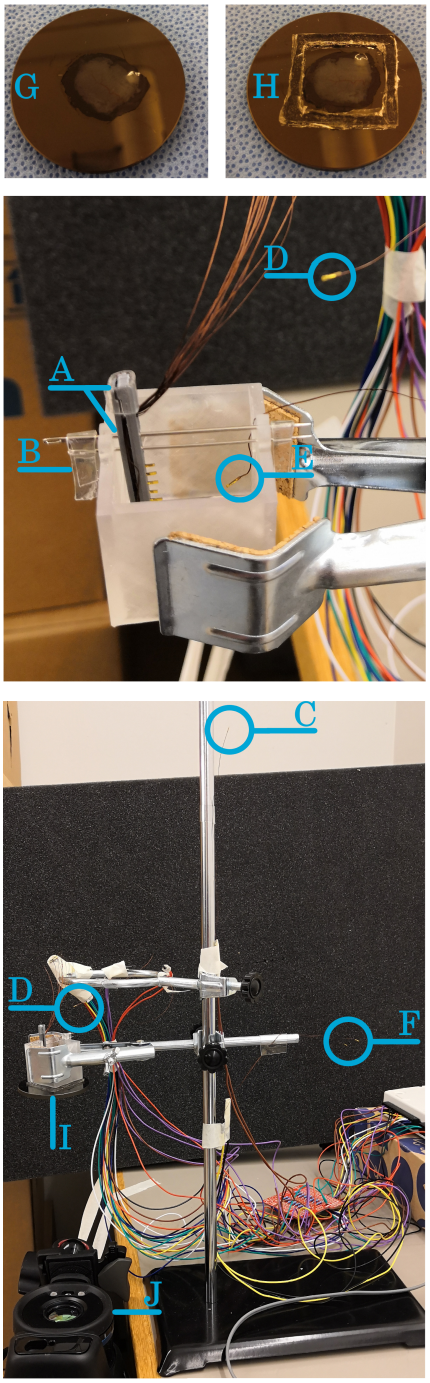

Fig. 25. Locations of experiment setup components and additional sensors

- 15 porcine cadaver eyes (provided less than 24 hours)
- Water basin
- Tissue waste can
- Preparation cloth
- Gloves
- Cleaning paper
- Incision knife
- Small scissors
- Big scissors
- Two wide tweezers

- Two thin tweezers
- AR-coated germanium window

4) Sample Preparation Setup: Figure 26 displays the sample preparation setup for eye dissection, retina removal and retina collection on the window.

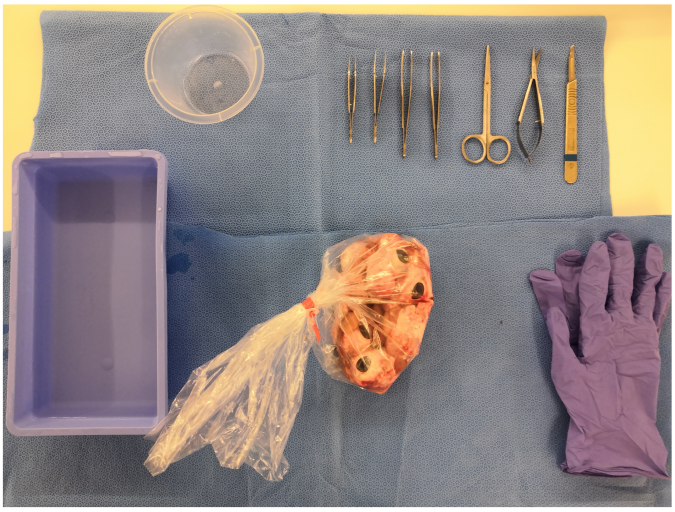

Fig. 26. Material needed for retina sample preparation

E. Experiment Settings

For the conduction of the experiments and the settings of the measurement systems, several conditions are determined.

1) Sensor Frame Rate: As the camera has an estimated frame rate of 23 frames per second, the same rate is implemented for the multi-sensor acquisition. This is set by means of loop time and amount to 43 milliseconds per sensor temperature data point.

2) Thermal Camera Settings: Several additional settings are set up in the thermal camera during the experiment. The emissivity factor 0.95 for Decalin is applied, because in the thermal image in the experiment setup, as can be seen in Figure 31A, the retina cannot be distinguished from the Decalin fluid. This value is based on the use of this factor for Decalin in the study of Riemens [35]. The humidity is set to 50% and the air temperature is set to 21%. As a result of subsubsection II-B3, the correction factor to correct for the portion of IR waves that cannot travel through the window is set to 88%.

F. Experiment Conditions

For execution of the experiment, we defined four test conditions. In this section, the reasoning for these conditions is described.

As a starting point, we defined a normal energy value, which represents normal surgical settings, and a safe maximum energy value, which represents exceptional clinical cases. The latter is chosen to measure as much heat as possible, while still providing a safe surgical coagulation outcome. The question is with what energy value the coagulation is still safe.

Electrical energy is converted to heat, which can result in the needed tissue denaturation but also unintended collateral damage. In addition to the application time, the heat (and thus tissue damage) depends on the resistance (R) and the current (I), which is equivalent to the output power (P) of the source, as depicted in Equation 3 [36, p. 446].

$$P = I^2 \times R \tag{3}$$

The use of low power (P) and applied time (t), thus the use of lower electrical energy (W) following Equation 4 [36, p. 440-441], could theoretically minimize collateral tissue damage.

$$W = P \times t \tag{4}$$

1) Safe Clinical Use: The surgical effect of coagulation of tissue is defined as ”the tissue is heated below the boiling point and undergoes thermal denaturation”

In clinical practice, safe use is not based on an energy calculation, but on the power setting of the equipment and the chosen duration of the application, leading to the desired coagulation effect. The application time is manually determined during diathermy until the desired coagulation effect on the blood vessel is visually obtained. A desired effect means that, next to the denaturation of the vessel itself, the denatured retina tissue surrounding the vessel is kept to a minimum, as can be seen in the denaturation spots in Figure 2. According to Van Overdam (personal communication, May 18, 2022), during clinical intraocular diathermy, usually 20% to 30% of the diathermy and vitrectomy system is used. In clinical use, no safe maximum power setting is defined.

2) Safe Maximum Power Estimation: The surgical diathermy and vitrectomy system can deliver a maximum power of 10 Watt (W). However, the real output power is dependent on the load impedance of the tissue, which lowers the output current according to the graph in Figure 27. The maximum output power is obtained when the circuit contains an ideal load impedance of 100 Ohm (Ω). In practice, the load is dependent on the impedance of the tissue.

Schoevaerdts et al. [37] used the electrical bio-impedance sensor to measure the proximity of a probe to the retina of a porcine eye. These measurements were made at a frequency of 349 kHz. As can be seen in Figure 28, the impedance magnitude of the porcine eye ranges from 411 Ω to 425 Ω, with a peak impedance value of 425 Ω at an electrode distance of 0mm (n=1). Generally, in electrosurgery, the frequency of the RF current can vary between 300 kHz and 5 MHz, depending on the desired surgical effect [38]. The frequency of the impedance measurement (349 kHz) is considerably close to the frequency which is used with the porcine cadaver study of Van Overdam et al. [7], where the use of a conventional disposable diathermy probe is compared with the intraocular diathermy forceps using a 450 kHz bipolar coagulator. Therefore, the tissue impedance of 425 Ω is used as an assumption value in the determination of the safe maximum output power.

If 20% to 30% power is used in normal clinical practice, 40% could be an estimation of the safe maximum power value, while using a default application time. Assuming that the

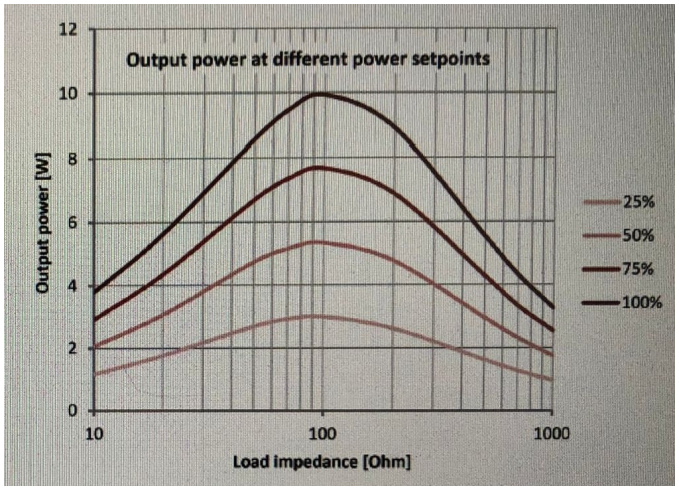

Fig. 27. Output power of the diathermy and vitrectomy system used in clinical practice, dependent on load impedance. Figure provided by Van Overdam (personal communication, May 18, 2022).

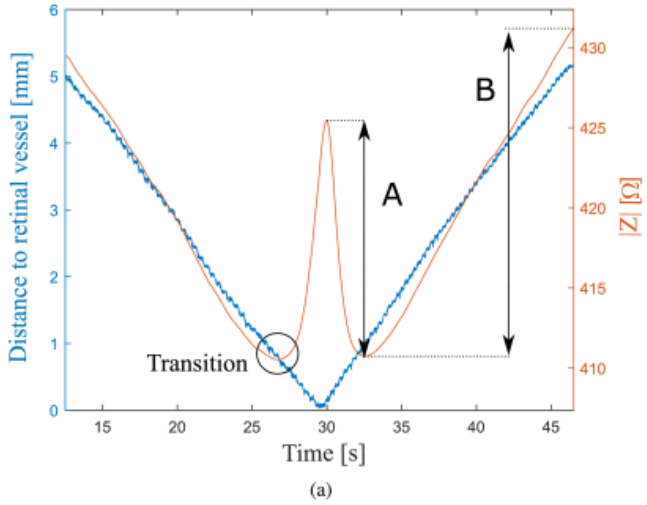

Fig. 28. Load impedance of porcine eye at varying electrode distance to retinal vessel. Figure adapted from [37]

maximum output power occurs at 40% use of the vitrectomy system and the load impedance is 425 Ω, an output power value of 2.9 W can be estimated from the graph in Figure 27.

3) Safe Maximum Energy Estimation: In order to translate the safe maximum power estimation into a safe maximum energy value, a normal application time must be determined.

In clinical practice, there is no exact value for normal application time. Therefore, for the estimation of the safe maximum energy, we assumed a normal application time of 1.5". This is based on the mean application time which is needed for coagulation with the conventional bipolar diathermy probe in the animal cadaver study of Van Overdam et al. [7], which was 1.4 ± 0.5 seconds (") (n=5) at the retinal artery and 1.6 ± 0.5" (n=5) at the retinal vein.

As energy is the product of power and time, following equation Equation 4 [36, p. 440-441], the product of the estimated safe maximum power (2.9 W) and the estimated application time (1,5") results in a safe maximum energy estimate of 4,35 J.

4) Safe Maximum Energy Validation Test: We performed a safe maximum energy validation test to determine whether the estimated safe maximum energy value of 4,35 J still has a safe coagulation effect.

During the safe maximum energy determination test, the application time is set to a constant normal value of 1.5", so only an increase in power is sufficient to determine the applied energy. The test starts with an energy of 2.25 Joule (J). This is based on the required energy in the same animal cadaver study of Van Overdam et al [7], which is 2.1 ± 0.8 J (n=5) at the retinal artery and 2.4 ± 0.8 J (n=5) at the retinal vein. A diathermy unit is used on which the output power is displayed and can be adjusted with 0.1 W. In this test, the energy is gradually increased by means of an repeated increase of 0.1 W. Using Equation 3, the initial energy of 2.25 J with a fixed duration of 1.5" results in an initial power of 1.50. This power value is increased at each measurement until an energy of 5.10 J is reached.

During coagulations with each energy condition, the denaturation spots and coagulation effect on the retina are qualitatively evaluated by visual inspection.

It resulted that from an applied energy of 2.25 to 4.05 J, normal coagulation spots were obtained. At applied energy higher than 4.5 J, severe undesirable effects emerged during coagulation, including crackling sounds, sparks, and a burnt smell. Within the energy range of 4.2 J and 4.5 J, these undesirable effects occasionally emerged and safe use must be questioned.

The main goal of this safe maximum energy validation test was to verify if a power of 2.9 W could be safely applied with an application time of 1.5", resulting in an energy of 4.35 J. This energy value lies within the questioned energy range and cannot be assumed as safe maximum energy value. The highest energy value of the safe energy appears to be 4.05 J.

5) Application Time of Conditions: Following early research which suggested that longer tissue contact results in more lateral heat [39], it is advised to use shorter application times with higher power in order to minimize collateral damage [1]. Hence, the ratio of power and time is varied in the conditions to investigate whether power or time could have a greater influence on produced heat.

It is not convenient for the experiment to use 1.5" as application time because it is difficult to apply this time correctly and to determine a second application time value which is not close to 1.5", but not to large to exceed the safe maximum energy value. Hence, the two varying application time values for the experiment are set to 1" and 2".

6) Final Safe Maximum Energy Value: As indicated from the safe maximum energy determination test, 4.05 J is the highest energy which can be safely used. With application time of 2", this energy results from a voltage of 2.025 W. The diathermy unit provides power increases of 0.1 W, so this unit cannot provide 2.025 W. Hence, we defined 4 J as the final

safe maximum energy for the experiment conditions, as power values of 2 W and 4 W can be provided by the diathermy unit.

7) Final Normal Energy Value: The defined normal energy value for the experiment conditions is based on the mean required energies in the animal cadaver study of Van Overdam et al [7], which are 2.1 ± 0.8 J (n=5) at the retinal artery and 2.4 ± 0.8 J (n=5) at the retinal vein. The mean of these two values (2.25J) could not be used because here also applies the minimal power step of 0.1 W. Hence, this value is rounded to 2.2J for the remaining two experiment conditions.

8) Final Experiment Conditions: Four voltage conditions with two varying application time values are defined, to provide two sets of two conditions which provide the same energy. These energy values are the previously defined normal and safe maximum energy values of 2.2 J and 4 J, respectively.

This results in the following conditions: 2.2 J resulting from an input of 2.2 W and 1", 4 J produced by 4 W and 1", 2.2J produced by 1.1 W and 2" and 4J resulting from 2 W and 2". In this work, these conditions are denoted following the numbers displayed in Table III.

TABLE III
NOTATION NUMBER OF EXPERIMENT CONDITIONS

Notation #	Condition
C1	2.2J (2.2W * 1")
C2	4J (4W * 1")
C3	2.2J (1.1W * 2")
C4	4J (2W * 2")

The experiment protocol contains two repetitions of 10 measurements with each condition. In each measurement, the temperature resulting from one coagulation is measured. In the full notation of each measurement (eg. C1_R1_M1), the condition numbers are denoted as C1, the repetition numbers are denoted by R1, the measurement number is denoted as M1. It is intended to use the following order of repetitions: C1_R1, C2_R1, C3_R1, C4_R1, C1_R2, C2_R2, C3_R2, C4_R2.

Before these repetitions can be performed, the experiment setup has to be assembled. This consists of a first assembly to create the hollow box environment merely containing the multi-sensor and to test this setup including the thermal camera. Second, the retina sample is prepared. This cannot take place before the first setup assembly, as the retina sample will dry out over time. Third, the sample is added to the test environment, and the setup is completed with Decalin. For these assembly steps, the following protocols must be followed.

9) Protocol for Fixation of Hollow Box and Multi-sensor: The first assembly, the fixation of the hollow box and the multi-sensor, the hollow box is clamped in a laboratory stand using the following steps.

1) Fix the multi-senor in the hollow box by inserting the two guide rods through the guiding holes and inlets of the hollow box (Figure 25A)
2) Tape the guide rods to each other (Figure 25B) to prevent vertical movement of the multi-sensor
3) Tape the five additional NTC sensors at the locations described in subsubsection II-D2
4) Connect the multi-sensor to the laptop
5) Place the thermal camera under the hollow box and connect is to the laptop
6) Test the reflective temperature using step 2 of the transmission factor determination test, which is described in Appendix C and set this setting in the camera
7) Setup the camera settings (described in subsection II-E)
8) Test this first setup assembly
9) Adjust the sensor frame rate to 43 milliseconds and add the correct file save path in the LabView program
10) Set the returned color space setting to red-green-blue (RGB) and the logging options to memory and Audio Video Interleave (AVI) file to disk saving, including automatically increment filename, in the Matlab Image Acquisition Toolbox interface
11) Perform a test run with the sensor and the thermal camera at the same time, to see if both files can be saved and retrieved.
12) Remove the camera away from the hollow box
13) Connect the diathermy probe is to the diathermy unit and place the foot pedal of the diathermy unit on the ground beneath the camera
14) Test the diathermy probe by hearing a sound made by the diathermy when pressing the foot pedal

10) Protocol for Sample Preparation: After testing the setup, the retina sample must be prepared by the following protocol. To create this protocol, we performed several preliminary studies on how the retina sample can be separated and collected (see Appendix H).

1) Fill the basin with water
2) Cut the fat tissue off the eye ball (Figure 29A)
3) Make an incision with the knife along the edge of the cornea and cut the cornea along the edge with a pair of scissors. Remove the cornea and the lens with a pair of tweezers (Figure 29B)
4) Let the vitreous humour fall out of the eye by turning the eye upside down with a pair of tweezers (Figure 29C)
5) Cut through the sclera with a pair of scissors at the location at which the optic nerve is the closest to the created opening, until the optic nerve is nearly reached (Figure 29D)
6) Hold the the eye in the water with a pair of tweezers so the retina comes loose (except its fixation at the optic nerve) and slides down (Figure 29E)
7) Check if the retina is slid down and is only fixed at the optic nerve (Figure 29F)
8) Scrape down along the optic nerve to remove the retina from the optic nerve (Figure 29G)
9) Check if the retina is completely loose from the optic nerve (Figure 29H)
10) Hold the the eye in the water with a pair of tweezers (Figure 29I) and move the eye so the retina comes loose completely and lays in the water (Figure 29J)
11) Collect the retina from the water on the window, by moving the window beneath the retina and moving upwards while the water is flowing down while the retina stays at its place by holding it gently with one side of

a pair of thin tweezers (Figure 29K)

12) Create a piece of retina which fits inside the hollow box profile (23*23 mm), remove excess of retina using a knife and a pair of thin tweezers and dry the window around the sample with cleaning paper (Figure 29L)

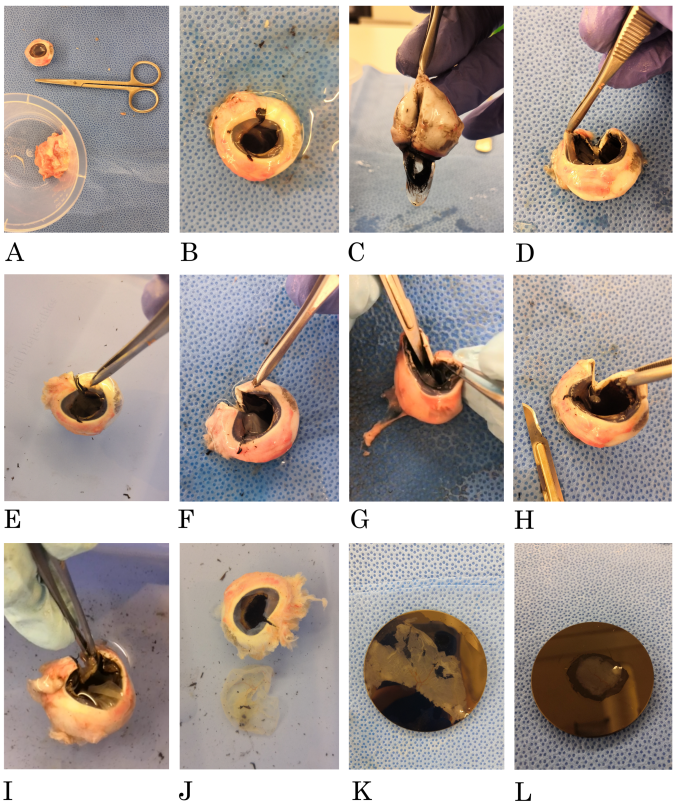

Fig. 29. Images of retina sample preparation steps

11) Protocol for Experiment Setup Completion: The following steps are performed to complete the setup of the experiment.

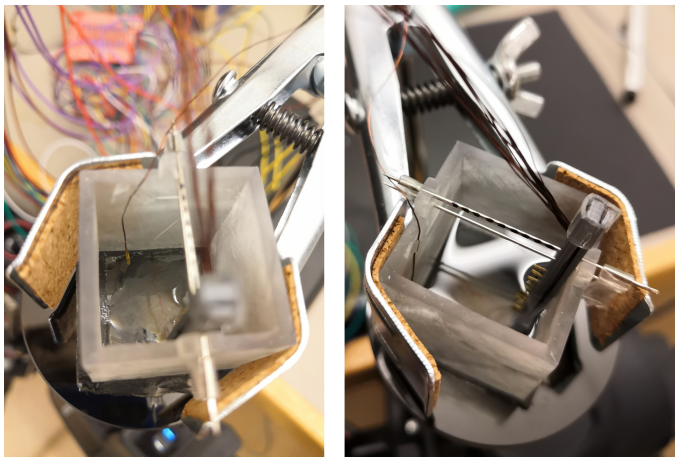

Fig. 30. Experiment box containing the retina sample (left) and filled with Decalin fluid (right)

1) Cut a piece of double sided tape in the same profile of the hollow box and place it on the window around the sample (Figure 25H). To enhance the ease of finding a location for coagulation on the retinal blood vessel during the experiments, the edges of tape should be placed parallel to a blood vessel in the retina sample
2) Adhere the window containing the retina sample and the double-sided tape to the hollow box which is already fixated in the laboratory stand clamp (Figure 25I). This results in a closed box containing the retina sample, as shown in the left image of Figure 30.
3) Fill the box with 10.6 mL Decalin as shown in the right image of Figure 30.
4) Place the thermal camera 16cm beneath the box, pointed at the window (Figure 25J) and connect it to the laptop.
5) Place a syringe, the empty Decalin vial, a vacuum grasper, a writing pen, a note book and piece of cardboard paper, near the experiment laptop.

12) Protocol for Experiment Measurements: The retina samples are coagulated 10 times using the following experiment protocol. This protocol is repeated at each repetition.

1) Set correct power condition in the diathermy unit
2) Note the name of test round and fill it in as saving name in LabView
3) Start sensor acquisition (note starting time)
4) Start image acquisition (note starting time)
5) Move the black cardboard paper between the camera and the sample and hold the reference sensor at the same time
6) Remove the black cardboard paper and release the reference sensor at the same time
7) Repeat steps 5-6
8) Note the time of probe insertion
9) Insert the diathermy probe inside the box through the ring of the sensor holder until it softly reaches the retina on a retinal vessel
10) Push coagulation foot pedal for 1 or 2”s, depending on the condition
11) Wait for 30” while not moving the probe
12) Remove probe
13) Note the time of probe removal
14) Move sensor 1 step along guide rods (0.2 mm)
15) Wait 30”s
16) Repeat steps 1 to 15 for a maximum of 3 or 4 times
17) Move the black cardboard paper between the camera and the sample and hold the reference sensor at the same time
18) Remove the black cardboard paper and release the reference sensor at the same time
19) Repeat steps 17-18
20) Stop thermography and sensor acquisition
21) Export the acquired Matlab file
22) Repeat steps 1-19 until a total of 10 coagulation measurements are obtained

Once one repetition is performed, a new sample must be implemented into the test environment. Therefore, in between each repetition, the Decalin is drained and stored in the

Decalin vial and the window, and the sample and the excess of tape are removed from the hollow box. Subsequently, the protocols for sample preparation and for experiment setup completion are repeated.

G. Data Processing Methods

The results of the final experiment can be obtained by running one Matlab script, while following instructions from a diagram (see Appendix I).

1) Conversion of Thermography Images to Temperature: The Matlab Image Acquisition Toolbox is used to record the thermal images and export these as a Matlab file for processing and an AVI file as backup. A description of the file formats is given in Appendix J. The Matlab files provide a sequence of thermal image frame, which consists of pixels corresponding to a RGB color value. In each thermal image frame, a color bar is present. Figure 31A shows an example of a thermal image frame.

To retrieve the temperature value of each pixel, first, the RGB image frame is converted to a grayscale image with intensity values from 0 to 255. Second, the grayscale image is converted to an indexed image. In this indexed image, the intensities of the grayscale pixels are converted to values within the range of 0 to 380, based on the color map containing 380 colors, within the range of 0 to 1. This means that a pixel value of 1 corresponds to the color value of the first row of the color map [40]. Third, the indexed image is converted to a grayscale image containing pixel values within the range of 0 to 1 (black and white, respectively). Subsequently, the pixel values can be used as factor which is applied to the temperature difference between the minimum and maximum temperature on the original thermal image frame, and added to the minimum temperature. The minimum and maximum temperature values are automatically identified using optical character recognition. This calculation results in the temperature and is applied to all pixel to create a temperature image.

Because the the colors in the original color map on the grayscale image are not equally distributed, the color distribution differs from the used color map containing 380 colors. Hence, temperature effect of this dissimilarity is determined by taking the intensity difference between these two color maps and multiply the intensity difference with the maximum temperature difference in the image. This resulted in a mean temperature difference of 0.05 ± 0.04°C. Because the minimum temperature increase in the experiment is 0,73°C, we consider this difference as an acceptable deviation. A detailed description of this calculation can be found in Appendix K.

2) Thermography Temperature Peak Calculation: The conversion to temperature image is only applied to the thermal image frames on which heating is visible. Therefore, the frame number of the first and last frames that contain a visible heating point of each measurement is manually identified. At each first heating frame of each measurement, the region of interest (ROI) is manually determined. When these manual steps are performed of all the measurements, the remaining thermography processing steps of each measurement are performed automatically.

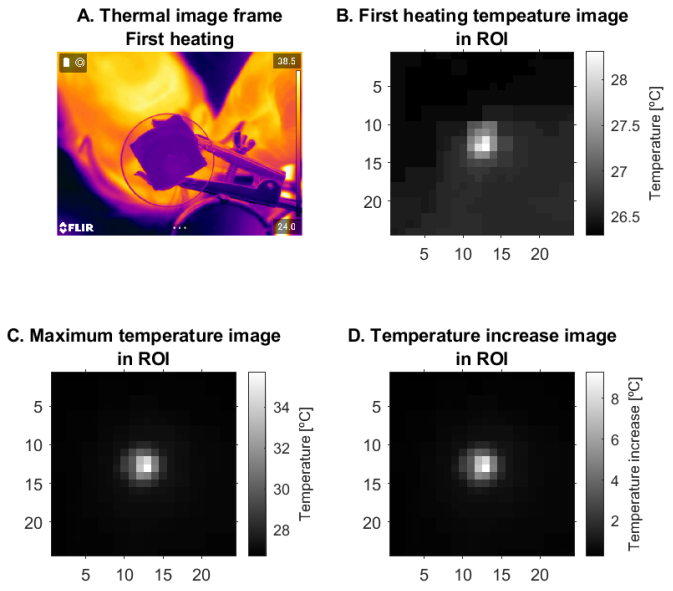

Fig. 31. Thermal image frame (A), first heating temperature image (B), maximum temperature image (C), and temperature increase image (D) of Measurement C2_R2_M4

The following images and temperature values are obtained of each measurement. The first thermal image frame in which a heating point is visible is shown in Figure 31A. All frames within the heating range are converted to temperature images and are framed within the predetermined ROI. The first temperature image of the heating (first heating temperature image) is shown in Figure 31B. The maximum temperature value of all temperature images is identified and the temperature image that contains this maximum value within the ROI (maximum temperature image) is identified (Figure 31C). The reference temperature is calculated by taking the grand mean of all mean temperatures within the ROI of 20 temperature images before the first frame at which a heating point is visible. The temperature image containing the temperature increase values within the ROI (temperature increase image in Figure 31D)) is obtained by subtracting the reference temperature, which is the grand mean of all mean temperatures within the ROI of 20 temperature images before the first heating temperature image, from each pixel of the maximum temperature image within the ROI.

3) Sensor Data Processing: Labview is used to acquire the sensor data and export these as a text file for processing in Matlab. Before the temperature increase values of the sensor measurement can be retrieved, a for loop consisting of filtering steps and trampling is executed.

4) Sensor Data Filtering: As can be seen in Figure 32, the noise peaks of the raw sensor data (blue) are removed resulting in the filtered data (orange). The filtering steps include median linear outlier filling, one-dimensional third-order median filtering and low-pass filtering. The detailed description of filters can be found in Appendix L

As can be seen at the external sensor in Figure 33, the same

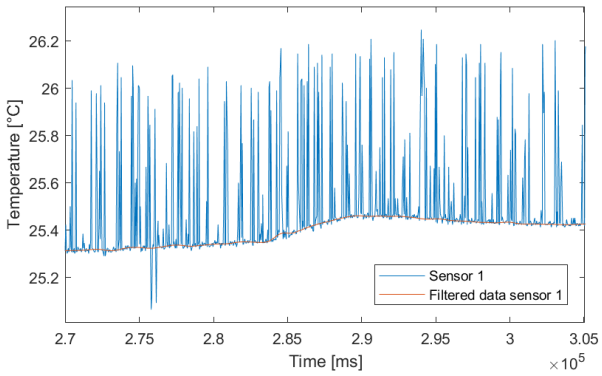

Fig. 32. Example of raw data (blue) and filtered data (orange) of sensor 1 from Measurement C2_R2_M4

type of peaks are emerging at the same time as in sensor 1, which proves that the peaks are noise.

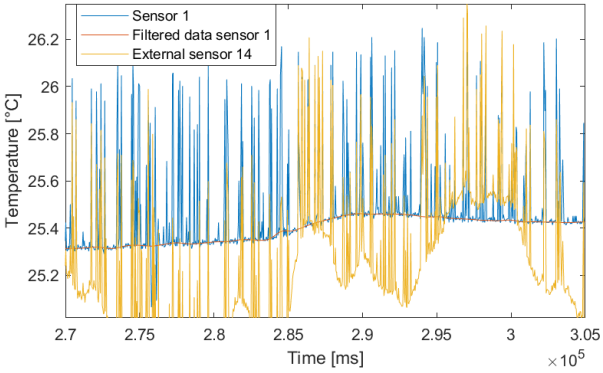

Fig. 33. Raw data of external sensor 14 (yellow) plotted over raw data (blue) and filtered data (orange) of sensor 1 from Measurement C2_R2_M4

5) Thermography and Sensor Data Alignment: The frame rate for thermography and sensor acquisition varies within these methods, as well as between these methods. Furthermore, the starting and ending time of the saved thermography and sensor data of each acquisition is not equal. Hence, to indicate if temperature peaks in the sensor data are during the coagulation or after the coagulation, we downsampled the sensor data.

For downsampling, at the beginning and the end of each acquisition, two reference signs are induced at both measurements systems at the same time. The reference sign at the sensor is induced by holding an additional sensor, so its becomes heated. The reference sign for the thermal camera is induced by holding a piece of cardboard paper in between the camera and the sample. At the same time, the sensor is released and the paper is removed.

The last frame fully displaying the cardboard paper and the index of the highest reference sensor temperature peaks are identified as reference signs.

To downsample the sensor data set, the sensor data points in between the sensor reference sings are distributed over the frames in between the thermography reference signs. This is done by creating an array with the sensor reference sign index added with the subsequent data point multiplied by the step size. This step size is determined by dividing the amount of sensor data points in between the sensor reference signs by the amount of sensor data points in between the thermography reference signs. Sensor data points outside the reference sign region are not included in this array. The rounded values of this array are used as ranges to create a new down-sampled sensor data set of each measurement.

6) Sensor Temperature Peak Calculation: Of each filtered and downsampled measurement, a graph is plotted in the time range of 5 seconds before and 27 seconds after the real-time moment at which the corresponding thermography measurement shows the maximum temperature increase.

Figure 34 displays an example of the temperature peak of sensor 1 in Measurement C2_R2_M4. The real-time moment at which the corresponding thermography measurement shows the maximum temperature increase is denoted with an asterisk. The real time heating duration measured at the corresponding thermography measurement is indicated in orange.

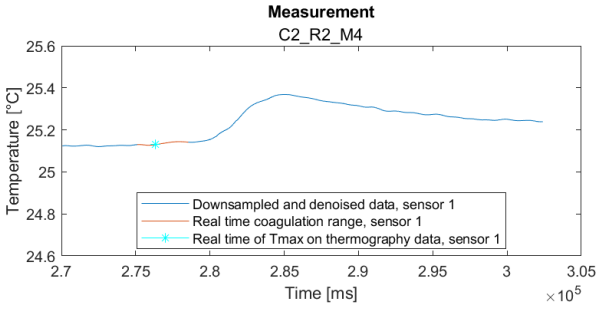

Fig. 34. Example of the temperature peak after heating in Measurement C2_R2_M4

The temperature increase values are measured by subtracting the reference temperature before the visible peak from the maximum temperature of the visible peak. The reference temperature value is the mean temperature of 20 sensor data points before the sensor data point at which visible heating begins at the thermography measurement. The maximum temperature is then identified.

7) Sensor Temperature Measurement Inclusion: First, the inclusion of sensor measurements is based on a minimal gradient value of 0.0010 between data points within the measurement. After this computational selection (see Matlab script in Appendix M, the data plots of selected peaks are visually checked to see whether the minimum gradient of 0.0010 is due to a visible peak, due to a coincidental peak or due to noise in the sensor data. Measurements at which no visible peak can be identified are considered invalid measurements and are therefore excluded from the sensor analysis.

8) Data Analysis Methods: After processing the data of the thermography and sensor measurements are processed and obtaining the temperature increase values, we calculated mean, standard deviation, effect size (Cohen's d) and error values of the measurements.

Based on the recommendations for the interpretation of the Cohen's d effect size provided by Cohen [41], we defined a small effect size as $0.2 \geq d < 0.5$, a medium effect size as $0.5 \geq d < 0.8$ and a large effect size as $d \geq 0.8$.

III. Results

The results section is divided into several subsections. External factors that have affected the experimental plan are described. The heating duration is reported. The measurement inclusion rate of the lower thermography method is reported, after which the thermography findings are described. Thereafter, the sensor measurement inclusion rate and the sensor findings are described. Finally, a comparison of effect sizes and a comparative error bar graph of the thermography and the sensor data are provided.

Matlab scripts which are used to obtain the results can be downloaded via this link. Acquired raw data is in possession of the researchers and the TU Delft.

A. External Factors

Due to the lack of time, we performed fewer measurements than intended and changed the order of acquisition. Specifically, more time was spent on eye separation, as retina samples could not be prepared beforehand. This is because if pieces of separated retina were to preserved in the water bath, the blood would flow out of the vessels and when pieces of retina are preserved in the open air, the tissue dries out. Moreover, the acquisition times and data saving times were longer than expected. Additionally, because the Decalin fluid was lost several times during the experiment, the test environment had to be removed from the camera and replaced with a new retina sample. Hence, of the 80 intended measurements, only 72 measurements were performed.

The number of measurements in the second repetition round (C1_R2, C2_R2, C3_R2 and C4_R2) was decreased to 8 measurements per condition. Moreover, the execution order of the second repetition was changed to the following: C1_R2, C2_R2, the first four measurements of C3_R2, C4_R2, and the remaining four measurements of C3_R2.

During the experiment, the thickness of the double-sided tape in between the hollow box and the window adds up 2 mm to the height of the multi-sensor above the upper window surface, which was not accounted for in the design of the measuring system. The sensor height above the upper window surface is defined as the sensor height above the coagulation site, because the direct temperature of the lower surface of the retina, which faces the upper window surface, is measured.

B. Thermography Analysis

In this subsection, the results within the thermography measurements are described.

1) Thermography Measurement Inclusion Rate: With the thermal camera, the 72 measurements were recorded. 71 recordings could be exported as Matlab file and could be processed directly in Matlab following the methods described in subsection II-G. The relevant thermal images of the remaining record were manually identified and individually exported from an AVI file (see acquisition formats in Appendix J). Hence, all 72 coagulation recordings could be processed for

TABLE IV
Thermography findings

Measurement #	Condition (E (P*t))	Max. T [°C]	Ref. T [°C]	T Incr. [°C]
C1_R1_M1	2.2J (2.2W * 1")	28.31	27.58	0.73
C1_R1_M2	2.2J (2.2W * 1")	28.45	27.44	1.01
C1_R1_M3	2.2J (2.2W * 1")	29.10	27.86	1.23
C1_R1_M4	2.2J (2.2W * 1")	28.74	27.52	1.22
C1_R1_M5	2.2J (2.2W * 1")	28.75	27.82	0.92
C1_R1_M6	2.2J (2.2W * 1")	29.10	27.80	1.30
C1_R1_M7	2.2J (2.2W * 1")	30.02	27.59	2.43
C1_R1_M8	2.2J (2.2W * 1")	29.57	27.76	1.81
C1_R1_M9	2.2J (2.2W * 1")	29.95	27.74	2.21
C1_R1_M10	2.2J (2.2W * 1")	30.10	27.76	2.34
C2_R1_M1	4J (4W * 1")	32.65	25.81	6.84
C2_R1_M2	4J (4W * 1")	36.26	25.76	10.50
C2_R1_M3	4J (4W * 1")	34.12	25.60	8.52
C2_R1_M4	4J (4W * 1")	33.35	25.97	7.38
C2_R1_M5	4J (4W * 1")	34.29	25.83	8.47
C2_R1_M6	4J (4W * 1")	36.37	26.34	10.03
C2_R1_M7	4J (4W * 1")	39.41	26.82	12.59
C2_R1_M8	4J (4W * 1")	35.97	26.62	9.34
C2_R1_M9	4J (4W * 1")	37.59	26.63	10.96
C2_R1_M10	4J (4W * 1")	36.25	27.22	9.03
C2_R2_M1	4J (4W * 1")	31.08	26.35	4.73
C2_R2_M2	4J (4W * 1")	35.16	26.81	8.34
C2_R2_M3	4J (4W * 1")	33.99	26.42	7.57
C2_R2_M4	4J (4W * 1")	35.73	26.43	9.30
C2_R2_M5	4J (4W * 1")	34.17	26.67	7.49
C2_R2_M6	4J (4W * 1")	34.67	27.17	7.50
C2_R2_M7	4J (4W * 1")	35.38	26.92	8.46
C2_R2_M8	4J (4W * 1")	36.37	27.30	9.07
C3_R1_M1	2.2J (1.1W * 2")	29.18	27.19	2.00
C3_R1_M2	2.2J (1.1W * 2")	29.34	27.25	2.08
C3_R1_M3	2.2J (1.1W * 2")	29.43	27.35	2.08
C3_R1_M4	2.2J (1.1W * 2")	28.08	26.69	1.39
C3_R1_M5	2.2J (1.1W * 2")	29.16	27.35	1.81
C3_R1_M6	2.2J (1.1W * 2")	29.32	27.44	1.88
C3_R1_M7	2.2J (1.1W * 2")	29.56	27.58	1.97
C3_R1_M8	2.2J (1.1W * 2")	28.74	27.03	1.71
C3_R1_M9	2.2J (1.1W * 2")	29.17	27.34	1.83
C3_R1_M10	2.2J (1.1W * 2")	30.55	27.62	2.93
C3_R2_M1	2.2J (1.1W * 2")	30.57	28.42	2.15
C3_R2_M2	2.2J (1.1W * 2")	30.76	28.34	2.41
C3_R2_M3	2.2J (1.1W * 2")	31.28	28.34	2.94
C3_R2_M4	2.2J (1.1W * 2")	31.89	28.11	3.78
C3_R2_M5	2.2J (1.1W * 2")	27.43	26.58	0.85
C3_R2_M6	2.2J (1.1W * 2")	28.65	26.91	1.74
C3_R2_M7	2.2J (1.1W * 2")	28.26	26.87	1.39
C3_R2_M8	2.2J (1.1W * 2")	28.14	26.85	1.28
C4_R1_M1	4J (2W * 2")	32.60	27.27	5.33
C4_R1_M2	4J (2W * 2")	33.59	27.43	6.16
C4_R1_M3	4J (2W * 2")	33.83	27.52	6.31
C4_R1_M4	4J (2W * 2")	33.83	28.08	5.75
C4_R1_M5	4J (2W * 2")	32.70	27.65	5.06
C4_R1_M6	4J (2W * 2")	35.95	27.53	8.42
C4_R1_M7	4J (2W * 2")	33.88	27.82	6.07
C4_R1_M8	4J (2W * 2")	33.20	27.52	5.69
C4_R1_M9	4J (2W * 2")	34.28	27.74	6.54
C4_R1_M10	4J (2W * 2")	37.39	27.78	9.60
C4_R2_M1	4J (2W * 2")	30.14	27.01	3.13
C4_R2_M2	4J (2W * 2")	31.28	26.85	4.43
C4_R2_M3	4J (2W * 2")	32.65	26.61	6.04
C4_R2_M4	4J (2W * 2")	37.14	26.91	10.23
C4_R2_M6	4J (2W * 2")	32.53	27.62	4.92
C4_R2_M7	4J (2W * 2")	30.79	26.84	3.95
C4_R2_M8	4J (2W * 2")	32.58	26.49	6.08

the visual detection of temperature increase.

All eight measurements in Repetition C1_R2, are excluded from the thermography and the sensor analysis because the indented condition (2.2J (2.2W * 1")) seems to not have been achieved judging from the found effect size of -3.28 between the mean heating duration of Repetitions C1_R1 and C1_R2, which is out of proportion compared to the effect sizes of the other repetitions with the same condition, which are d=-0.06, d=-0.34 and d=-0.82, respectively (for more details, see Appendix N). Measurement C4_R2_M5 is excluded from the thermography analysis because no temperature increase could be visually detected.

After measurement exclusion, the resulting thermography sample sizes of Conditions 1, 2, 3 and 4 are 10, 18, 18 and 17 measurements, respectively. The temperature increase data of the excluded thermography measurements can be found in Appendix O.

2) Heating Duration: By qualitative visual identification of thermal images, the total heating duration and the duration from the first frame on which heating is visible, until the frame containing the maximum temperature value, are determined. The means and standard deviations of the heating duration are displayed in Table VI. Condition 1 has the shortest mean heating duration of 37 ± 6 frames. Condition 4 has the longest heating duration of 83 ± 14 frames. The mean duration from the first frame on which heating is visible, until the frame containing the maximum temperature value, is the shortest at Condition 2 (19 ± 6 frames) and the longest at Condition 4 (41 ± 9 frames), respectively.

TABLE V
MEAN AND STANDARD DEVIATION OF COAGULATION HEATING DURATION AND DURATION UNTIL MAXIMUM TEMPERATURE FRAME PER CONDITION (IN AMOUNT OF FRAMES)

Condition	$\bar{x}$ **± SD Heating Duration**	$\bar{x}$ **± SD Duration Until Max. T**
C1: 2.2J (2.2W * 1")	37 ± 6	21 ± 5
C2: 4J (4W * 1")	62 ± 9	19 ± 6
C3: 2.2J (1.1W * 2")	56 ± 6	37 ± 8
C4: 4J (2W * 2")	83 ± 14	41 ± 9

Table VI shows the Cohen's d effect sizes between the condition means of heating duration until maximum temperature. The effect sizes between Conditions 1 and 2 and between Conditions 3 and 4 are small. The effect sizes between the remaining conditions are large.

TABLE VI
HEATING DURATION EFFECT SIZE BETWEEN CONDITIONS

Condition	$\bar{x}$ **± SD [°C]**	**Condition**	$\bar{x}$ **± SD [°C]**	**Cohen's d**
C1	21 ± 5	C2	19 ± 6	0.23
C1	21 ± 5	C3	37 ± 8	-2.26
C1	21 ± 5	C4	41 ± 9	-2.50
C2	19 ± 6	C3	37 ± 8	-2.47
C2	19 ± 6	C4	41 ± 9	-2.75
C3	37 ± 8	C4	41 ± 9	-0.41

3) Thermography Temperature: Table IV shows the temperature increase values (T Incr.) which are obtained from the thermal image frames. The converted temperature images of each measurement can be found in Appendix P. The lowest temperature increase is found in Measurement C1_R1_M1 (0.73°C) and the highest temperature increase is found in Measurement C2_R1_M7 (12.59°C).

4) Thermography Condition Temperature: The mean temperature increases of each condition are shown in Table VII. The condition with the highest mean temperature increase of the thermography measurements is Condition 2 (8.67°C). The lowest mean temperature increase is found in Condition 1 (1.52°C).

TABLE VII
MEAN AND STANDARD DEVIATION OF MAXIMUM TEMPERATURE AND REFERENCE TEMPERATURE, AND MEAN TEMPERATURE INCREASE PER THERMOGRAPHY CONDITION

Condition	$\bar{x}$ **± SD Ref. T [°C]**	$\bar{x}$ **± SD Max. T [°C]**	$\bar{x}$ **T Incr. [°C]**
C1: 2.2J (2.2W * 1")	27.69 ± 0.14	29.21 ± 0.66	1.52
C2: 4J (4W * 1")	26.48 ± 0.52	35.16 ± 1.89	8.67
C3: 2.2J (1.1W * 2")	27.40 ± 0.57	29.42 ± 1.19	2.01
C4: 4J (2W * 2")	27.33 ± 0.46	33.43 ± 1.98	6.10

5) Thermography Effect Size Between Conditions: The effect sizes between mean temperature increase values of the thermography conditions are shown in Table VIII. A large effect size is found between the thermography temperature increase means of all of the conditions, except between Conditions 1 and 3, which is a medium effect size of d=-0.72. The highest effect size values are found between Conditions 1 and 2, and between Conditions 2 and 3 (d=-4.77 and d=4.92, respectively).

TABLE VIII
EFFECT SIZE BETWEEN THERMOGRAPHY CONDITIONS

Condition	$\bar{x}$ **± SD [°C]**	**Condition**	$\bar{x}$ **± SD [°C]**	**Cohen's d**
C1	1.52 ± 0.63	C2	8.67 ± 1.74	-4.77
C1	1.52 ± 0.63	C3	2.01 ± 0.68	-0.72
C1	1.52 ± 0.63	C4	6.10 ± 1.85	-2.91
C2	8.67 ± 1.74	C3	2.01 ± 0.68	4.92
C2	8.67 ± 1.74	C4	6.10 ± 1.85	1.40
C3	2.01 ± 0.68	C4	6.10 ± 1.85	-2.90

C. Sensor Analysis

In this subsection, the results of the sensor measurements are described.

1) Sensor Measurement Inclusion Rate: Of the remaining 64 measurements, 45 measurements are selected at which a real temperature peak can be identified in the data of sensor 1 at a height of 5.5 mm above the coagulation site. Gradient values of the selected measurements and excluded peaks by visual check can be found in Appendix M. This leads to a sensor sample size per condition of 2, 18, 7 and 18 peak measurements in Condition 1, 2, 3 and 4, respectively.

2) Sensor Temperature: Table IX shows the temperature increase values (T Incr.), which are obtained from the data graphs of sensor 1 (see Appendix Q. The temperature increase values of all measurements range from 0.06°C at Measurement C3_R2_M4 to 0.57°C at Measurement C4_R2_M5.

TABLE IX
SENSOR FINDINGS

Measurement #	Condition (E (P*t))	Max. T [°C]	Ref. T [°C]	T Incr. [°C]
C1_R1_M1	2.2J (2.2W * 1")	25.31	25.24	0.08
C1_R1_M3	2.2J (2.2W * 1")	25.67	25.58	0.08
C2_R1_M1	4J (4W * 1")	24.96	24.75	0.21
C2_R1_M2	4J (4W * 1")	25.11	24.88	0.22
C2_R1_M3	4J (4W * 1")	25.10	24.97	0.13
C2_R1_M4	4J (4W * 1")	25.21	25.04	0.17
C2_R1_M5	4J (4W * 1")	25.31	25.10	0.21
C2_R1_M6	4J (4W * 1")	25.29	25.16	0.12
C2_R1_M7	4J (4W * 1")	25.45	25.21	0.24
C2_R1_M8	4J (4W * 1")	25.43	25.23	0.20
C2_R1_M9	4J (4W * 1")	25.38	25.23	0.15
C2_R1_M10	4J (4W * 1")	25.47	25.28	0.19
C2_R2_M1	4J (4W * 1")	25.13	25.00	0.13
C2_R2_M2	4J (4W * 1")	25.23	25.01	0.22
C2_R2_M3	4J (4W * 1")	25.27	25.09	0.18
C2_R2_M4	4J (4W * 1")	25.37	25.13	0.24
C2_R2_M5	4J (4W * 1")	25.29	25.14	0.16
C2_R2_M6	4J (4W * 1")	25.43	25.15	0.28
C2_R2_M7	4J (4W * 1")	25.35	25.17	0.18
C2_R2_M8	4J (4W * 1")	25.41	25.23	0.18
C3_R1_M2	2.2J (1.1W * 2")	26.19	26.08	0.11
C3_R1_M7	2.2J (1.1W * 2")	25.97	25.79	0.17
C3_R1_M10	2.2J (1.1W * 2")	25.70	25.54	0.16
C3_R2_M1	2.2J (1.1W * 2")	26.14	26.07	0.08
C3_R2_M2	2.2J (1.1W * 2")	26.14	26.05	0.09
C3_R2_M3	2.2J (1.1W * 2")	26.10	25.99	0.10
C3_R2_M4	2.2J (1.1W * 2")	26.03	25.97	0.06
C4_R1_M1	4J (2W * 2")	26.42	26.22	0.19
C4_R1_M2	4J (2W * 2")	26.28	26.08	0.21
C4_R1_M3	4J (2W * 2")	26.18	25.96	0.22
C4_R1_M4	4J (2W * 2")	26.20	25.90	0.30
C4_R1_M5	4J (2W * 2")	25.82	25.72	0.09
C4_R1_M6	4J (2W * 2")	25.91	25.67	0.24
C4_R1_M7	4J (2W * 2")	26.02	25.63	0.39
C4_R1_M8	4J (2W * 2")	25.64	25.51	0.13
C4_R1_M9	4J (2W * 2")	25.74	25.45	0.29
C4_R1_M10	4J (2W * 2")	25.78	25.48	0.30
C4_R2_M1	4J (2W * 2")	25.98	25.83	0.15
C4_R2_M2	4J (2W * 2")	26.08	25.78	0.30
C4_R2_M3	4J (2W * 2")	26.02	25.76	0.27
C4_R2_M4	4J (2W * 2")	26.09	25.68	0.41
C4_R2_M5	4J (2W * 2")	26.61	26.04	0.57
C4_R2_M6	4J (2W * 2")	26.21	26.04	0.17
C4_R2_M7	4J (2W * 2")	26.20	25.98	0.22
C4_R2_M8	4J (2W * 2")	26.10	25.96	0.14

3) Sensor Condition Temperature: The mean temperature increases of each condition are shown in Table VII. The condition with the highest mean temperature increase of the sensor measurements is Condition 4 (0.25°C) and the lowest mean temperature increase is found in Condition 1 (0.08°C).

TABLE X
MEAN AND STANDARD DEVIATION OF MAXIMUM TEMPERATURE AND REFERENCE TEMPERATURE, AND MEAN TEMPERATURE INCREASE PER THERMOGRAPHY CONDITION

Condition	$\bar{x}$ ± SD Ref. T) [°C]	$\bar{x}$ ± SD Max. T [°C]	$\bar{x}$ T Incr. [°C]
C1: 2.2J (2.2W * 1")	25.41 ± 0.24	25.49 ± 0.25	0.08
C2: 4J (4W * 1")	25.10 ± 0.14	25.29 ± 0.14	0.19
C3: 2.2J (1.1W * 2")	25.93 ± 0.20	26.04 ± 0.17	0.11
C4: 4J (2W * 2")	25.82 ± 0.22	26.07 ± 0.24	0.25

TABLE XI
EFFECT SIZE BETWEEN SENSOR CONDITIONS

Condition	$\bar{x}$ ± SD [°C]	Condition	$\bar{x}$ ± SD [°C]	Cohen's d
C1	0.08 ± 0.00	C2	0.19 ± 0.0	-2.54
C1	0.08 ± 0.00	C3	0.11 ± 0.04	-0.69
C1	0.08 ± 0.00	C4	0.25 ± 0.12	-1.48
C2	0.19 ± 0.04	C3	0.11 ± 0.04	1.80
C2	0.19 ± 0.04	C4	0.25 ± 0.12	-0.73
C3	0.11 ± 0.04	C4	0.25 ± 0.12	-1.36

4) Sensor Effect Size Between Conditions: Table XI shows the effect sizes between the mean temperature increase values of the sensor conditions. A medium effect size can be found between Conditions 1 and 3 (d=-0.69) and between Conditions 2 and 4 (d=-0.73). Between the remaining conditions, a large effect size can be found. The largest effect size is between Conditions 1 and 2 (d=-2.54).

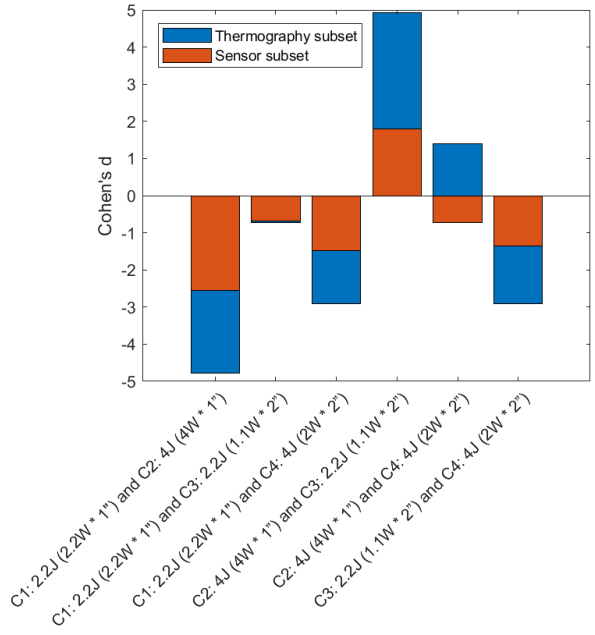

Fig. 35. Thermography and sensor effect sizes between conditions

D. Effect Sizes Between Thermography Conditions and Between Sensor Conditions

The effect sizes between the thermography conditions (blue) and between the sensor conditions (orange) are displayed in Figure 35. The effect sizes between Conditions 1 and 2, between Conditions 1 and 3, between Conditions 1 and 4, and between Conditions 3 and 4 are negative for both the thermography and the sensor measurements. The effect sizes between Conditions 2 and 3 are positive for both the thermography and the sensor measurements. Between Conditions 2 and 4, the thermography subset effect size is positive and the sensor effect size is negative. In both the thermography measurements as the sensor measurements, the effect sizes

between Conditions 1 and 3 and between Conditions 2 and 4 show smaller effect sizes than between the other conditions.

E. Error and Mean Temperature Increase of Thermography and Sensor Conditions

Figure 36, shows the mean thermography and sensor temperature increase and the error per condition. In this comparison, only the measurements that are included in both thermography and sensor analysis are included (see the list of subset measurements in Appendix R).

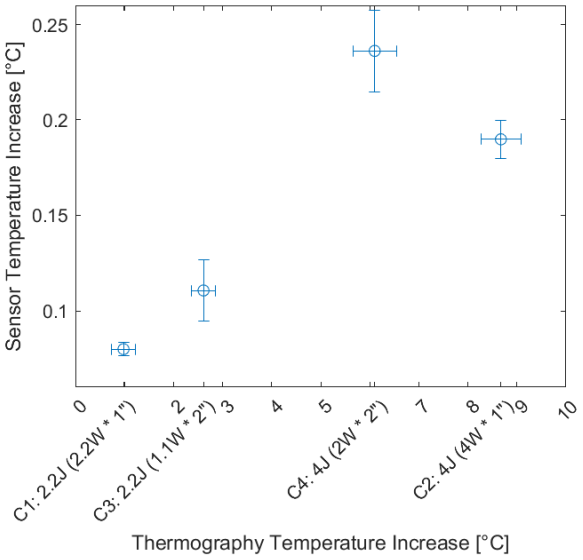

Fig. 36. Mean and standard error of thermography temperature increase values per condition plotted against mean and standard error of sensor temperature increase values per corresponding condition

The mean temperature increase of Condition 1 the lowest for both the thermography subset (0.98 ± 0.35°C, standard error (SE)=0.25) and sensor subset (0.08 ± 0.00°C, SE=0.00). The second lowest mean temperature increase is found Condition 3 at both the thermography subset (2.61 ± 0.65°C, SE=0.25) and the sensor subset (0.11 ± 0.04°C, SE=0.02). The highest mean temperature increase of the thermography subset is found in Condition 2 (8.67 ± 1.74°C, SE=0.41) while the highest mean temperature increase of the sensor subset is at Condition 4 (0.24 ± 0.09°C, SE=0.02).

IV. Discussion

A. Evaluation of results

1) Heating Duration Until Maximum Temperature: The small effect sizes between Conditions 1 and 2 (d=0.23) and between Conditions 3 and 4 (d=-0.41) indicate that difference in mean duration, until the maximum temperature is reached, between the conditions with the same application time are small. Therefore, the application time can be expected to be indicative of the duration until the maximum temperature. The large effect sizes between conditions with different application times verifies that the duration until the maximum temperature is independent to the energy value.

An evaluation of the total heating duration can be found in Appendix S

2) Thermography Condition Evaluation: As seen in Table VII, the thermography conditions with an energy of 2.2 J appear to show a lower mean temperature increase than conditions with an energy of 4 J. This indicates that the theoretical expectation that more energy produces more heat in the tissue is correct.

At an energy of 2.2 J, Condition 3, which has a higher application time, shows a higher mean temperature increase. At an energy of 4 J, Condition 2, which has a higher power setting, shows a higher mean temperature increase. To explain this contradictory observation, the precision of the time application could be questioned. It might be the case that the intended application time of 1" is actually applied longer at Condition 2, resulting in more heat. However, this argument can presumably be rejected using the suggestion that the duration, until the maximum temperature is reached, is indicative of the application time. Because the mean duration, until the maximum temperature is reached, of Condition 4 (41 ± 9 frames) is more than twice as long as Condition 2 (19 ± 6 frames), it is not expected that the fourth condition is actually applied less than the intended 2".

Another explanation for the contradictory observation could be that with an application time of 1", the energy of Conditions 1 (2.2 J) is too short to let the higher power manifest in heat. This would indicate that the energy value of 2.2 J is too low in order to draw conclusions about the influence of power and application time on the thermography temperature increase measurements, within this energy condition.

Although the medium effect size between Conditions 1 and 3 is less significant than the large effect sizes between Conditions 2 and 4, the effect sizes verify that there is a difference in the mean temperature increase between conditions with the same energy value.

3) Sensor Condition Evaluation: The sensor conditions with energy of 2.2 J, appear to show lower mean temperature increase, than conditions with energy of 4 J. This indicates that the sensor at a height of 5.5 mm is able to measure more heat resulting from higher energy.

The conditions with a higher application time show a higher mean temperature increase. This indicates that the application time has a larger influence on the measured heat.

The question is whether the application time has a larger dependency in the actual conversion to heat, as is also suggested in early research by Kalkwarf et al. [39], or that the sensor system is more sensitive at longer application times leading to higher measured temperatures. An additional experiment could answer this question.

Between the mean temperatures of Conditions 1 and 3, and between the mean temperatures of Conditions 2 and 4, a medium effect size is found, which indicates that the differences between the conditions with the same energy value are present, but not as significant as the differences between conditions with unequal energy values.

4) Comparison of Effect Sizes Between Thermography Conditions and Between Sensor Conditions: At the thermography measurements there is only a medium effect between Conditions 1 and 3, while at the sensor measurement, a medium effect is found between Conditions 1 and 3, and between Conditions 2 and 4. This indicates that using the same energy value of 4J only has a minor influence on the resulting heat.

The effect size between Conditions 2 and 4 is negative for the sensor measurements, while the effect size between these conditions is positive for the thermography measurements. This is not in line with the signs of the remaining effect sizes, which are equal. As this equality is a minimum requirement for stating that the upper contactless sensor could be used to infer the temperature increases directly on the retina, this comparison indicates that the sensor cannot infer the thermography measurements.

5) Comparison of Error Within Thermography Conditions and Within Sensor Conditions: For the thermography subset, Conditions 1 and 3 show similar standard error values (SE=0.25). Furthermore, the standard errors of Conditions 2 and 4 are comparable (SE=0.41 and SE=0.45, respectively). This could imply that the error is constant for each energy condition and that a higher energy value leads to a larger standard error. An additional experiment with more energy conditions could verify this implication. This trend is not seen at the sensor subset, at which the standard error values are varying. At the sensor subset, the standard error values at the conditions with a higher application time, is higher than at the conditions with a higher power setting. This implies that, at longer application times, the sensor is more sensitive to changes in the measurements. However, as there are many varying factors, including the different energy, power and application settings, the height of the sensor and the conductivity of the Decalin fluid, it is difficult to prove this implication.

The low sensor error in Condition 1 may imply that this condition provides accurate results. However, as this condition only consists of two measurements, it can be expected that the low error is coincidental.

In conclusion, no similar trend is seen between the error values of the thermography subset and the sensor subset. Comparison of Error and Mean Temperature Increase

6) Evaluation of Compared Mean Temperature Increases: In Figure 36 can be seen that the lowest and second lowest mean temperature increase is found in Conditions 1 and 3, respectively. This applies to both the thermography and sensor measurements, which is a first indication of a positive correlation. However, since the highest mean temperature increase in the thermography measurements is found in a different condition than at the sensor, there is no positive correlation.

Based on the mean temperature increases of Conditions 1 and 3 at both the thermography subset and the sensor subset, it is indicated that the application time has a greater dependence on the mean temperature increase at an energy of 2.2 J.

At the sensor subset, the application time also seems to have a larger dependency on the mean temperature increase using an energy of 4 J, while at the thermography subset, it is the higher power that leads to a higher mean temperature increase at an energy of 4 J.

The contradicted mean temperature increase values explain the contradictory signs of effect size between Conditions 2 and 4 (described in subsubsection IV-A4). As the higher energy condition of 4 J is a better condition for observing coagulation effect as 2.2 J, because the low sensor measurement inclusion rate of this lower energy condition, the contradictory effect between between the 4 J conditions cannot be neglected. Consequently, we can conclude that it is impossible to infer the direct tissue temperature by the contactless sensor measurement at a height of 5.5 mm above the coagulation site, with the conditions used in this experiment.

B. Limitations

In this work, there are several limitations with regard to the design of the whole measuring system, the execution of the experiment and the data analysis.

1) Limitations System Design: For the assembly of the experiment setup, a more recent iteration of the hollow box was intended to be used. However, the guiding rods of the multi-sensor could not fit through the guiding holes because of a 3D-print failure, resulting in the holes being clogged with hardened resin. Consequently, the older iteration of the hollow box, which is described in subsubsection II-C2, was actually used during the experiment. This presumably did not affect the temperature results. However, it decreased the ease of use of the experiment setup because the wall thickness was thinner, leading to weaker tape adhesion with Decalin leaks as result. Additionally, as the fluid level indication inlet of the used hollow box is located at an incorrect height of 22 mm, the amount of Decalin inserted in the box could not be controlled easily. Finally, to prevent vertical movement of the upper guiding rod of the multi-sensor, which the more recent hollow box accounted for, the guiding rods are taped to each other outside the hollow box.

Although the vertical movement of the multi-sensor is prevented using the tape, the axial rotation around the two guiding rods could not be prevented. This led to an unstable positioning of the multi-sensor during the experiment. This provided the opportunity to guide the diathermy probe to a blood vessel in the retina sample.

Because the thickness of the double-sided tape between the hollow box and the window during the experiment, is not taken into account in this design calculation, the lowest sensor is located 22 mm further away from the coagulation site, presumably resulting in a lower sensor measurement inclusion rate. Additionally, the probe tip could not be forced to coagulate exactly in line with the vertical sensors. However, as the diathermy probe guiding ring had a large tolerance, the angle of the probe was not entirely fixed. When located above the blood vessel, it was difficult to visually determine if the probe tip was in vertical line with the sensors.

The time response of the NTC sensors in liquids is 200 milliseconds, which means that the set loop time of 43 milliseconds is too low for the multi-sensor. This might have affected the sensor results.

2) Limitations Experiment: The loss of Decalin due to poor adhesion of the window to the hollow box, the longer sample preparation, data acquisition and data saving time led to a smaller sample size of the second repetitions. As there was no backup Decalin fluid present during the experiment, the Decalin fluid height decreased after each leak. After three times of Decalin leakage, only three sensors could be covered with the fluid at the last acquisition. Because only the lowest sensor is capable of providing sufficient temperature peaks, the reduction of the Decalin fluid is not considered a major limitation. However, it changed the environmental conditions during the experiment, which could have affected the temperature results.

Before coagulation in each measurement, the guidance of the diathermy probe to a blood vessel was somewhat difficult, because the sight through the Decalin fluid was obstructed by the small test environment and the light reflection on the Decalin fluid surface. It was also difficult to keep the multi-sensor at the predefined step along the guiding rods.

Because the porcine retina has a similar vascular micro structure as the human retina [31], and the mean thickness of the human retinal vein, at a distance of 1440 µm from the optic nerve, is 137.69 µm (SD=15.22, n=58) [42], it can be assumed that the blood vessels of the pig retina have a maximum diameter of 138 µm. This contributed to the difficulty of coagulation, as the thin vessels are hardly visible.

3) Limitations Data Analysis: From the thermal images it appears that the retina could be distinguished from the Decalin fluid around it, which indicated that the retina is acclimatized to the Decalin fluid temperature and has the same temperature as the Decalin fluid or that a small layer of Decalin is located between the lower surface of the retina and the window. However, as the Decalin fluid pushes the retina sample against the window surface, it can be expected that the thickness of the fluid layer is this case would be thin. Hence, this limitation does not label the results as unreliable.

C. Future Prospects

1) Additional Thermography Validation: The lower thermography method can be further validated to show that the lower retina surface temperature really represents the upper retina surface temperature. For this purpose, the existing data of the safe maximum energy determination test, at which the lower surface temperature is also measured with the thermal camera (see subsubsection II-F4), could be consulted.

2) Experiment Protocol Optimization: Although in this experiment, no correlation was found between the thermography and the sensor data, an improved version of this experiment could be performed to investigate if the contactless sensor could infer what directly is happening at the tissue under different conditions. Moreover, it could be investigated whether trends within the thermography and sensor measurement at this experiment, also would appear in a similar experiment. More specifically, a similar test could provide more insight into whether the application time has a larger dependency in the actual conversion to heat or that the sensor system itself is more sensitive at longer application times.

Based on the limitations of this work, several improvements can be suggested. For the definition of conditions, we recommend to use a higher normal energy value than 2.2 J. To limit the amount of varying factors and to eliminate the contradictory influence of the application time on the resulting heat and on the sensor sensitivity, we recommend to use a constant application time and to apply energy increments by increasing the power setting. Additionally, the loop time of the sensor acquisition (and thermography acquisition, if possible) should be equal to the time response of the sensors in liquids (200 milliseconds).

3) Design Improvements: Figure 37 displays a design improvement of the hollow box, which was indented to be used in our experiment. This design has an inlet for fluid level indication at a height of 20 mm, which is the intended depth of the Decalin fluid. This is based on the depth from the iris to the back of the human eye (19.98 mm, see subsection II-A). The wall thickness of this box is 3 mm, providing a larger surface to successfully adhere the double-sided tape. Another possible design improvement is that the upper guiding inlets are replaced by holes, so the upper guide rod cannot move in the vertical direction, and the fixation of both guide rods with tape might not be needed.

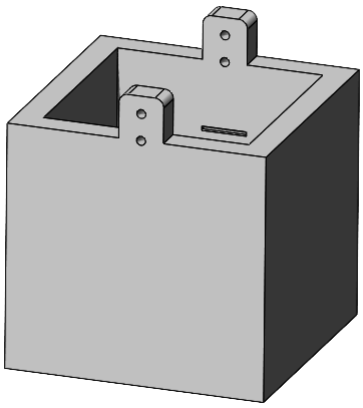

Fig. 37. Design improvement of the hollow box

A possible design improvement of the multi-sensor, is to locate the guide rods 2 mm higher, as the thickness of the double-sided tape in between the hollow box and the window are not accounted for in the current sensor holder design. Furthermore, we recommend redesigning the fixation method multi-sensor, because in the current design, the freedom of movement around the guiding rings and along the guide rods is too large.

For a similar experiment, we recommend developing a method to visualize the coagulation so that the denaturation spot can be evaluated. This method could involve a microscope or a (real-life) camera with a zooming function.

4) Focus on Thermal Spread: In the experiment analysis, we merely focused on temperature increase. However, since thermal spread is indicative of lateral tissue damage, it could

be interesting to investigate the thermal spread by using the standard deviation of the temperature images and the histogram data provided in Appendix P, or by performing a similar experiment.

Optimization of thermal spread measurement could possibly solve an existing medical problem. This problem concerns the safe distance to the optic nerve to apply diathermy. Diathermy cannot be applied on the retina too close to the optic nerve, as patients could be blinded when lateral heat denatures nerve tissue. Currently, there are no protocols or rules for the safe distance from the coagulation site to the optic nerve. Surgeons speculate about this safe distance and do not take risks and let bleeding occur, which blocks sight (Van Overdam, personal communication, November 05, 2021). If the safe thermal spread of instrument could be decreased and measured in a similar experiment, instruments could be used close to the optic nerve or a protocol for safe diathermy application distance to the optic nerve could be created.

5) Clinical Trial: It might be interesting to eventually measure temperature and thermal spread in a clinical trial. The sensors used in this experiment have a diameter of 0.5 mm, which could be difficult to place on a diathermy probe or other intraocular tool. Although the sensor are recommended for application of medical catheters [34], it should be questioned whether the use of such a sensor actually is biocompatible and suited for intraocular use. If a separate measuring instrument solely containing a sensor would meet the latter requirements, such a tool might be inserted through an adjacent cannula next to the diathermy instrument. In this setup, the sensor could be located near the site of coagulation which could allow for internal measurements. During this clinical experiment, optical coherence tomography could be used to evaluate histological effects in a cross-sectional view of the retina [43].

6) Additional Application Areas: In addition to the application in the intraocular diathermy area, (components of) the heat measurement system provided in this paper might be used in other (surgical) areas. Because the test environment of this system a tissue-fluid interface, a similar experiment could be performed at similar surgical sites, such as cerebrospinal fluid which is in contact with the ventricular surface [44]. Furthermore, researchers of other micro surgical areas could be inspired by the measurement methods of this thesis.

V. Conclusion

The aim of this thesis was to investigate whether and to what degree contactless heat measurements can be used to infer what thermal effects are arising at the coagulation site of a diathermy probe inside the eye.

We developed a measurement system containing a lower thermography method and an upper contactless sensor, which can individually measure the higher temperature resulting from higher energy values.

The use of a normal energy of 2.2 J appears to be too low for proper sensor temperature peak identification and comparison between conditions with the same energy of 2.2 J.

For conditions with a safe maximum energy of 4 J, there is a contradictory indication of the influence of application time in thermography measurements versus sensor measurements. It is expected that sensor is more sensitive to changes in the application time than the thermal camera.

In conclusion, since no similar trends have been observed between effects sizes, between errors, and between means of temperature increases, it can be concluded that the contactless sensor cannot infer the direct tissue temperature at a height of 5.5 mm above the coagulation site on the lower retinal surface, with the conditions used in this experiment.

VI. Acknowledgements

First of all, I am thankful for Dimitra, for supervising me during my thesis. She always was positive and supportive, while understanding my doubts and the difficulties I encountered. For a long time, it seemed impossible to achieve this, but for Dimitra it was clear that I could do this from the beginning.

The TU Delft (financially) supported me for the materials of the design. In particular, Jos helped me with the assembly and programming of the sensors. I would like to thank Paddy for inspiring me for the measuring system.

I am thankful for Koen, for all the interesting conversations we had about the topic and his help with the instrumentation, although I did not end up improving his diathermy forceps, with which I wish him luck. Without his help I would not have succeeded.

The Rotterdam Eye Hospital provided materials and a test lab, for which I am thankful. I would like to thank Daniel, Mart, Boyd, Valentin and Luc, for helping me with experiments, materials, and advice on the topic.

I am very grateful to all the people who supported me during this long period of graduation. In particular Kris, for giving me positive energy, Berna, for being my thesis partner in crime, Timo, for giving his unexpected life advice, Rob, for strengthening my 'ikje', my grandparents, for always being proud, JvB 61, for still being a family, Mathilde, for always giving me advice, Noor, for checking up on me at difficult times, Abe, for providing a sympathetic ear and Nienke, who I appreciate, despite everything that has happened, for the mental support she gave me.

During the periods in which my thesis and my personal life were very tough, my father always was there for me. I appreciate him for everything he has done for me and I wish him all the best in his open future.

From the sixteenth of august, the world is my oyster. I am proud of myself for keeping my head up, while fantasizing about helping future parents have their babies. I am excited to explore whether my path will lead to this fantasy or if there will come a day when I feel like a real biomedical engineer.

References

[1] Arash Taheri, Parisa Mansoori, Laura F. Sandoval, Steven R. Feldman, Daniel Pearce, and Phillip M. Williford. Electrosurgery: Part I. Basics and principles. *Journal of the American Academy of Dermatology*, 70 (4):591.e1–591.e14, Apr 2014. ISSN 0190-9622. doi: 10.1016/j.jaad.2013.09.056.

[2] Nicolas Aigner, Christian Fialka, Angelika Fritz, Otto Wruhs, and Gerald Zöch. Complications in the use of diathermy. *Burns*, 23(3):256–264, 1997. ISSN 0305-4179.

[3] W. J. Turrell. Treatment by Diathermy. *Br Med J*, 1 (3239):143–145, Jan 1923. ISSN 0007-1447, 1468-5833. doi: 10.1136/bmj.1.3239.143.

[4] Jean-Marie Parel, Robert Machemer, Guy E. O'Grady, Gerard W. Crock, and Izuru Nose. Intraocular diathermy coagulation. *Graefe's Archive for Clinical and Experimental Ophthalmology*, 221(1):31–34, Aug 1983. ISSN 1435-702X. doi: 10.1007/BF02171728.

[5] Jean-Marie Parel, Guy E. O'Grady, and Robert Machemer. A Bipolar Coaxial Microprobe for Safe Transvitreal Diathermy. *Archives of Ophthalmology*, 99(3):494–497, Mar 1981. ISSN 0003-9950. doi: 10.1001/archopht.1981.03930010496024.

[6] Robert Machemer. Transvitreal radiofrequency diathermy. *American journal of ophthalmology*, 83 (2):282, 1977.

[7] Koen A. van Overdam, Emine Kilic, Robert M. Verdijk, and Sonia Manning. Intra-ocular diathermy forceps. *Acta Ophthalmologica*, 96(4):420–422, Jun 2018. ISSN 1755375X. doi: 10.1111/aos.13619.

[8] Koen A. van Overdam, Tom Missotten, Emine Kilic, and Leigh H. Spielberg. Early surgical treatment of retinal hemangioblastomas. *Acta Ophthalmologica*, 95(1):97–102, 2017. ISSN 1755-3768. doi: 10.1111/aos.13223.

[9] Koen-Willem Adriaan van Overdam, Jun 2017. WO Patent 2017/102975 A1.

[10] Koen Overdam, Jerrel Pawiroredjo, Dinesh Jiawan, and Sonia Manning. First-in-human study of the safety, effectiveness and ease of use of the intra-ocular diathermy forceps during vitrectomy. *Acta Ophthalmologica*, 97(8), Dec 2019. ISSN 1755-375X, 1755-3768. doi: 10.1111/aos.14134. URL https://onlinelibrary.wiley.com/doi/abs/10.1111/aos.14134.

[11] Susan Roweton, Beth Johnson, Julie Kurtenbach, G. Young, and J. Dunne. Comparison of Two Histological Test Methods for the Measurement of Thermal Spread Associated With Energized Vessel Sealing. *Journal of Testing and Evaluation*, 44:20140233, May 2016. doi: 10.1520/JTE20140233.

[12] *Regulation (EU) 2017/745 of the European Parliament and of the Council*, volume 117. Apr 2017. URL http://data.europa.eu/eli/reg/2017/745/oj/eng.

[13] J. M. Parel, R. Machemer, and W. Aumayr. A new concept for vitreous surgery. 4. Improvements in instrumentation and illumination. *American Journal of Ophthalmology*, 77(1):6–12, Jan 1974. ISSN 0002-9394.

[14] Kirwan Surgical Products. BIPOLAR PENCILS. URL http://www.ksp.com/product/bipolar-pencils. Accessed: April. 29, 2021.

[15] Lawrence T. Kirwan Jr. Disposable bipolar coagulator, Feb 1992. URL https://patents.google.com/patent/US5089002A/en?oq=+5%2c089%2c002%2c. US Patent 5,089,002 A.

[16] DORC. Endo-diathermy handle, straight pointed tip. (23 gauge / 0.6 mm). URL https://dorcglobal.com/product/endo-diathermy-handle-straight-pointed-tip-23-gauge-06-mm. Accessed: Apr. 14, 2021.

[17] M. Shiwa and T. Kishi. *NDT-based Assessment of Damage: An Overview*, page 1–8. Elsevier, Jan 2005. ISBN 978-0-08-043152-9. doi: 10.1016/B0-08-043152-6/02032-5. URL https://www.sciencedirect.com/science/article/pii/B0080431526020325.

[18] P. A. Campbell, A. B. Cresswell, T. G. Frank, and A. Cuschieri. Real-time thermography during energized vessel sealing and dissection. *Surgical Endoscopy*, 17 (10):1640–1645, Oct 2003. ISSN 0930-2794, 1432-2218. doi: 10.1007/s00464-002-8781-2.

[19] Nermin K Negied. Human biometrics: Moving towards thermal imaging. *International Journal of Recent Technology and Engineering (IJRTE)*, 2(6), 2014.

[20] FLIR. ResearchIR 4 User's Guide, Feb 2015. URL https://assets.tequipment.net/assets/1/26/FLIR_ResearchIR_User_Manual.pdf. Accessed: April. 22, 2022.

[21] Robert Dodde, Albert Shih, and Arnold P. Advincula. A novel technique for demonstrating the real-time subsurface tissue thermal profile of two energized surgical instruments. *Journal of Minimally Invasive Gynecology*, 16(5):599–603, Sep 2009. ISSN 1553-4650. doi: 10.1016/j.jmig.2009.05.018.

[22] C. Crean, C. Mcgeouge, and R. O'kennedy. *11 - Wearable biosensors for medical applications*, page 301–330. Woodhead Publishing Series in Biomaterials. Woodhead Publishing, Jan 2012. ISBN 978-1-84569-935-2. doi: 10.1533/9780857097187.2.301. URL https://www.sciencedirect.com/science/article/pii/B9781845699352500115.

[23] KAI Siren, GUNNAR Rosén, JÁNOS Vad, and PETER V. Nielsen. *12 - EXPERIMENTAL TECHNIQUES*, page 1105–1195. Academic Press, Jan 2001. ISBN 978-0-12-289676-7. doi: 10.1016/B978-012289676-7/50015-1. URL https://www.sciencedirect.com/science/article/pii/B9780122896767500151.

[24] Ignace T. C. Hooge, Diederick C. Niehorster, Roy S. Hessels, Dixon Cleveland, and Marcus Nyström. The pupil-size artefact (psa) across time, viewing direction, and different eye trackers. *Behavior Research Methods*, 53(5):1986–2006, Oct 2021. ISSN 1554-3528. doi: 10.3758/s13428-020-01512-2.

[25] Helga Kolb. *Facts and Figures Concerning the Human Retina*. University of Utah Health Sciences Center, Salt Lake City (UT), 1995. URL http://www.ncbi.nlm.nih.gov/books/NBK11556/.

[26] Kishore Cholkar, Supriya Reddy Dasari, Dhananjay Pal, and Ashim K. Mitra. *1 - Eye: anatomy, physiology and barriers to drug delivery*, page 1–36. Woodhead Publishing Series in Biomedicine. Woodhead Publishing, Jan 2013. ISBN 978-1-907568-86-2. doi: 10.1533/9781908818317.1. URL https://www.sciencedirect.com/science/article/pii/B9781907568862500010.

[27] Renoh Johnson Chalakkal, Waleed Habib Abdulla, and Sheng Chiong Hong. *3 - Fundus retinal image analyses for screening and diagnosing diabetic retinopathy, macular edema, and glaucoma disorders*, page 59–111. Computer-Assisted Diagnosis. Elsevier, Jan 2020. ISBN 978-0-12-817440-1. doi: 10.1016/B978-0-12-817440-1.00003-6. URL https://www.sciencedirect.com/science/article/pii/B9780128174401000036.

[28] Thorlabs. Germanium Windows, n.d.. URL https://www.thorlabs.com/newgrouppage9.cfm?objectgroup_id=3980. Accessed: Feb. 24, 2022.

[29] Steven G. Kramer, David Hwang, Gholam A. Peyman, Joel A. Schulman, and Brian Sullivan. Perfluorocarbon liquids in ophthalmology. *Survey of Ophthalmology*, 39 (5):375–395, Mar 1995. ISSN 0039-6257. doi: 10.1016/S0039-6257(05)80093-1.

[30] Jasenka Guduric-Fuchs, Laura J. Ringland, Ping Gu, Margaret Dellett, Desmond B. Archer, and Tiziana Cogliati. Immunohistochemical study of pig retinal development. 15:1915–1928, Sep 2009. ISSN 1090-0535.

[31] Mihyun Choi, Seong-Woo Kim, Somin Ahn, Thi Que Anh Vu, Cheolmin Yun, and Yong Yeon Kim. Relationship between retinal capillary vessel density of oct angiography and intraocular pressure in pig. *Scientific Reports*, 11(11):8555, Apr 2021. ISSN 2045-2322. doi: 10.1038/s41598-021-87689-8.

[32] Openworldlearning. What 3d Printer Process Technology Is Waterproof?, n.d. URL https://formlabs.com/blog/ultimate-guide-to-stereolithography-sla-3d-printing/. Accessed: Aug. 09, 2022.

[33] J. Arevalo, Maria Berrocal, Juan Arias, and Touka Banaee. Minimally invasive vitreoretinal surgery is sutureless vitrectomy the future of vitreoretinal surgery? *Journal of ophthalmic vision research*, 6:136–44, Apr 2011.

[34] TE Connectivity. MICRO-BETACHIP (MCD), Sep 2015. URL https://nl.mouser.com/datasheet/2/418/8/ENG_DS_MCD_10K3MCD1_A-2940474.pdf. Accessed: Dec. 09, 2021.

[35] Boyd Riemens. Safety of Intraocular Diathermy Forceps, Dec 2020. Internship Report Delft University of Technology.

[36] Narinder Kumar. *Comprehensive Physics XII*. Laxmi Publications, 2004. ISBN 978-81-7008-592-8. Google-Books-ID: yGjmnAAACAAJ.

[37] Laurent Schoevaerdts, Gianni Borghesan, Mouloud Ourak, Dominiek Reynaerts, and Emmanuel Vander Poorten. Electrical Bio-Impedance Proximity Sensing for Vitreo-Retinal Micro-Surgery. *IEEE Robotics and Automation Letters*, 4(4):4086–4093, Oct 2019. ISSN 2377-3766. doi: 10.1109/LRA.2019.2930482.

[38] Mark Holker. *27 - Radiowave propagation*, page 27–1. Butterworth-Heinemann, Jan 1993. ISBN 978-0-7506-1162-6. doi: 10.1016/B978-0-7506-1162-6.50033-2. URL https://www.sciencedirect.com/science/article/pii/B9780750611626500332.

[39] Kenneth L Kalkwarf, Robert F Krejci, and Allen R Edison. A method to measure operating variables in electrosurgery. *Journal of Prosthetic Dentistry*, 42(5): 566–570, 1979.

[40] MathWorks. Image Types, n.d.. URL https://nl.mathworks.com/help/matlab/creating_plots/image-types.html. Accessed: Aug. 02, 2022.

[41] Jacob Cohen. A power primer. *Psychological Bulletin*, 112(1):155–159, 1992. ISSN 1939-1455. doi: 10.1037/0033-2909.112.1.155.

[42] Dafna Goldenberg, Jonathan Shahar, Anat Loewenstein, and Michaella Goldstein. DIAMETERS OF RETINAL BLOOD VESSELS IN A HEALTHY COHORT AS MEASURED BY SPECTRAL DOMAIN OPTICAL COHERENCE TOMOGRAPHY. *RETINA*, 33 (9):1888–1894, Oct 2013. ISSN 0275-004X. doi: 10.1097/IAE.0b013e31829477f2.

[43] C. Lamirel. *Optical Coherence Tomography*, page 660–668. Academic Press, Oxford, Jan 2014. ISBN 978-0-12-385158-1. doi: 10.1016/B978-0-12-385157-4.00171-8. URL https://www.sciencedirect.com/science/article/pii/B9780123851574001718.

[44] Maria K. Lehtinen and Christopher A. Walsh. Neurogenesis at the brain–cerebrospinal fluid interface. *Annual review of cell and developmental biology*, 27:653–679, 2011. ISSN 1081-0706. doi: 10.1146/annurev-cellbio-092910-154026.

[45] Edmund Optics. The Correct Material for Infrared (IR) Applications, n.d. URL https://www.edmundoptics.com/knowledge-center/application-notes/optics/the-correct-material-for-infrared-applications/. Accessed: Feb. 24, 2022.

[46] Tydex. Silicon, n.d. URL http://www.tydexoptics.com/materials1/for_transmission_optics/silicon/. Accessed: Feb. 25, 2022.

[47] Daniel Csati, n.d. URL https://diy-optics.com/. Accessed: Feb. 22, 2022.

[48] MICRO-EPSILON. thermoIMAGER TIM // Compact thermal imaging cameras, Oct 2017. URL http://web.archive.org/web/20171024162247/http://www.micro-epsilon.co.uk/download/products/_thermoimager/dax--thermoIMAGER-TIM-400-450--en.html. Accessed: Feb. 25, 2022.

[49] Thorlabs. Zinc Selenide (ZnSe) Windows, n.d.. URL https://www.thorlabs.com/newgrouppage9.cfm?objectgroup_id=3981. Accessed: Aug. 07, 2022.

[50] Crystran. Zinc Sulphide Multispectral (Zinc Sulfide) (ZnS), n.d. URL https://www.crystran.co.uk/optical-materials/zinc-sulphide-multispectral-zinc-sulfide-zns. Accessed: Aug. 07, 2022.

[51] Hyperion Optics. ZnSe ZnS window, n.d. URL

http://www.hypoptics.com/components/windows/znse-zns-window.html. Accessed: Aug. 07, 2022.

[52] Gary Orlove (Infrafred Training Center). Easy IR Window Transmission Measurement, n.d. URL https://flir.custhelp.com/ci/fattach/get/9908/0/filename/Tech+Pub+-+Easy+Window+Transmission+Measurement.pdf. Accessed: Apr. 22, 2022.

[53] MathWorks. filloutliers, n.d.. URL https://nl.mathworks.com/help/matlab/ref/filloutliers.html?s_tid=doc_ta. Accessed: Aug. 02, 2022.

[54] MathWorks. medfilt1, n.d.. URL https://nl.mathworks.com/help/signal/ref/medfilt1.html?s_tid=doc_ta. Accessed: Aug. 02, 2022.

[55] MathWorks. lowpass, n.d.. URL https://nl.mathworks.com/help/signal/ref/lowpass.html?searchHighlight=lowpass&s_tid=srchtitle_lowpass_1#d123e102556. Accessed: Aug. 02, 2022.

APPENDIX

APPENDIX A
PROJECT DEFINITION

To determine the focus of this thesis, we explored several research areas originated from the literature review, which is conducted prior to this thesis. In a meeting with Gahler from the Dutch Ophthalmic Research Center, and in several meetings with eye surgeon Van Overdam from the Rotterdam Eye Hospital, we discussed these research areas. Further more, we explored and questioned possible thesis projects on its medical contribution and its (dis)advantages. All this information is gathered in Figure 38. By combining different components of this diagram, we determined the aim of this thesis project.

The diagram can also be downloaded via this link.

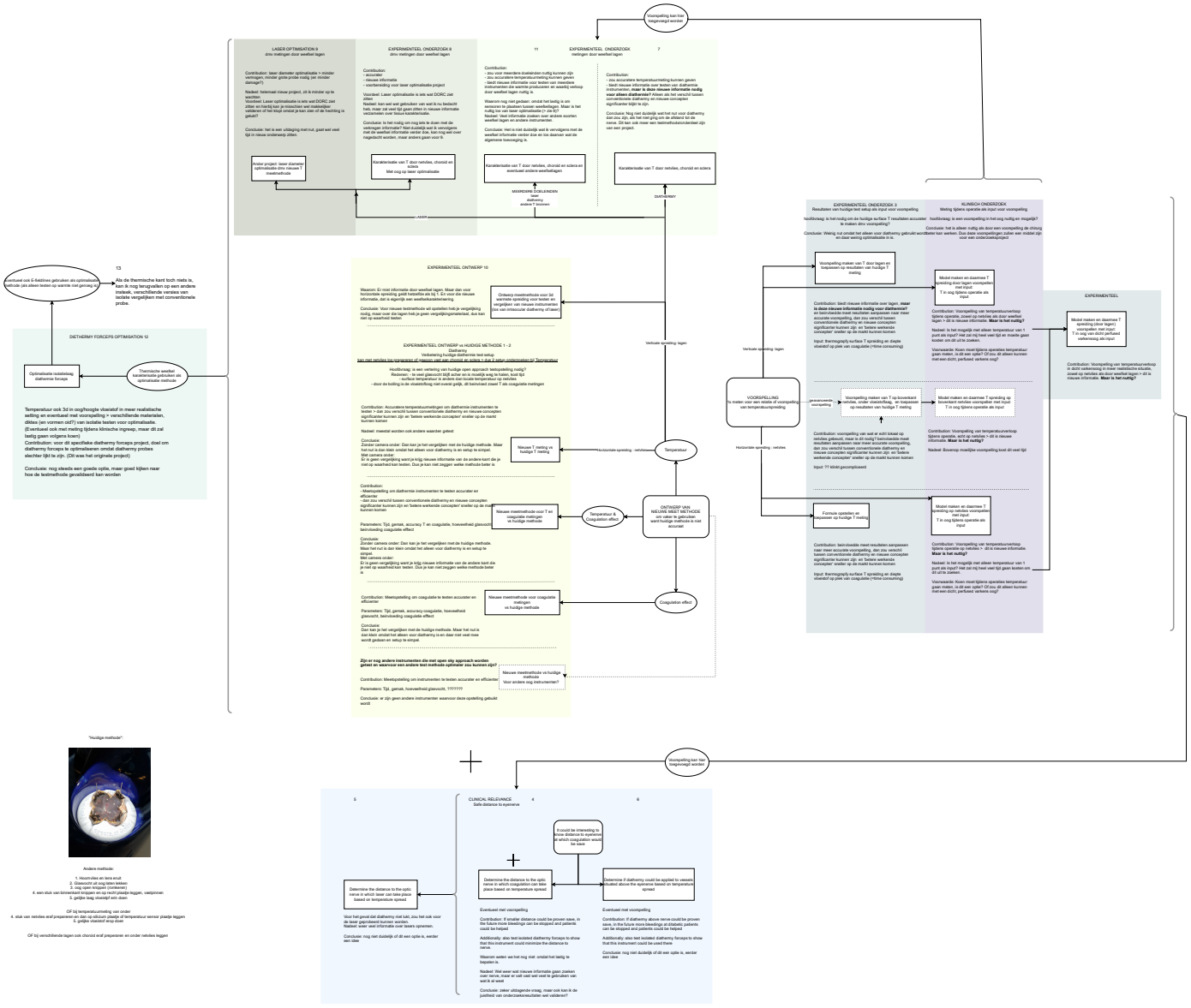

Fig. 38. Thesis focus choice progress diagram

APPENDIX B
WAFER MATERIAL CHOICE PROCESS

This appendix provides additional information on the choice of AR-coated germanium as window material.

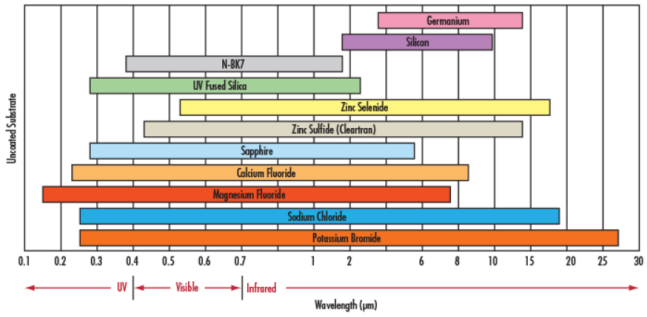

Fig. 39. Spectral ranges of IR materials. Figure adapted from [45]

In order to identify suitable material(s) for the IR window, first a selection of potential material is done. The materials to be considered are selected according to one of the criteria "IR material used in thermal imaging" [45]) and LWIR transmittance. The latter follows from Figure 39, which displays the spectral ranges in which IR material can be used as window [45]. The first criterion resulted in the materials Germanium, Zinc Selenide, and Zinc Sulfide. These materials also fall in the LWIR range. The second criterion resulted in the addition of Potassium Bromide and Sodium Chloride. Silicon does not fall into the LWIR range completely; however, this material is included in the material selection because it was recommended (personal communication with French, an expert from the TU Delft) to serve as a highly transmitting infrared window. Additionally, it is indicated that silicon windows with a maximum thickness of 1 mm could also be used in the LWIR range [46].

TABLE XII
INFRARED MATERIAL PROPERTIES

Material	**Index of Refraction**	**Density [g/cm3]**	**CTE [x10-6/°C]**	**Knoop Hardness**
Germanium	4.003	5.33	6.1	780
Potassium Bromide	1.527	2.75	43	7
Silicon	3.422	2.33	2.55	1150
Sodium Chloride	1.491	2.17	44	18.2
Zinc Selenide	2.403	5.27	7.1	120
Zinc Sulfide	2.631	5.27	7.6	120

Note. Table adapted from [45]

The thermal properties of the selected window materials are shown in Table XII. Because Potassium Bromide and Sodium Chloride are water soluble and have a Knoop Hardness of 7 and 18.2, respectively, these materials are not suitable as window material.

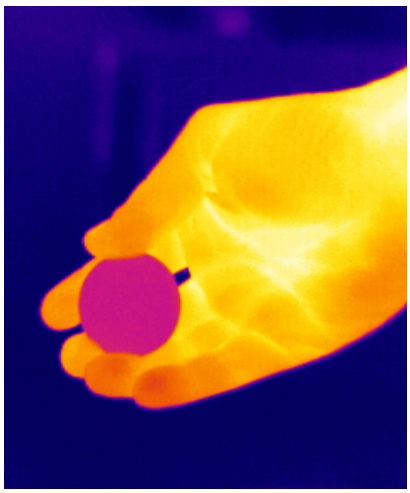

Fig. 40. Infrared transmission of silicon wafer. Figure provided by Csati (personal communication, February 22, 2022).

In a requested test conducted by Csati from DIY Optics [47], it was proved that temperature could not be measured with a TIM400 microbolometer thermography camera with a spectral range of 7.5um-11um [48], through a silicon substrate doped with boron with a thickness of 0.375 mm, as can be seen in Figure 40.

Although Zinc Selenide and Zinc Sulfide have a higher Knoop Hardness, the transmission rate of Zinc Selenide in the LWIR range is below 70% [49] and the transmission rate of Zinc Sulfide is below 80% in the LWIR range [50]. When an anti-reflection (AR) coating is added, the transmission rate of Zinc Selenide in the LWIR range is below 80% [49], which is below the criterion of 85%. A multispectral form of Zinc Sulfide reaches a transmission rate of 100% [50]. However, as Zinc Sulfide still has a low Knoop Hardness, the material is soft and can be scratched easily [51]. This is not a suitable material for the experiment because the window must be repeatedly removed from the double-sided tape with a high tensile force. Furthermore, this material could be scratched by the diathermy probe.

Germanium has a transmission rate below 50% [28]. Anti-reflection coated Germanium provides a transmission rate of 90% in the LWIR range. As this material has a high Knoop Hardness of 780, this material is suitable as window for the experiment in this thesis.

APPENDIX C
TRANSMISSION RATE DETERMINATION METHOD

The transmission rate of the window can be determined by performing a test provided by the Infrared Training Center [52]. The following steps, which are cited from this technical publication must be performed.

"1: Place a few strips of electrical tape on the outside surface of your hot reference object. Avoid overlapping the tape. Allow to sit for about 1 minute to stabilize in temperature.
2: Set the emissivity in your camera to 1.00 and measure the reflected temperature using your flat aluminum foil surface. (This is done by positioning the foil perpendicular to the camera's line of site and at the same distance as the hot object you will be measuring. Measure the temperature of the foil and input this number into your camera's settings menu.
3: Orient the camera directly at the hot reference source and measure the apparent temperature of the electrical tape surface. Write this number down.
4: Quickly place the IR window between the object and the camera. Orient the camera so that it is measuring the electrical tape through the window and freeze the image. If your camera does not have image freezing functionality, perform step 5 as quickly as possible.
5: Change the emissivity setting on your camera until the temperature reading through the window equals the original temperature you wrote down. This emissivity setting is the transmission rate of the window." [52, p. 2-4]

APPENDIX D
CORRECTION FACTOR TESTS

First Test to Determine Correction Factor: The first transmission rate test, based on the steps described in Appendix C, is performed with two cameras, FLIR E96 and FLIR E75. A reflective temperature of 22 is determined as the camera setting. The temperature at which the E75 camera was used ranged from 56.4°C to 52.3°C and the temperature of the E96 ranged from 44.4°C to 42.1°C. The differences between the real temperature of the sample and the temperature measured with the window between the camera and the sample are manually identified on the AVI files noted as follows (<factor>: <actual temperature> <temperature difference with window>):

E75

Video: E75Transmission22_0002.avi
88: 56.4 +0.5

Video: E75Transmission22_0004.avi
89: 54.6 = 0
88: 54.7 -0.2
89: 54.3 +0.1

Video: E75Transmission22_0005.avi
89: 53.6 - 0.1
88: 53.6 - 0.4
88: 53.5 - 0.2
89: 53.2 -0.2
89: 53.2 - 0.2
89: 53.0 - 0.1
88: 53.1 - 0.3
89: 52.9 - 0.3
88: 52.9 - 0.6
89: 52.2 - 0.1
89: 52.3 - 0.1

E96

Video: E96Transmission22_0001.avi
87: 44.4 - 0.7
88: 44.0 - 0.2
89: 43.5 + 0.3
89: 43.4 - 0.1
88: 43.5 - 0.3
89: 43.4 - 0.4
90: 43.0 = 0
90: 43.0 - 0.2
89: 43.2 - 0.5
90: 42.7 = 0
90: 42.4 +0.1
91: 42.3 +0.1
91: 42.1 +0.2

The Matlab script ('FirstWindowFactor.m') which computes the mean and standard deviations of these results can be downloaded via this link. The measurement with a factor of 87% is not included in this analysis because the difference with the actual temperature was too large (0.7°C).

The calculations of the E75 camera result in a mean difference of 0.37 ± 0.16°C at factor 88% and 0.13 ± 0.17°C for factor 89%. The calculations of the E96 camera result in a mean difference of 0.25 ± 0.07°C at factor 88%, 0.33 ± 0.17°C for factor 89%, 0.08 ± 0.10°C for factor 90% and 0.15 ± 0.08°C for factor 91%.

This suggests that for camera E75, a factor of 89% is the most accurate and for camera E96 a factor of 90% is more accurate. However, as this test is done with a decreasing actual temperature, it is not an accurate measuring method. When the emission factor is set up in the camera, the actual temperature can be changed.

Second Test to Determine Correction Factor: Because the water is moved by the stirrer in the second test to determine the correction factor, the temperature of the water at the camera center point, which displays the temperature in the center of the camera, is not constant. Consequently, the temperature values of several measurements are averaged in this test. Each time, the mean center temperature of 25 measurements before the window is positioned is noted as the mean temperature without window. The mean center temperature of 25 measurements after the window is positioned and the correction factor is applied is defined as mean temperature with window. In one exception, only 11 frames are used for the calculation of means. This test is carried out eight times with a factor of 87% (see Table D, six times with a factor of 88% (see Table D and eight times with a factor of 89% (see Figure D.

The Matlab script ('StirrerWindowFactor.m') for these calculation can be downloaded via this link.

The mean and standard deviation of all temperature difference values per correction factor are displayed in Table D.

Third Test to Determine Correction Factor: An additional test is performed at which water is heated until the boiling point, to create a reference temperature which is exact 100°C. The test setup, as shown in Figure 41, consists of a cooking pan filled with hot water which is placed on an induction hob. A thermocouple is placed inside the water, and a FLIR E75 thermal camera is aimed at the surface of the water. The correct emissivity factor for water (0.95) is set up in the camera.

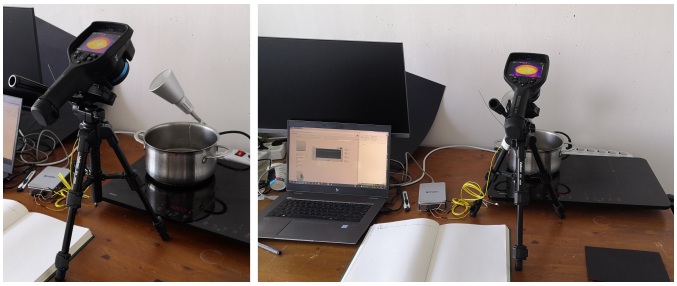

Fig. 41. Experiment setup of boiling test

In practice, the boiling point of the water cannot be determined because the water is not evenly heated and the bubbling

formation starts in a round pattern above the electrical heating element. This makes it impossible to determine the exact boiling point. When heated around boiling point, the water does not have a evenly distributed temperature and the water is moving due to the boiling bubbles. This leads to a highly fluctuating temperature measurement with the thermal camera. Figure 42 displays two thermal image frames that are acquired 43 milliseconds after each other. The temperature difference is 1.6°C. Another downside of this test is that when the temperature is above 100°C, the thermal camera only displays rounded numbers. This may give biased results, as temperature values above 100°C are not accurate and have a higher weight in the calculation of means. Nevertheless, three window factors (88%, 89% and 90%) are tested in this test with the same method as second test described in subsubsection II-B3.

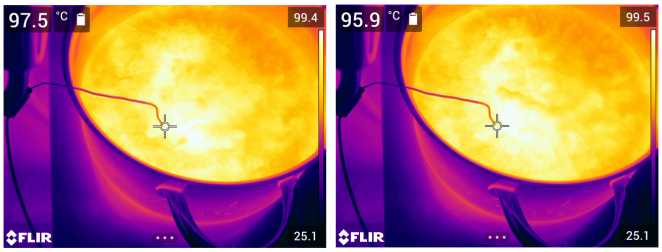

Fig. 42. Experiment setup of stirrer heating test

While the water was boiling, the thermocouple did not reach reach 100°C and resulted in temperatures about 5°C lower than the temperatures measured with the thermal camera. Hence, this instrument is not accurate and results from this instrument are not included. The mean temperatures without window, calculated from 25 frames before the window is positioned, the mean temperatures with window, calculated from 25 frames after the window is positioned and the factor is set, and the temperature differences between these means can be found in Table XVII, Table XVIII and Table XIX.

The mean and standard deviation of all temperature difference values per correction factor are shown in Table XX. The mean temperature difference of the tests with factor 88% is the smallest (1.06 ± 0.40°C). Factor 89% and factor 89% result in a mean difference of 1.21 ± 1.13°C and 1.38 ± 0.99°C, respectively. Although these results may be biased, this indicates that the best correction factor is 88%.

The Matlab script 'BoilingWindowFactor.m' provides all the results of this third test and can be downloaded via this link.

TABLE XIII
WINDOW VALIDATION EXPERIMENT WITH TRANSMISSION FACTOR OF 89

Experiment #	Mean Without Window [°C]	SD Without Window	Mean With Window [°C]	Standard Deviation With Window	Temperature Difference [°C]
1.1	81.96	0.09	81.58	0.40	0.38
1.2	82.39	0.18	81.47	0.15	0.92
1.3	82.66	0.30	79.41	1.45	3.25
1.4	82.21	0.06	82.07	0.27	0.14
1.5	82.45	0.05	80.86	0.44	1.59
1.6	82.45	0.34	81.02	0.40	1.43
1.7	81.15	0.13	80.90	0.21	0.24
1.8	82.45	0.34	81.15	0.09	1.30

TABLE XIV
WINDOW VALIDATION EXPERIMENT WITH TRANSMISSION FACTOR OF 88

Experiment #	Mean Without Window [°C]	Standard Deviation Without Window	Mean With Window [°C]	Standard Deviation With Window	Temperature Difference [°C]
2.1	81.53	0.28	81.68	0.21	-0.15
2.2	81.25	0.05	81.53	0.22	-0.28
2.3	81.20	0.00	81.16	0.35	0.04
2.4	81.42	0.49	80.80	0.00	0.62
2.5	81.13	0.05	80.90	0.25	0.23
2.6	80.90	0.12	80.60	0.00	0.30

TABLE XV
WINDOW VALIDATION EXPERIMENT WITH TRANSMISSION FACTOR OF 87

Experiment #	Mean Without Window [°C]	Standard Deviation Without Window	Mean With Window [°C]	Standard Deviation With Window	Temperature Difference [°C]
3.1	81.18	0.27	82.07	0.56	-0.90
3.2	81.14	0.21	81.92	0.34	-0.78
3.3	80.69	0.23	79.97	0.64	0.72
3.4	80.49	0.23	80.10	0.00	0.39
3.5	80.55	0.25	79.73	0.40	0.82
3.6	79.82	0.20	79.45	0.24	0.38
3.7	79.59	0.23	80.14	0.53	-0.55
3.8[1]	79.88	0.31	79.93	0.36	-0.05

[1] Only 11 frames are used for calculation of means

TABLE XVI
MEAN DIFFERENCE AT TRANSMISSION FACTORS 87, 88 AND 89

Mean Difference 87 [°C]	SD 87	Mean Difference 88 [°C]	SD 88	Mean Difference 89 [°C]	SD 89
0.57	0.29	0.27	0.20	1.16	1.01

TABLE XVII
MEAN AND STANDARD DEVIATION OF- AND DIFFERENCE BETWEEN TEMPERATURE WITH AND WITHOUT WINDOW WITH CORRECTION FACTOR 88

Experiment #	Transmission	Mean Without [°C]	SD Without	Mean With [°C]	SD With	Temperature Difference [°C]
6.7	88.00	99.70	0.99	100.56	0.88	-0.86
6.8	88.00	100.45	0.72	99.82	0.07	0.62
6.19	88.00	99.55	0.32	100.95	1.03	-1.41
6.20	88.00	98.36	0.29	100.02	0.95	-1.66
6.21	88.00	100.52	0.81	99.45	0.38	1.07
6.22	88.00	97.93	0.99	98.68	0.80	-0.75

TABLE XVIII
MEAN AND STANDARD DEVIATION OF- AND DIFFERENCE BETWEEN TEMPERATURE WITH AND WITHOUT WINDOW WITH CORRECTION FACTOR 89

Experiment #	Transmission	Mean Without [°C]	SD Without	Mean With [°C]	SD With	Temperature Difference [°C]
6.5	89.00	99.22	0.29	100.05	0.59	-0.83
6.6	89.00	100.31	0.47	99.48	0.96	0.82
6.9	89.00	99.48	0.26	100.53	0.55	-1.05
6.10	89.00	99.43	0.41	99.71	0.64	-0.28
6.11	89.00	100.85	0.42	100.65	0.49	0.20
6.12	89.00	99.85	0.23	100.58	0.70	-0.73
6.13	89.00	96.69	0.73	100.25	0.57	-3.56
6.14	89.00	101.88	0.33	99.70	0.63	2.19

TABLE XIX
MEAN AND STANDARD DEVIATION OF- AND DIFFERENCE BETWEEN TEMPERATURE WITH AND WITHOUT WINDOW WITH CORRECTION FACTOR 90

Experiment #	Transmission	Mean Without [°C]	SD Without	Mean With [°C]	SD With	Temperature Difference [°C]
6.1	90.00	99.88	0.94	100.07	0.40	-0.19
6.2	90.00	100.54	0.51	100.02	1.03	0.52
6.3	90.00	100.92	0.89	98.34	1.83	2.58
6.4	90.00	100.04	1.03	98.47	0.30	1.57
6.15	90.00	101.46	0.51	99.18	0.68	2.28
6.16	90.00	99.80	0.15	99.00	0.00	0.80
6.17	90.00	101.40	1.25	98.84	0.40	2.57
6.18	90.00	99.19	1.50	99.71	1.44	-0.52

TABLE XX
MEAN AND STANDARD DEVIATION OF DIFFERENCE AT TRANSMISSION FACTORS 88, 89 AND 90

Mean Difference at 88	**SD at 88**	**Mean Difference at 89**	**SD at 89**	**Mean Difference at 90**	**SD at 90**
1.06	0.40	1.21	1.13	1.38	0.99

APPENDIX E
MULTI-SENSOR DESIGN PROCESS

On the recommendation of van Driel (personal communication, December 6, 2021), there must be enough space between the NTC sensor, because otherwise the sensors will influence the heating of the surrounding sensors, which influences their resistance and therefore influences the measured temperatures. Additionally, the sensor holder consists of as little material as possible, so there is less interference with the heating liquid and less heat conductance through the material.

In the multi-sensor design, a vertical alignment of NTC sensors is used. Before this design was developed, another sensor orientation as shown in Figure 43 is explored, which consists of a spiral orientation. This way, there is more distance between the NTCs, so there would be less heating influence between them, and a 3D measurement field can be provided.

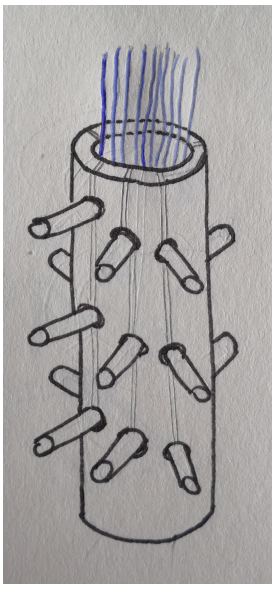

Fig. 43. Spiral sensor holder concept

However, the 3D measuring system would make heating measurement analysis complex and a large heat convection region would be required. Additionally, the design and assembly of such a spiral sensor holder is very complex and more material is needed, which could influence the heat measurements. At last, the location of the diathermy probe should ideally be in the centre of this spiral, so a guiding shaft in the middle of this spiral holder should be realised. This has the downside that it is impossible to visually check the probe coagulation location on the retina sample.

Another sensor orientation concept orientation as displayed in Figure 44 is explored, in which there are two vertical strips of NTC sensors. However, as the diathermy probe would be applied in the center of the two vertical strips, there is a change that both vertical sensor strips cannot measure temperature, because the heat will be transferred upward in between the sensor strips.

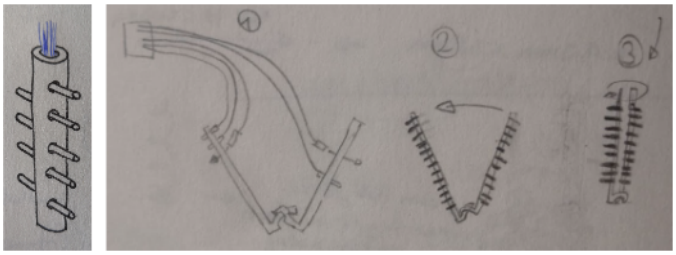

Fig. 44. Sensor holder concept with two vertical sensor strips

APPENDIX F
LABVIEW PROGRAM

The LabView program and its subcalculation diagram depicted in Figure 45 and Figure 46, respectively, are used for the acquisition of the sensor data (Van Driel, personal communication, December 6, 2021). This program ('Sensor_acquisition') can be downloaded via this link

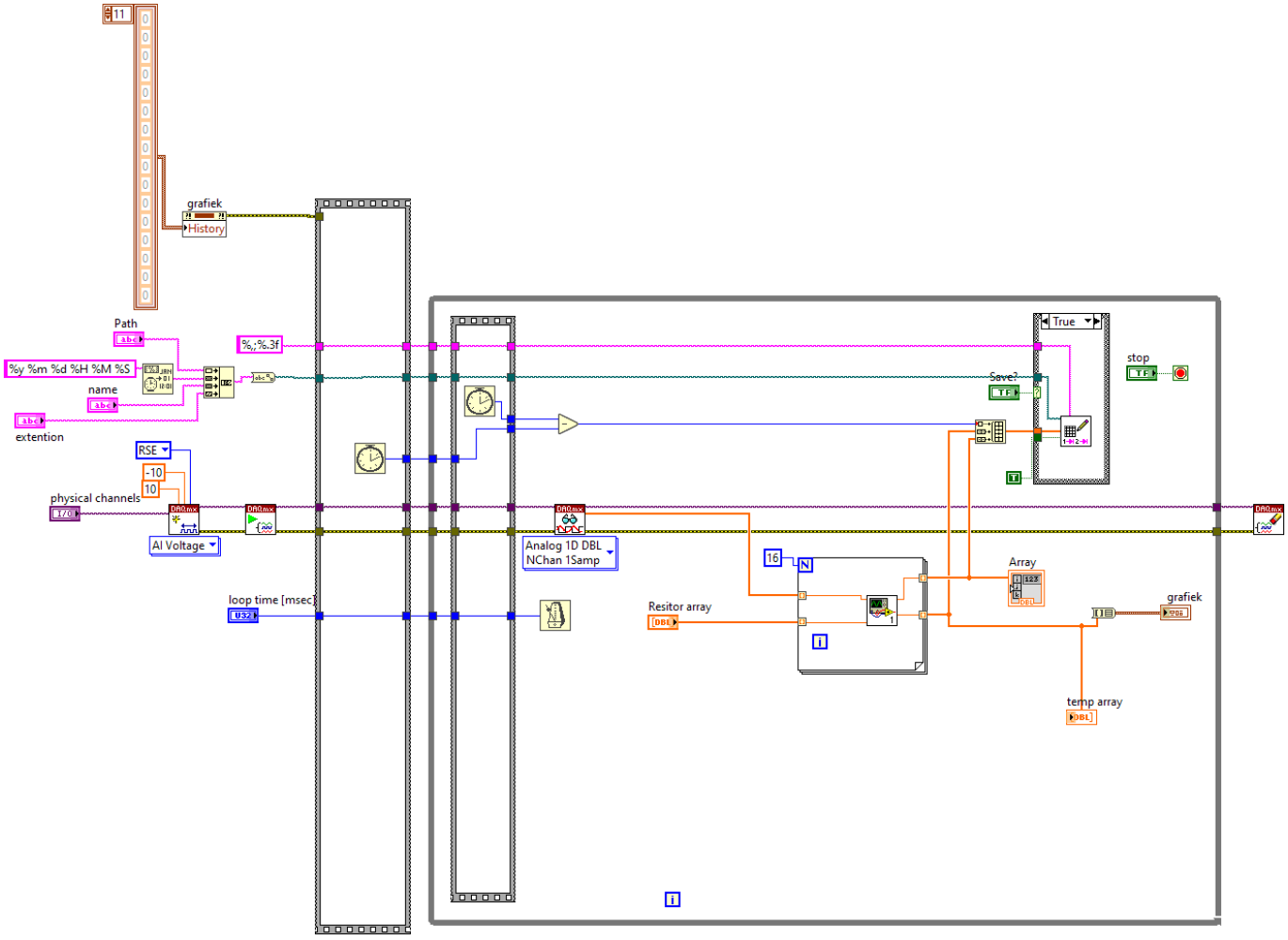

Fig. 45. LabView sensor module program

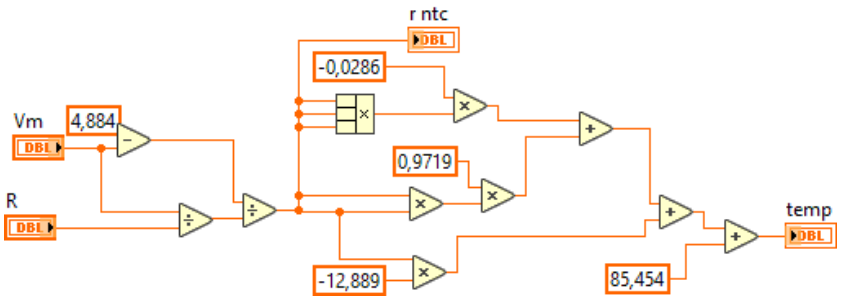

Fig. 46. LabView sub-calculation program

APPENDIX G
VALIDATION OF SENSOR WITH STIRRER EXPERIMENT

The temperature results of the test, which determine the accuracy of the multi-sensor, are shown in Table XXI. The temperature increases within the thermometer measurements and the relative temperature increases within the corresponding sensor, and the difference between these relative differences are shown in Table XXII. The Matlab script 'SensorValidation.m' which is used for these calculations, can be downloaded via this link.

TABLE XXI
TEMPERATURE OF EXTERNAL THERMOMETER, SENSOR 1 AND DIFFERENCE BETWEEN THESE MEASUREMENTS

Acquisition	**T_e [°C]**	**$\bar{x}$ ± SD T_s [°C]**	**Diff. [°C]**
1	30.20	30.35 ± 0.17	0.15
2	34.10	33.95 ± 0.44	0.15
3	39.80	39.64 ± 0.54	0.16
4	39.90	39.78 ± 0.57	0.12

TABLE XXII
TEMPERATURE INCREASES BETWEEN MEASUREMENTS

Range	**Δ T_e [°C]**	**Δ T_e [°C]**	**Diff. [°C]**
1 2	3.90	3.60	0.30
1 3	9.60	9.29	0.31
1 4	9.70	9.44	0.26
2 3	5.70	5.69	0.01
2 4	5.80	5.83	0.03
3 4	0.10	0.15	0.05

APPENDIX H
SAMPLE PREPARATION PILOT TESTS

We performed several pilot tests to test how we could separate retina and preserve it as a sample. Figure 47 shows images of these tests.

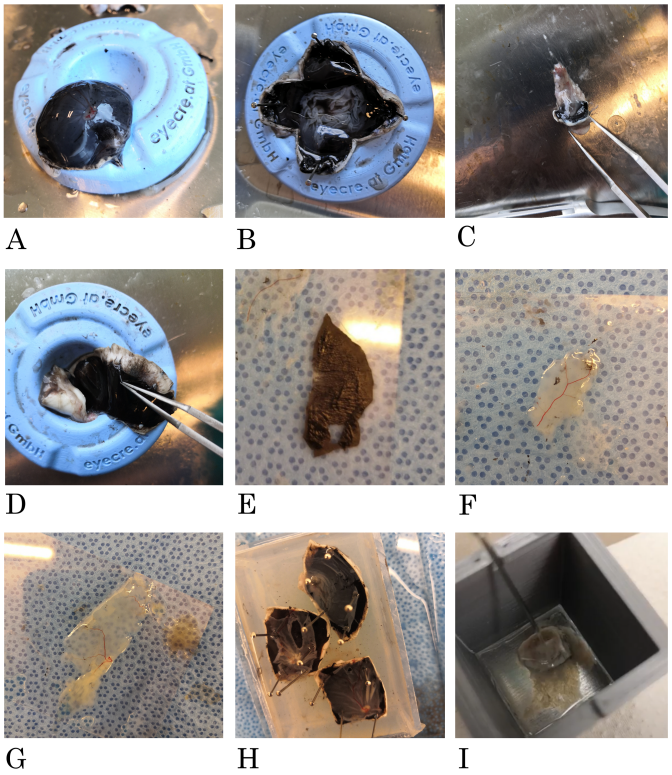

Fig. 47. Images of sample preparation pilot tests

The retina gets loose and damages easily. We tried to turn the sclera inside out, as shown in Figure 47A, so the retina lays on top of the convex shaped sclera. When turning the sclera back, cutting four incisions in the sclera and pinning it down, the retina seamed fully detached, as shown in Figure 47B. Complete removal of the retina, except from the fixed part to the optic nerve, succeeded by cutting out the nerve. However, as can be seen in Figure 47C, the retina is clinged together and cannot be separated in the open air.

The removal or the choroid, shown in Figure 47D, is difficult. During peeling the choroid can tear down and it folds inwards, so a water bath is needed to unfold it and let it slide on a glass while retracting the glass out of the water. A separated piece is shown in Figure 47E.

When cutting a piece of sclera containing retina tissue, a small piece of retina can be pulled of with a sponge and dragged on a glass substrate if it is loose and not too large (Figure 47F. This was difficult and it took a couple of times because parts of the retina broke off during the pulling.

When cutting another piece of sclera containing loose retina tissue, the retina gets loose and floats when putting the piece in water. Then it curls inwards, so two pairs of forcepses are needed to unfold it and let it slide on a glass while retracting the glass out of the water. Then also bigger parts can be put on the glass, as can be seen in Figure 47G.

When depositing water on loose retina on the glass, it directly flows away. Pieces of sclera containing retina are pinned on gelatin and water was deposited on top of these pieces. As can be seen in Figure 47H, the retina loosens at the pins and curls around the edges, and water flows beneath it.

The retina is fixed at optic nerve and loosely attached to the ora serrata and the vitreous humour is attached to the edge of the retina, so when you let the vitreous humour falls out, the attachment of the retina gets loose around the edges. Then, it is still fixed to the optic nerve.

When Decalin, a heavy-fluid, is deposited on a piece of separated retina is, which still is fixated to the optic nerve, the retina piece stays at places and does not curl or float. This is shown in Figure 47I.

APPENDIX I
DATA PROCESSING SCRIPT

The diagram shown in Figure 48 is a manual on how to use the Matlab script for the data processing of the experiment. This includes the thermography frame number identification, the thermography ROI determination and processing, the sensor reference numbers identification and processing, the missing thermography data identification, the sensor peak identification and the final analysis. The script 'DataProcessing.m' can be downloaded via this link.

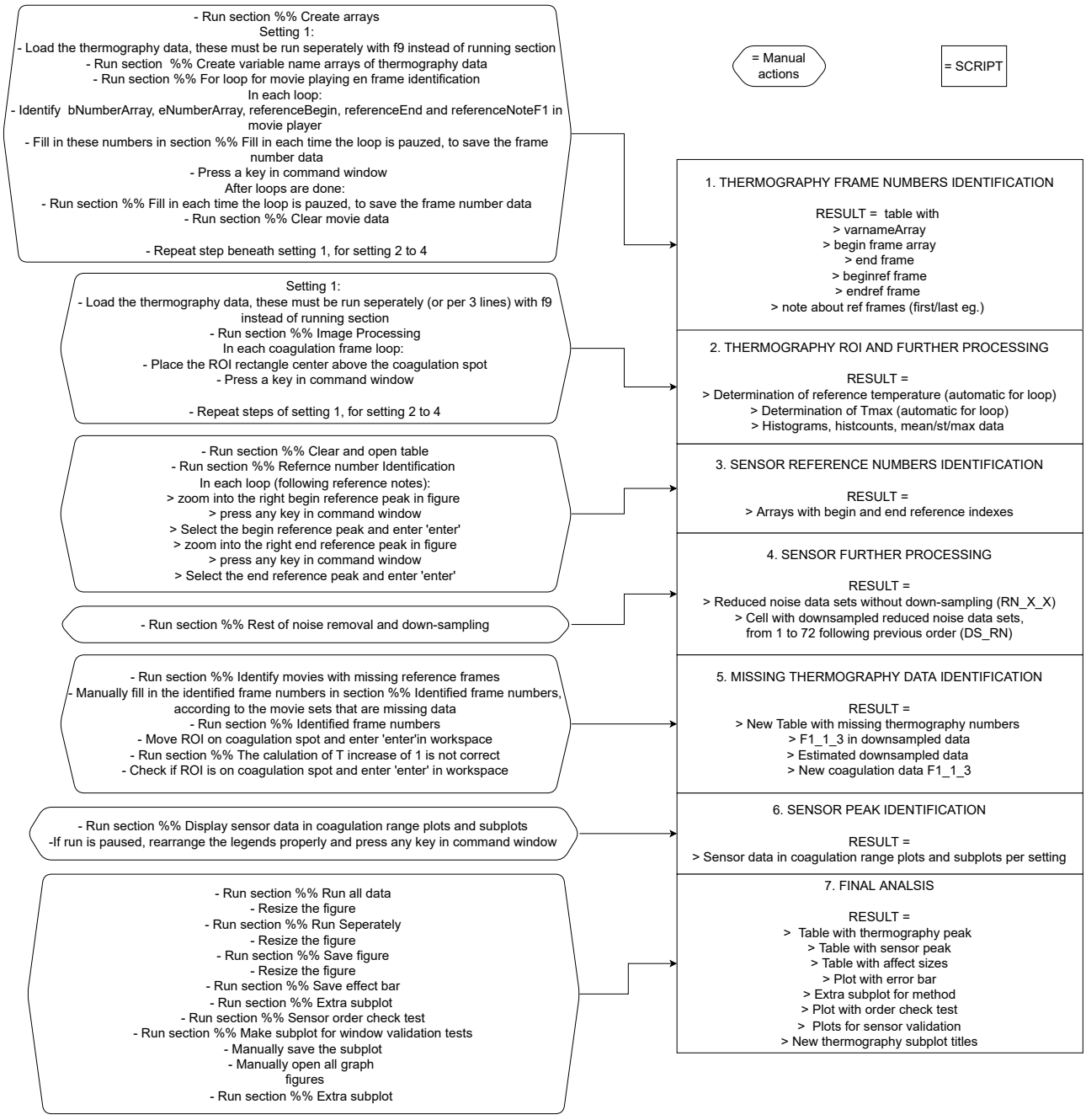

Fig. 48. Manual diagram for data processing Matlab script

APPENDIX J
VIDEO EXPORTATION FORMATS

With the Matlab Image Acquisition Toolbox, recorded videos can be exported as a Matlab file and in AVI file. The AVI file is saved during the acquisition and the Matlab file is saved afterwards.

The Matlab file is used to analyse the retrieved videos directly in Matlab. These Matlab files consists of a '4-D unint8' data format. The four dimensions of this data type contain the pixel width, the pixel height, the RGB color value of the pixel and the video frame, respectively. The RGB value of each pixel represents a temperature value, which can be calculated from the color bar on the image with corresponding minimum and maximum value.

The AVI file can be used to retrieve the starting and ending time of the acquisition. Additionally, if the Matlab file cannot be saved after acquisition, the AVI file can also be imported into Matlab, and individual frames can be manually exported from the movie player to unint8 data frames and still be used for analysis.

APPENDIX K
CONVERSION RGB TO TEMPERATURE ACCURACY

At the conversion of RGB images to temperature images, the intensities of the grayscale pixels are converted to values within the range of 0 to 380. However, the colors in the original color map on the grayscale image are not equally distributed. The temperature effect of this dissimilarity is determined by taking the intensity difference between these two color maps and multiplying the intensity difference by the maximum temperature difference in the image.

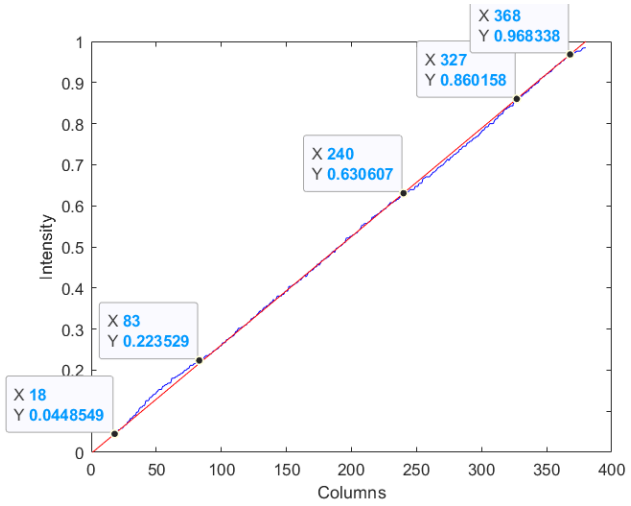

Fig. 49. Intensity values of the indexed map (red) and of the original color map on the grayscale image (blue)

The intensity values of the indexed map and of the original color map on the grayscale image are plotted in Figure 49. In the graph can be seen that there are different ranges. In the range of 83 to 240, the converted temperature would range from 28.25°C to 37.16°C. In the thesis experiment, there are three measurements which are below this range and there are three measurements which are above this range. Within this range, the temperature difference between the indexed map and the original color map on the grayscale image, the mean temperature difference is 0.05 ± 0.04°C and the maximum temperature difference is 0.18°C. Because most of the measurements are within this range, we can conclude that the temperature conversion has an accuracy of 0.05 ± 0.04°C.

The script 'ConversionValidation.m' provides the calculations of the accuracy and can be downloaded via this link.

APPENDIX L
FINAL FILTERS

For the reduction of noise, the following list of Matlab commands is applied to the raw data of each measurement in chronological order.

1) 'filloutliers', which detects outliers using movmedian moving method (which detects outliers "as elements more than three local scaled MAD from the local median over a window length" [53] of 200) and fills outliers "using linear interpolation of neighboring, non-outlier values" [53]
2) 'filloutliers', which detects outliers using movmedian moving method (which detects outliers "as elements more than three local scaled MAD from the local median over a window length" [53] of 80) and fills outliers "using linear interpolation of neighboring, non-outlier values" [53]
3) 'medfilt1', a one-dimensional third-order median filter [54]
4) 'lowpass', a low pass filter with a pass band of 0.000000001 Hz, applied on the data which has been acquired at a rate of 232.6 Hz (based on a frame rate of 23 frames per second) [55]
5) 'lowpass', a low pass filter with a pass band of 0.000000001 Hz, applied on the data which has been acquired at a rate of 232.6 Hz (based on a frame rate of 23 frames per second) [55]

APPENDIX M
GRADIENT SUBSET SELECTION

The gradients of the sensor peak measurements, which are above the criterion of 0.0010, are shown in Table XXIII. From these 52 measurements, the measurements at which no peak could be identified by visually checking the temperature peak graphs shown in Appendix Q), are excluded from the sensor analysis.

TABLE XXIII
GRADIENT VALUES AND RESULTS OF VISIBLE PEAK CHECK OF MEASUREMENTS WITH GRADIENT ABOVE 0.0010

Measurement	Gradient	Visible peak
C1_R1_M1	0.0012	Yes
C1_R1_M3	0.0011	Yes
C1_R1_M8	0.0012	No
C2_R1_M1	0.0073	Yes
C2_R1_M2	0.0035	Yes
C2_R1_M3	0.0018	Yes
C2_R1_M4	0.0028	Yes
C2_R1_M5	0.0040	Yes
C2_R1_M6	0.0019	Yes
C2_R1_M7	0.0052	Yes
C2_R1_M8	0.0049	Yes
C2_R1_M9	0.0022	Yes
C2_R1_M10	0.0029	Yes
C2_R2_M1	0.0025	Yes
C2_R2_M2	0.0077	Yes
C2_R2_M3	0.0037	Yes
C2_R2_M4	0.0036	Yes
C2_R2_M5	0.0019	Yes
C2_R2_M6	0.0058	Yes
C2_R2_M7	0.0022	Yes
C2_R2_M8	0.0036	Yes
C3_R1_M1	0.0012	No
C3_R1_M2	0.0024	Yes
C3_R1_M3	0.0011	No
C3_R1_M5	0.0013	No
C3_R1_M6	0.0011	No
C3_R1_M7	0.0031	Yes
C3_R1_M10	0.0021	Yes
C3_R2_M1	0.0011	Yes
C3_R2_M2	0.0014	Yes
C3_R2_M3	0.0014	Yes
C3_R2_M4	0.0011	Yes
C3_R2_M5	0.0014	No
C3_R2_M7	0.0011	No
C4_R1_M1	0.0048	Yes
C4_R1_M2	0.0039	Yes
C4_R1_M3	0.0060	Yes
C4_R1_M4	0.0094	Yes
C4_R1_M5	0.0012	Yes
C4_R1_M6	0.0036	Yes
C4_R1_M7	0.0088	Yes
C4_R1_M8	0.0010	Yes
C4_R1_M9	0.0044	Yes
C4_R1_M10	0.0055	Yes
C4_R2_M1	0.0026	Yes
C4_R2_M2	0.0083	Yes
C4_R2_M3	0.0048	Yes
C4_R2_M4	0.0115	Yes
C4_R2_M5	0.0209	Yes
C4_R2_M6	0.0028	Yes
C4_R2_M7	0.0049	Yes
C4_R2_M8	0.0028	Yes

APPENDIX N
EXCLUSION OF REPETITION C1_R1

It should be expected that the mean duration within the conditions is similar, also between repetitions, because the application time is used. As can be seen in Table XXIV, the effect size of -3.28 between the mean heating duration of Repetitions C1_R1 and C1_R2, is out of proportion compared to the effect sizes between the other repetitions with the same condition.

In Table XXV can be seen that there is a large effect size between the mean thermography temperature increase of repetition C1_R1 and C1_R2 there is a large difference in means. This is also out of proportion compared to the effect sizes between the other repetitions with the same condition.

The same trend is seen in the sensor measurements in Table XXVI. Here, the effect sizes between the other repetitions with the same condition are small, while the effect size between Repetitions C1_R1 and C1_R2 is large.

From the latter arguments, we can conclude that the indented condition (2.2J (2.2W * 1")) seems to not have been achieved.

TABLE XXIV
MEAN AND STANDARD DEVIATION OF HEATING DURATION (IN AMOUNT OF FRAMES) PER REPETITION

Mean duration	**SD duration**	**Mean duration**	**SD duration**	**Effect Size (Cohen's d)**
1_1		1_2		-3.28
37.30	5.95	60.12	7.40	
2_1		2_2		-0.06
62.20	9.84	62.75	7.23	
3_1		3_2		-0.34
55.50	7.12	57.62	4.14	
4_1		4_2		-0.82
78.30	13.33	89.71	12.98	

TABLE XXV
MEAN, STANDARD DEVIATION AND EFFECT SIZE OF THERMOGRAPHY DATA PER REPETITION

Thermography Mean T Increase [°C]	**Thermography SD T Increase**	**Thermography Mean T Increase [°C]**	**Thermography SD T Increase**	**Effect Size (Cohen's d)**
1_1		1_2		-4.42
1.52	0.63	5.09	0.92	
2_1		2_2		0.93
9.37	1.72	7.81	1.43	
3_1		3_2		-0.14
1.97	0.39	2.07	0.96	
4_1		4_2		0.49
6.49	1.43	5.54	2.33	

TABLE XXVI
MEAN, STANDARD DEVIATION AND EFFECT OF SENSOR DATA PER REPETITION

Sensor Mean T Increase [°C]	**Sensor SD T Increase**	**Sensor Mean T Increase [°C]**	**Sensor SD T Increase**	**Effect Size (Cohen's d)**
1_1		1_2		-2.39
0.04	0.03	0.16	0.07	
2_1		2_2		-0.20
0.19	0.04	0.20	0.05	
3_1		3_2		-0.03
0.08	0.05	0.09	0.02	
4_1		4_2		-0.35
0.24	0.09	0.28	0.15	

APPENDIX O
ALL THERMOGRAPHY AND SENSOR TEMPERATURE FINDINGS

Table XXVII includes all temperature findings of the included and excluded thermography and sensor measurements.

TABLE XXVII
ALL THERMOGRAPHY AND SENSOR TEMPERATURE FINDINGS

Measurement #	Energy [J]	Power [W]	Time ["]	Thermography Max. T [°C]	Thermography Ref. T [°C]	Thermography Incr. [°C]	Sensor Max. T [°C]	Sensor Ref. T [°C]	Sensor T Incr. [°C]
C1_1_1	2.2	2.2	1	28.31	27.58	0.73	25.31	25.24	0.08
C1_1_2	2.2	2.2	1	28.45	27.44	1.01	25.37	25.35	0.01
C1_1_3	2.2	2.2	1	29.10	27.86	1.23	25.67	25.58	0.08
C1_1_4	2.2	2.2	1	28.74	27.52	1.22	25.78	25.75	0.03
C1_1_5	2.2	2.2	1	28.75	27.82	0.92	25.74	25.73	0.01
C1_1_6	2.2	2.2	1	29.10	27.80	1.30	25.83	25.76	0.07
C1_1_7	2.2	2.2	1	30.02	27.59	2.43	26.03	26.01	0.02
C1_1_8	2.2	2.2	1	29.57	27.76	1.81	25.90	25.89	0.02
C1_1_9	2.2	2.2	1	29.95	27.74	2.21	25.81	25.78	0.03
C1_1_10	2.2	2.2	1	30.10	27.76	2.34	25.81	25.77	0.04
C1_2_1	2.2	2.2	1	31.08	26.75	4.32	25.98	25.81	0.18
C1_2_2	2.2	2.2	1	30.33	26.76	3.57	25.84	25.74	0.10
C1_2_3	2.2	2.2	1	32.28	27.12	5.15	25.91	25.69	0.22
C1_2_4	2.2	2.2	1	32.35	26.76	5.59	25.94	25.71	0.23
C1_2_5	2.2	2.2	1	30.94	26.64	4.30	25.52	25.47	0.04
C1_2_6	2.2	2.2	1	32.82	26.82	6.00	25.56	25.41	0.15
C1_2_7	2.2	2.2	1	32.93	26.92	6.01	25.56	25.35	0.21
C1_2_8	2.2	2.2	1	32.78	26.98	5.80	25.52	25.38	0.14
C2_1_1	4	4	1	32.65	25.81	6.84	24.96	24.75	0.21
C2_1_2	4	4	1	36.26	25.76	10.50	25.11	24.88	0.22
C2_1_3	4	4	1	34.12	25.60	8.52	25.10	24.97	0.13
C2_1_4	4	4	1	33.35	25.97	7.38	25.21	25.04	0.17
C2_1_5	4	4	1	34.29	25.83	8.47	25.31	25.10	0.21
C2_1_6	4	4	1	36.37	26.34	10.03	25.29	25.16	0.12
C2_1_7	4	4	1	39.41	26.82	12.59	25.45	25.21	0.24
C2_1_8	4	4	1	35.97	26.62	9.34	25.43	25.23	0.20
C2_1_9	4	4	1	37.59	26.63	10.96	25.38	25.23	0.15
C2_1_10	4	4	1	36.25	27.22	9.03	25.47	25.28	0.19
C2_2_1	4	4	1	31.08	26.35	4.73	25.13	25.00	0.13
C2_2_2	4	4	1	35.16	26.81	8.34	25.23	25.01	0.22
C2_2_3	4	4	1	33.99	26.42	7.57	25.27	25.09	0.18
C2_2_4	4	4	1	35.73	26.43	9.30	25.37	25.13	0.24
C2_2_5	4	4	1	34.17	26.67	7.49	25.29	25.14	0.16
C2_2_6	4	4	1	34.67	27.17	7.50	25.43	25.15	0.28
C2_2_7	4	4	1	35.38	26.92	8.46	25.35	25.17	0.18
C2_2_8	4	4	1	36.37	27.30	9.07	25.41	25.23	0.18
C3_1_1	2.2	1.1	2	29.18	27.19	2.00	26.19	26.13	0.06
C3_1_2	2.2	1.1	2	29.34	27.25	2.08	26.19	26.08	0.11
C3_1_3	2.2	1.1	2	29.43	27.35	2.08	26.10	26.05	0.04
C3_1_4	2.2	1.1	2	28.08	26.69	1.39	25.80	25.79	0.01
C3_1_5	2.2	1.1	2	29.16	27.35	1.81	25.79	25.71	0.08
C3_1_6	2.2	1.1	2	29.32	27.44	1.88	25.87	25.77	0.10
C3_1_7	2.2	1.1	2	29.56	27.58	1.97	25.97	25.79	0.17
C3_1_8	2.2	1.1	2	28.74	27.03	1.71	25.60	25.57	0.03
C3_1_9	2.2	1.1	2	29.17	27.34	1.83	25.59	25.52	0.07
C3_1_10	2.2	1.1	2	30.55	27.62	2.93	25.70	25.54	0.16
C3_2_1	2.2	1.1	2	30.57	28.42	2.15	26.14	26.07	0.08
C3_2_2	2.2	1.1	2	30.76	28.34	2.41	26.14	26.05	0.09
C3_2_3	2.2	1.1	2	31.28	28.34	2.94	26.10	25.99	0.10
C3_2_4	2.2	1.1	2	31.89	28.11	3.78	26.03	25.97	0.06
C3_2_5	2.2	1.1	2	27.43	26.58	0.85	25.63	25.50	0.13
C3_2_6	2.2	1.1	2	28.65	26.91	1.74	25.64	25.57	0.07
C3_2_7	2.2	1.1	2	28.26	26.87	1.39	25.62	25.56	0.07
C3_2_8	2.2	1.1	2	28.14	26.85	1.28	25.61	25.53	0.09
C4_1_1	4	2	2	32.60	27.27	5.33	26.42	26.22	0.19
C4_1_2	4	2	2	33.59	27.43	6.16	26.28	26.08	0.21
C4_1_3	4	2	2	33.83	27.52	6.31	26.18	25.96	0.22
C4_1_4	4	2	2	33.83	28.08	5.75	26.20	25.90	0.30
C4_1_5	4	2	2	32.70	27.65	5.06	25.82	25.72	0.09
C4_1_6	4	2	2	35.95	27.53	8.42	25.91	25.67	0.24
C4_1_7	4	2	2	33.88	27.82	6.07	26.02	25.63	0.39
C4_1_8	4	2	2	33.20	27.52	5.69	25.64	25.51	0.13
C4_1_9	4	2	2	34.28	27.74	6.54	25.74	25.45	0.29
C4_1_10	4	2	2	37.39	27.78	9.60	25.78	25.48	0.30
C4_2_1	4	2	2	30.14	27.01	3.13	25.98	25.83	0.15
C4_2_2	4	2	2	31.28	26.85	4.43	26.08	25.78	0.30
C4_2_3	4	2	2	32.65	26.61	6.04	26.02	25.76	0.27
C4_2_4	4	2	2	37.14	26.91	10.23	26.09	25.68	0.41
C4_2_5	4	2	2	0.00	0.00	0.00	26.61	26.04	0.57
C4_2_6	4	2	2	32.53	27.62	4.92	26.21	26.04	0.17
C4_2_7	4	2	2	30.79	26.84	3.95	26.20	25.98	0.22
C4_2_8	4	2	2	32.58	26.49	6.08	26.10	25.96	0.14

APPENDIX P
ALL THERMOGRAPHY TEMPERATURE FRAMES

In this appendix, the visual results of the thermography measurements are shown. These include the placement of the ROI around the first heating point, the first heating temperature image, the first heating temperature image within the ROI, the maximum temperature image within the ROI, the temperature increase image of the first heating frame within the ROI and the temperature increase image within the ROI of the frame containing the maximum temperature. Furthermore, a histogram (and a zoomed in version of the same histogram) is included which shows the amount of pixels containing the temperature ranges (on the horizontal axis). These figures are created using the script 'DataProcessing.m', which can be downloaded via this link.

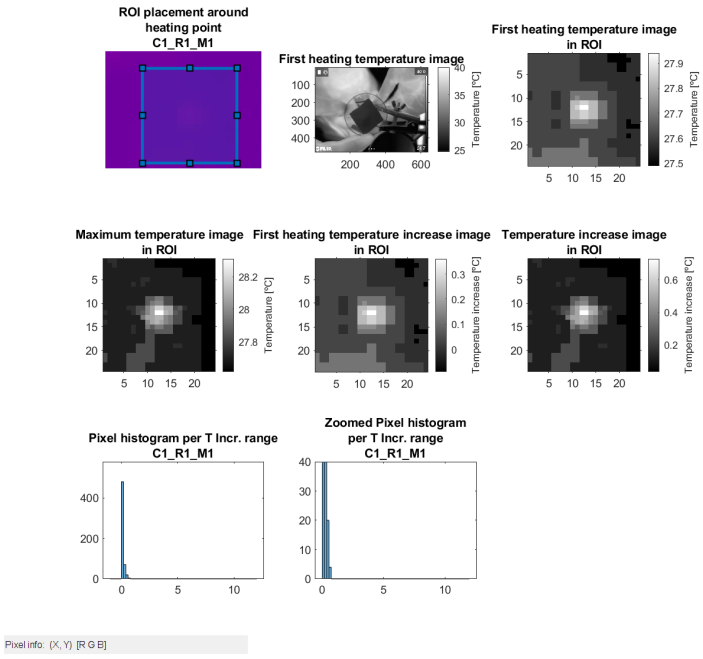

Fig. 50. Thermography images and histograms of Measurement C1_R1_M1

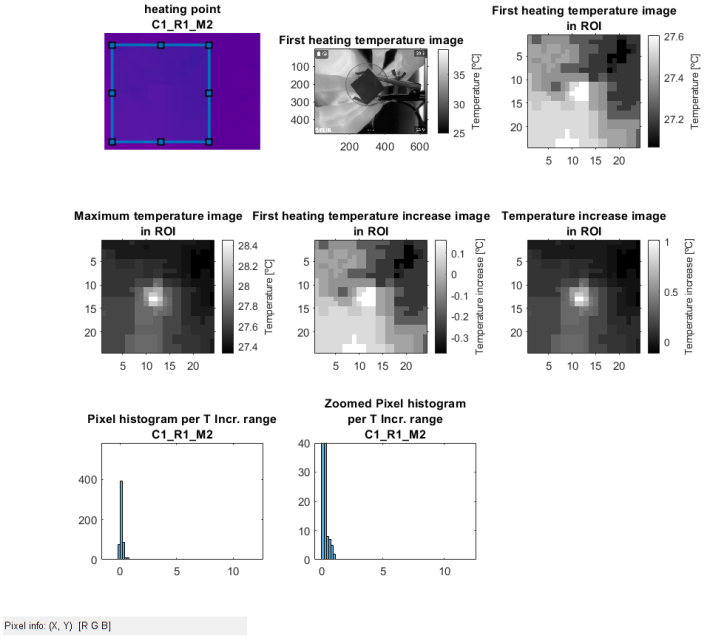

Fig. 51. Thermography images and histograms of Measurement C1_R1_M2

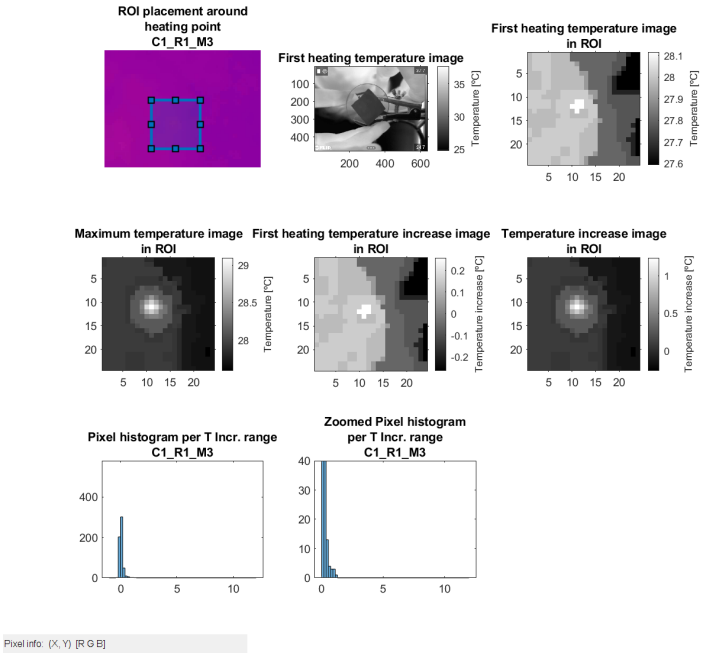

Fig. 52. Thermography images and histograms of Measurement C1_R1_M3

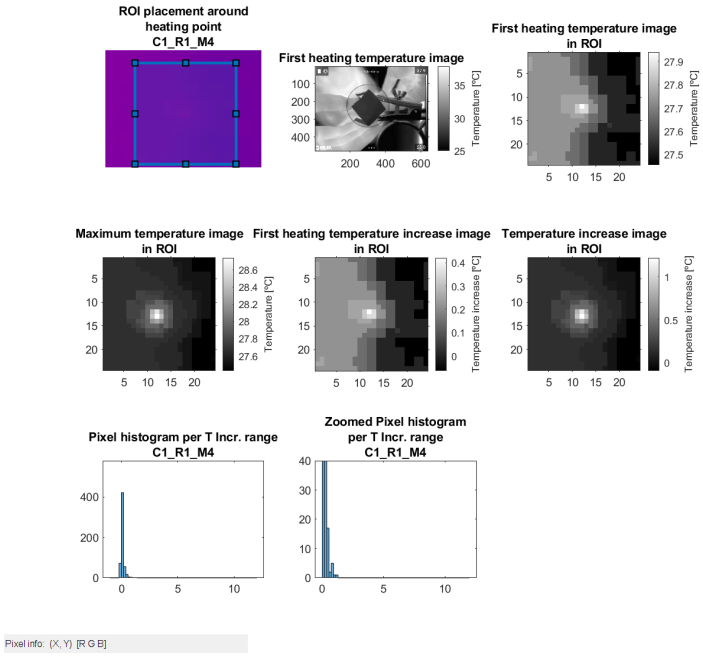

Fig. 53. Thermography images and histograms of Measurement C1_R1_M4

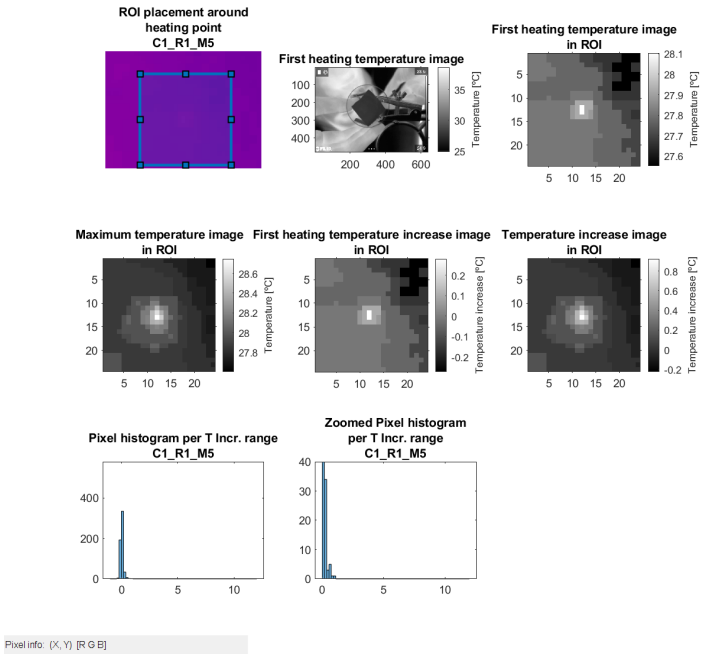

Fig. 54. Thermography images and histograms of Measurement C1_R1_M5

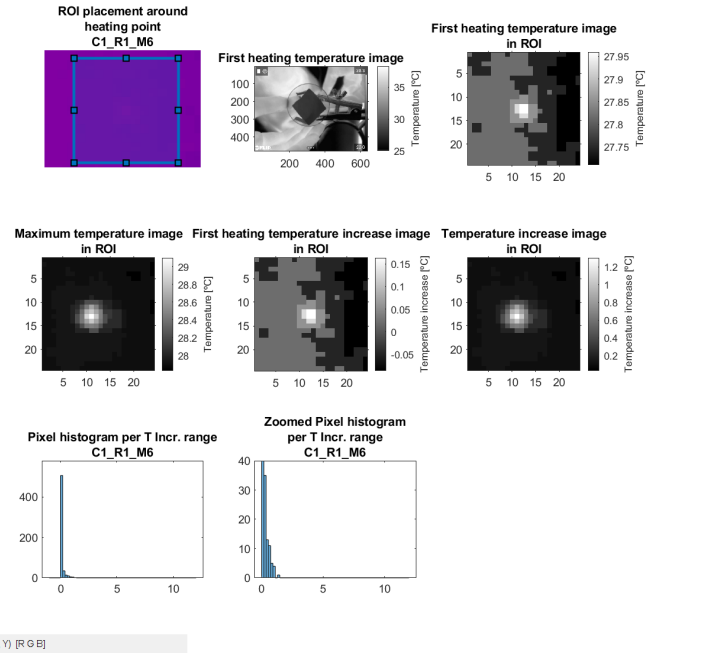

Fig. 55. Thermography images and histograms of Measurement C1_R1_M6

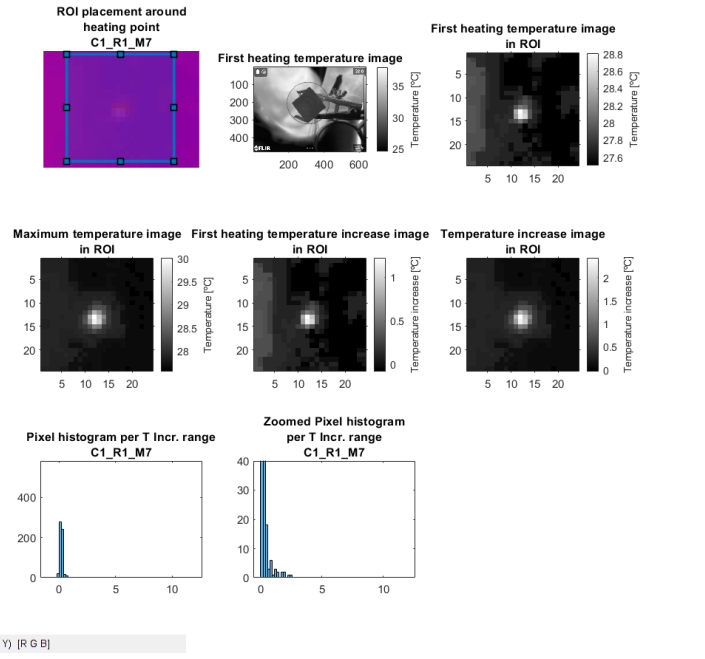

Fig. 56. Thermography images and histograms of Measurement C1_R1_M7

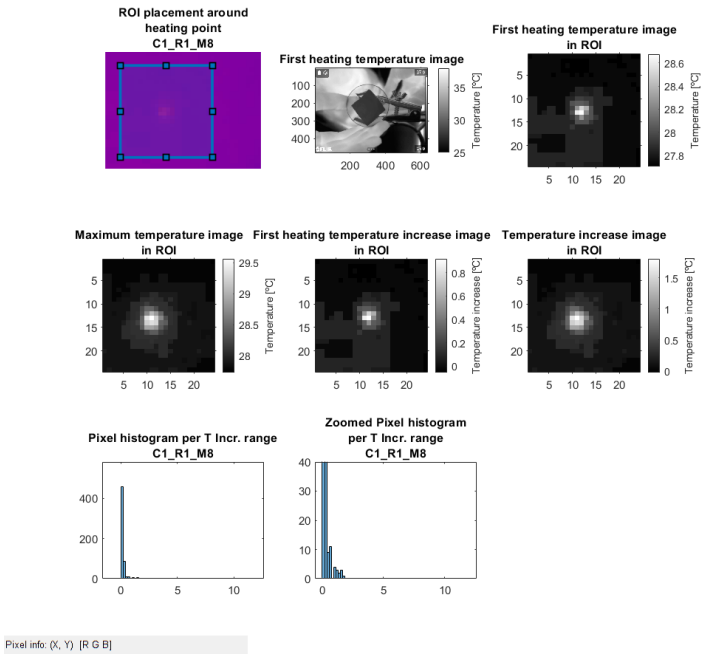

Fig. 57. Thermography images and histograms of Measurement C1_R1_M8

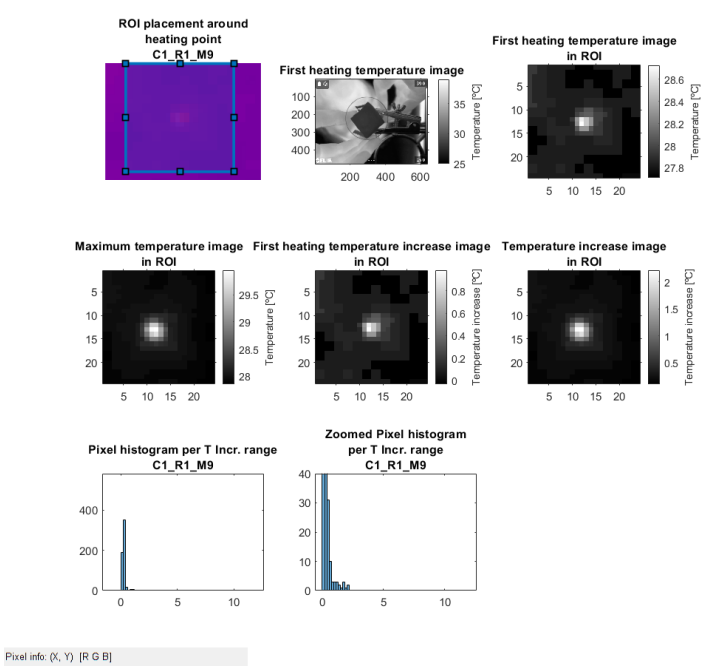

Fig. 58. Thermography images and histograms of Measurement C1_R1_M9

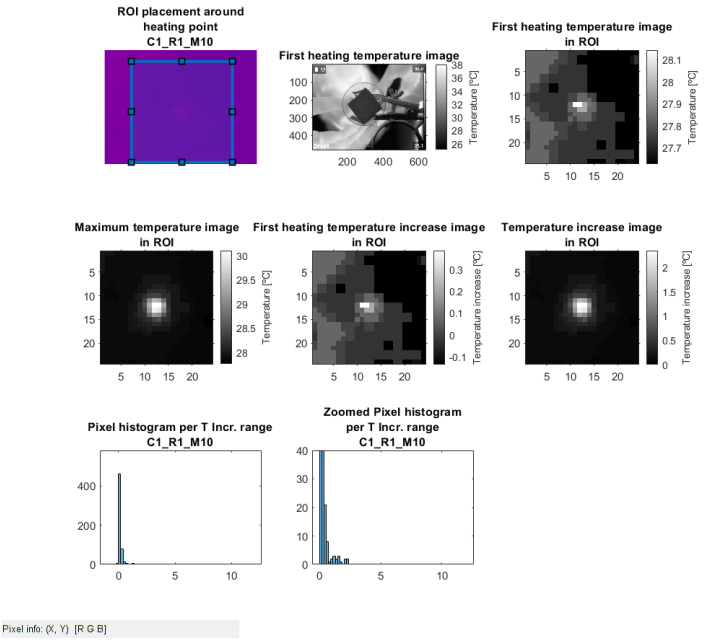

Fig. 59. Thermography images and histograms of Measurement C1_R1_M10

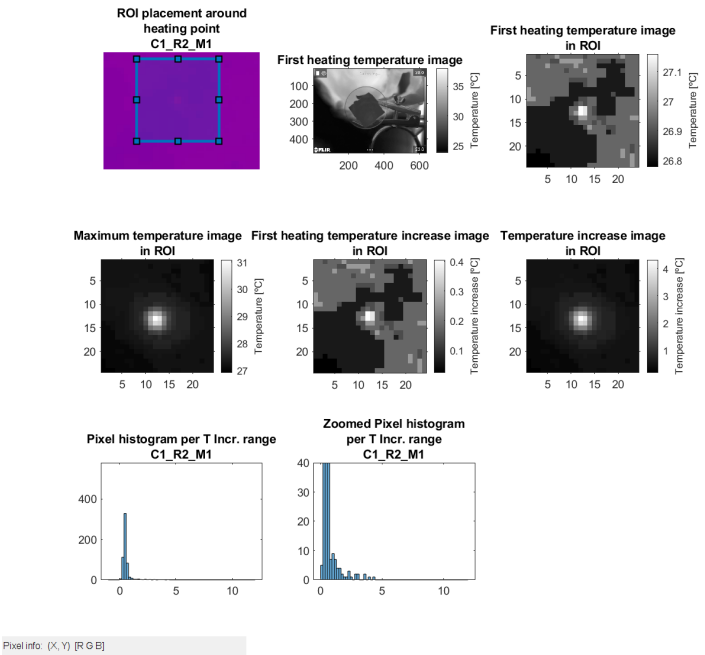

Fig. 60. Thermography images and histograms of Measurement C1_R2_M1

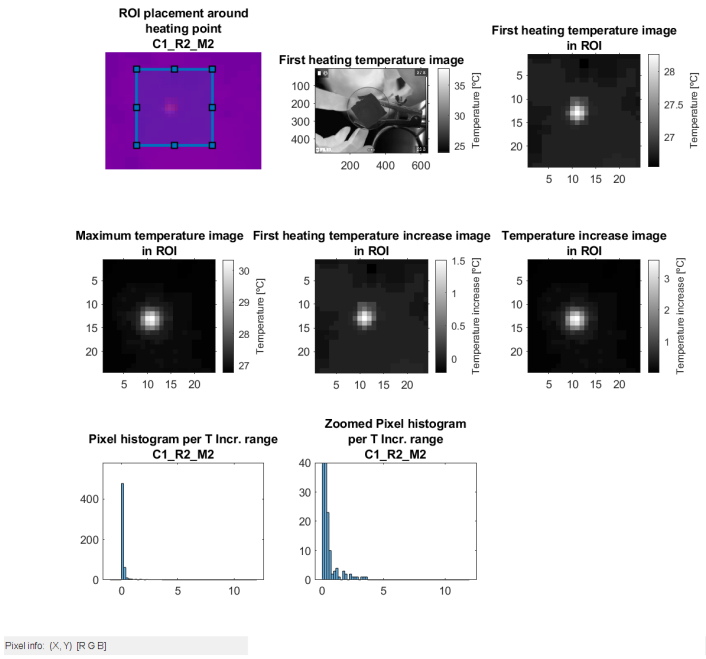

Fig. 61. Thermography images and histograms of Measurement C1_R2_M2

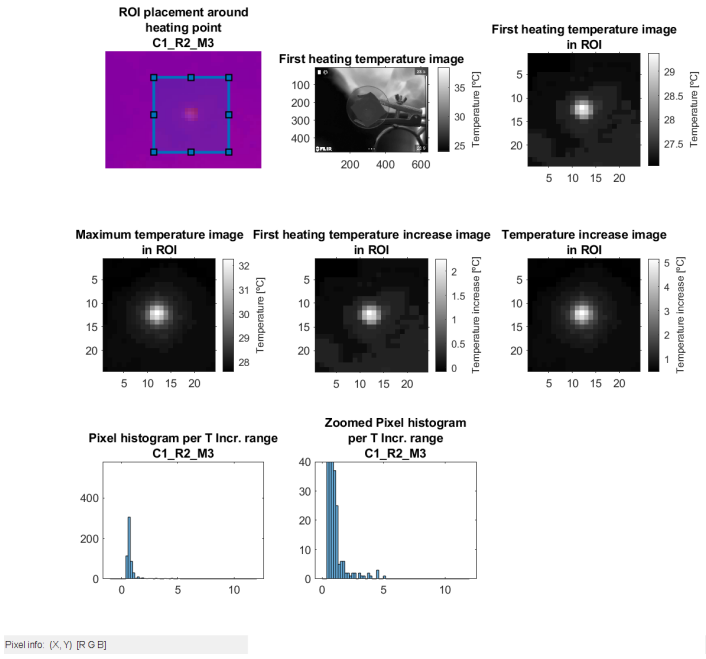

Fig. 62. Thermography images and histograms of Measurement C1_R2_M3

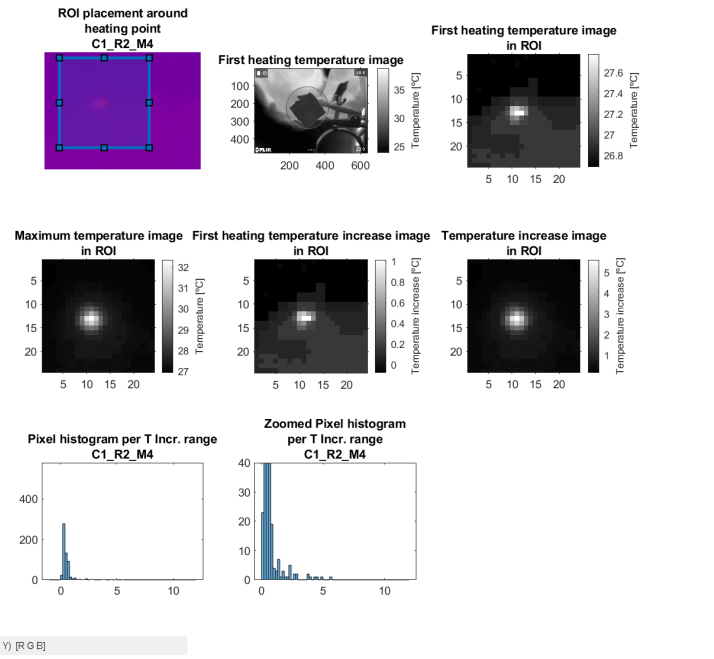

Fig. 63. Thermography images and histograms of Measurement C1_R2_M4

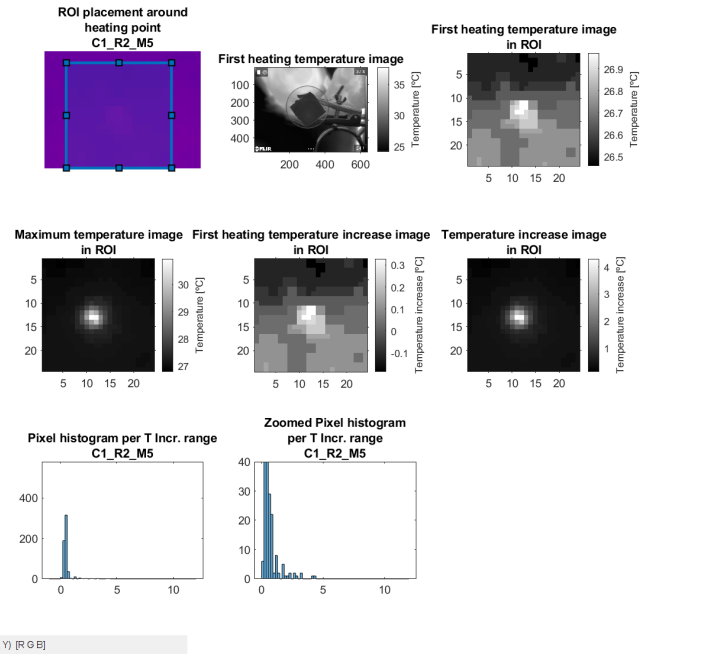

Fig. 64. Thermography images and histograms of Measurement C1_R2_M5

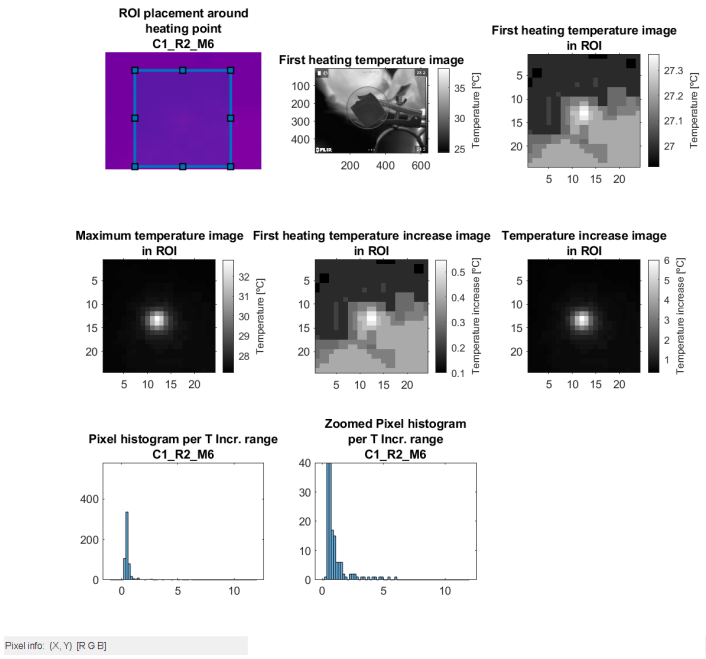

Fig. 65. Thermography images and histograms of Measurement C1_R2_M6

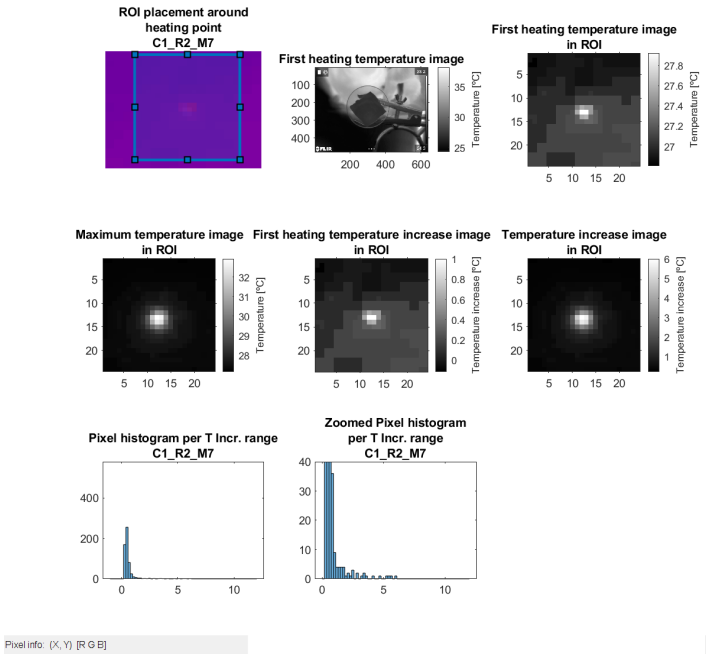

Fig. 66. Thermography images and histograms of Measurement C1_R2_M7

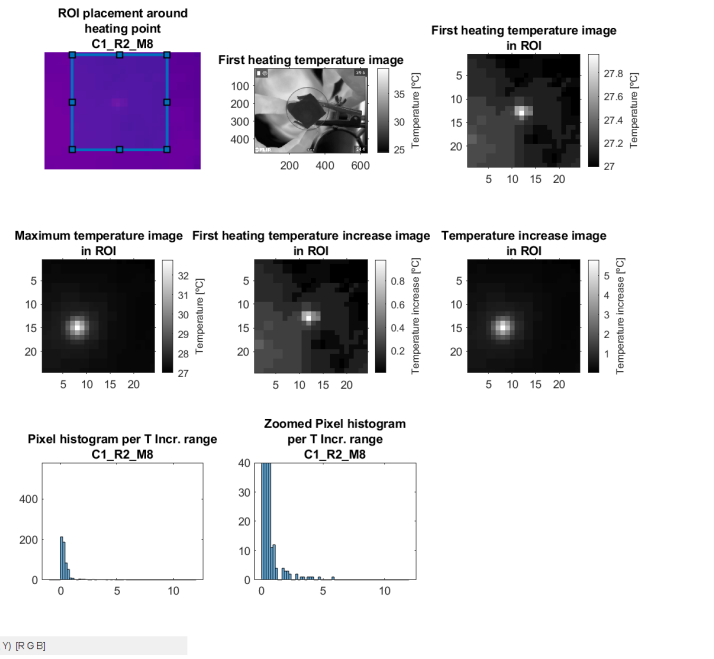

Fig. 67. Thermography images and histograms of Measurement C1_R2_M8

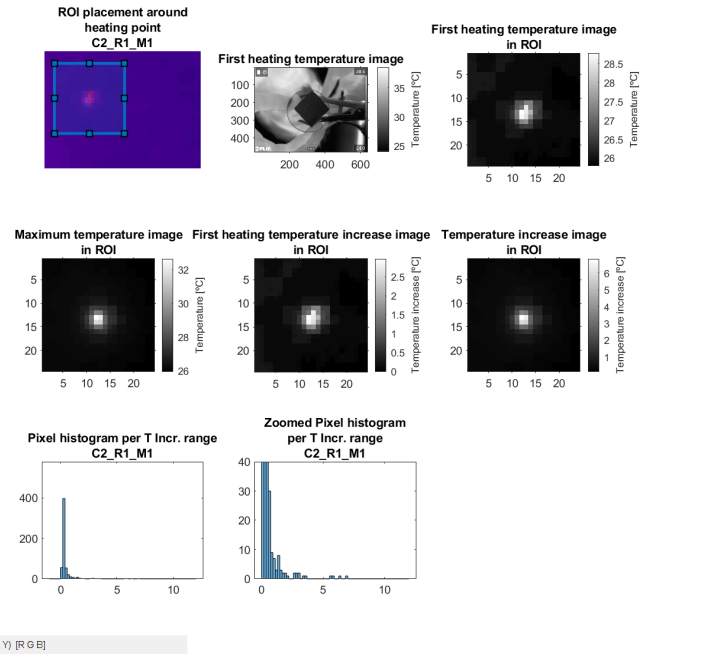

Fig. 68. Thermography images and histograms of Measurement C2_R1_M1

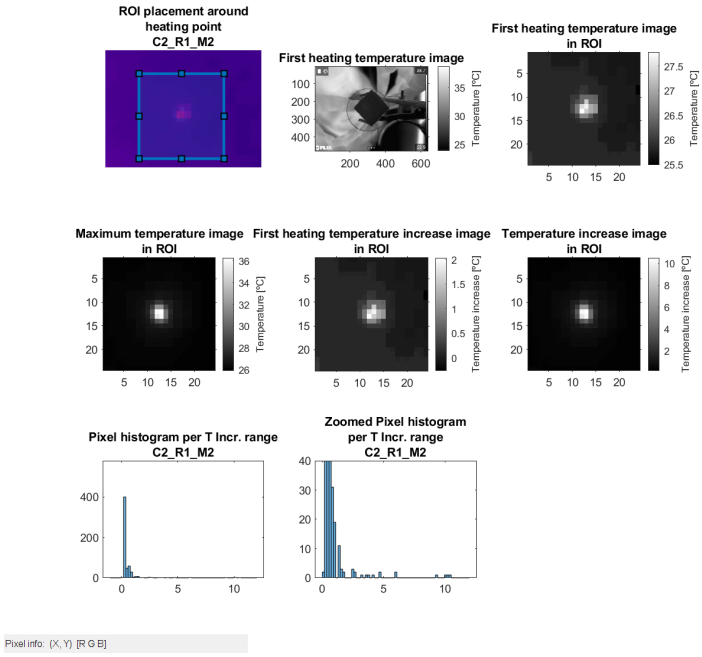

Fig. 69. Thermography images and histograms of Measurement C2_R1_M2

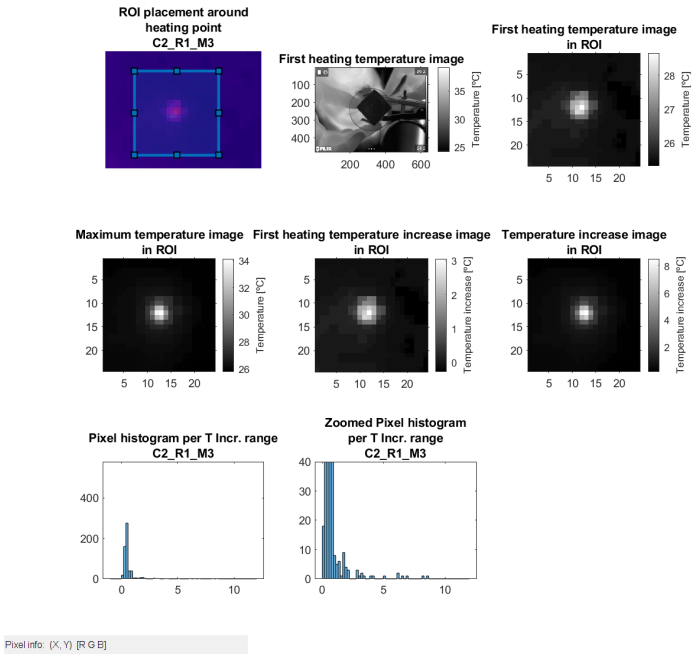

Fig. 70. Thermography images and histograms of Measurement C2_R1_M3

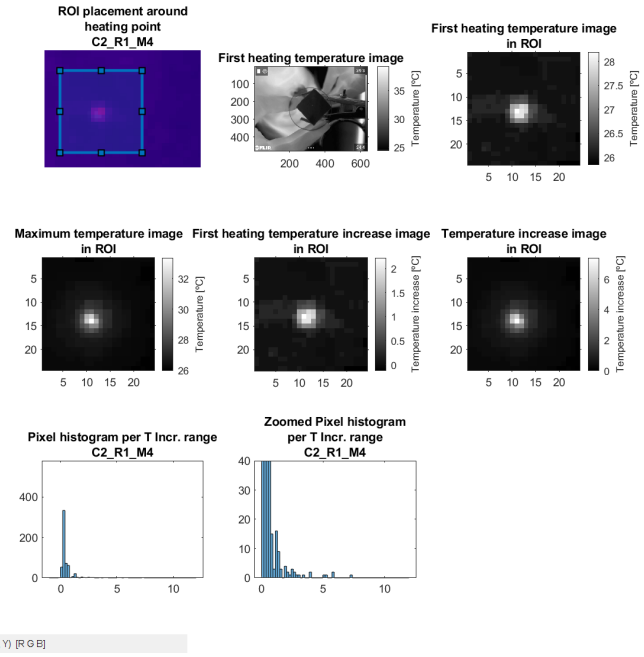

Fig. 71. Thermography images and histograms of Measurement C2_R1_M4

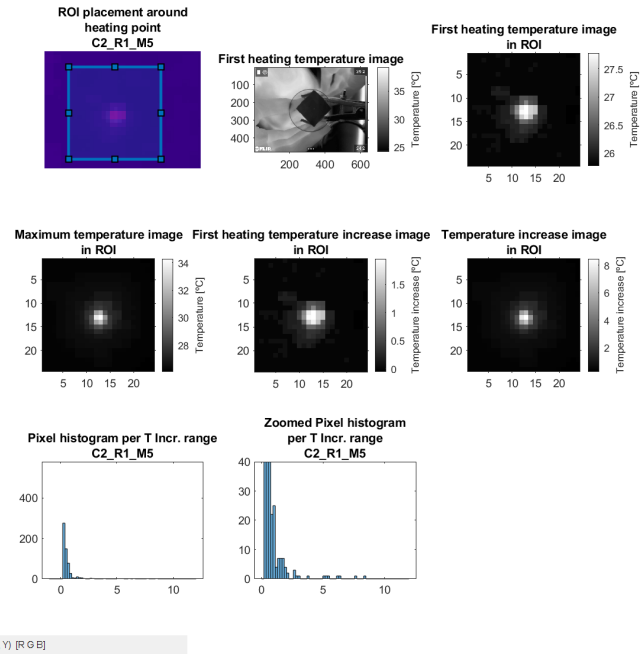

Fig. 72. Thermography images and histograms of Measurement C2_R1_M5

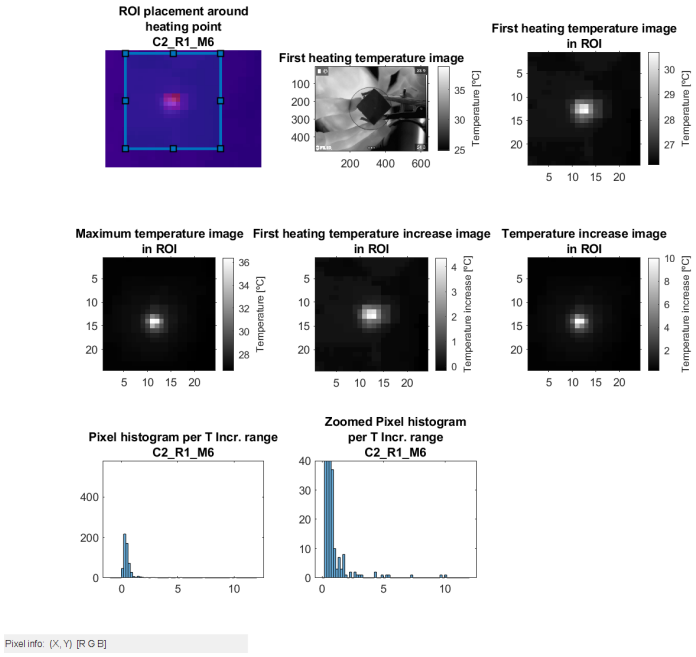

Fig. 73. Thermography images and histograms of Measurement C2_R1_M6

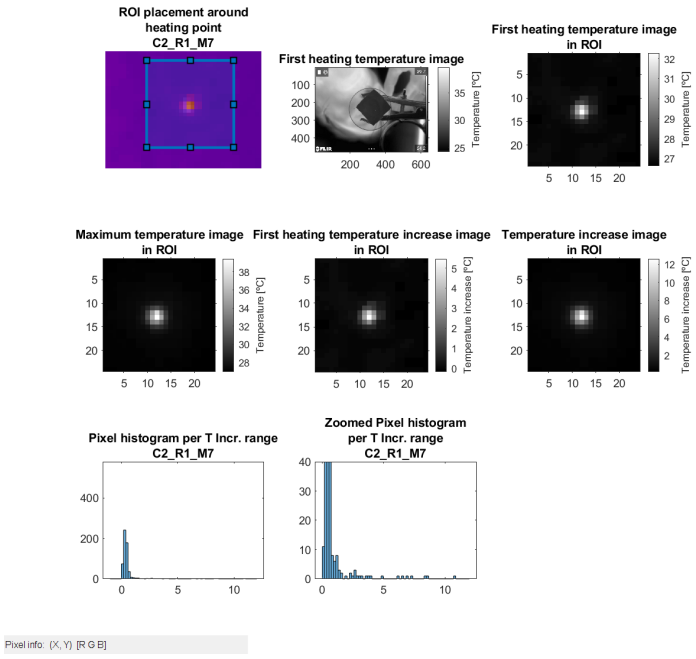

Fig. 74. Thermography images and histograms of Measurement C2_R1_M7

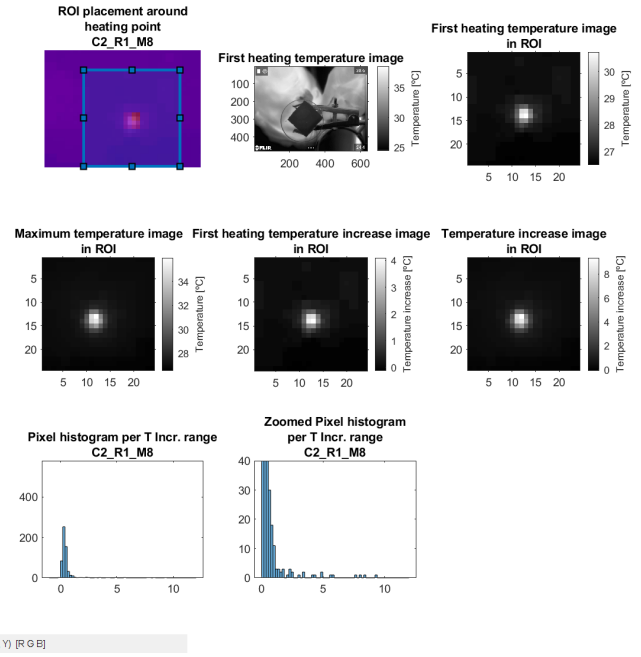

Fig. 75. Thermography images and histograms of Measurement C2_R1_M8

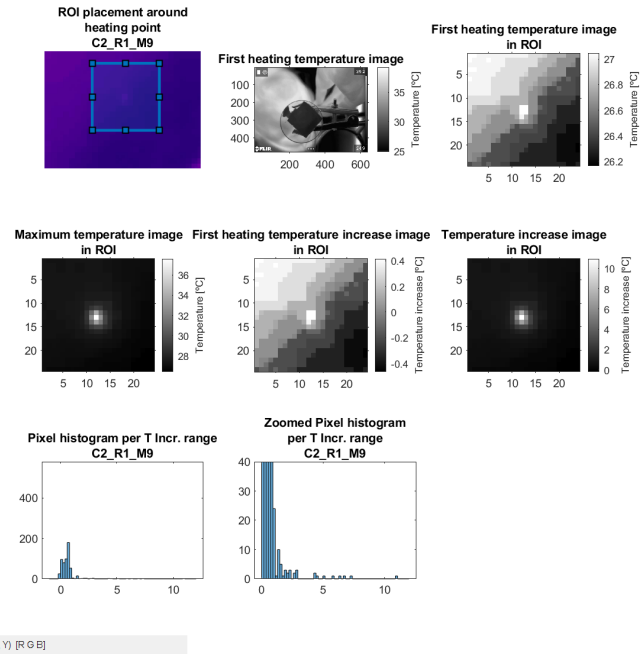

Fig. 76. Thermography images and histograms of Measurement C2_R1_M9

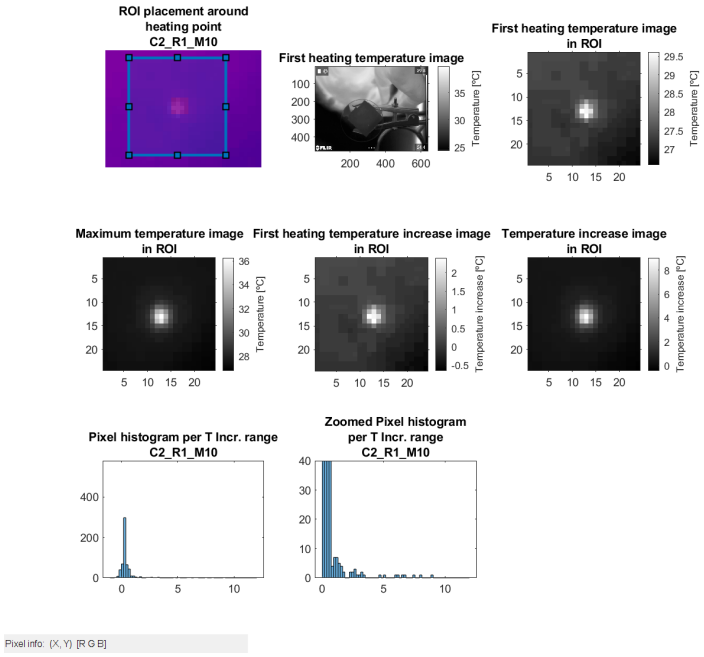

Fig. 77. Thermography images and histograms of Measurement C2_R1_M10

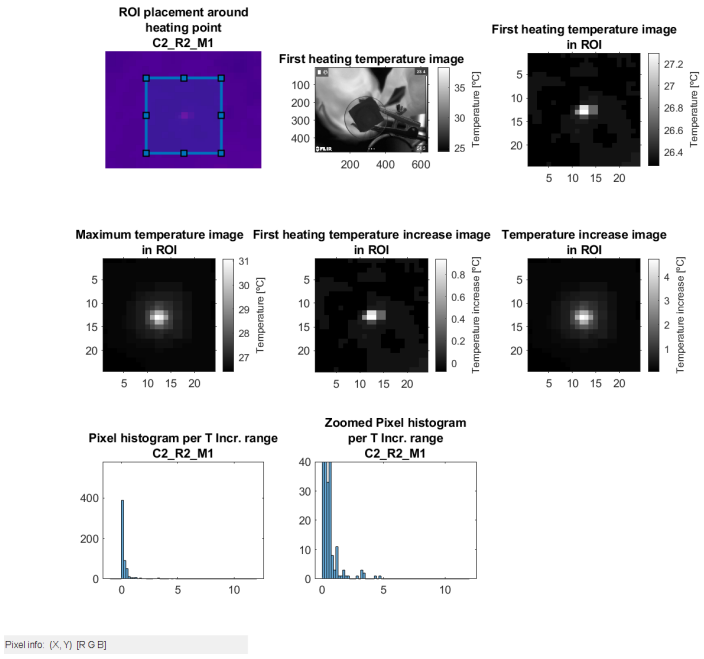

Fig. 78. Thermography images and histograms of Measurement C2_R2_M1

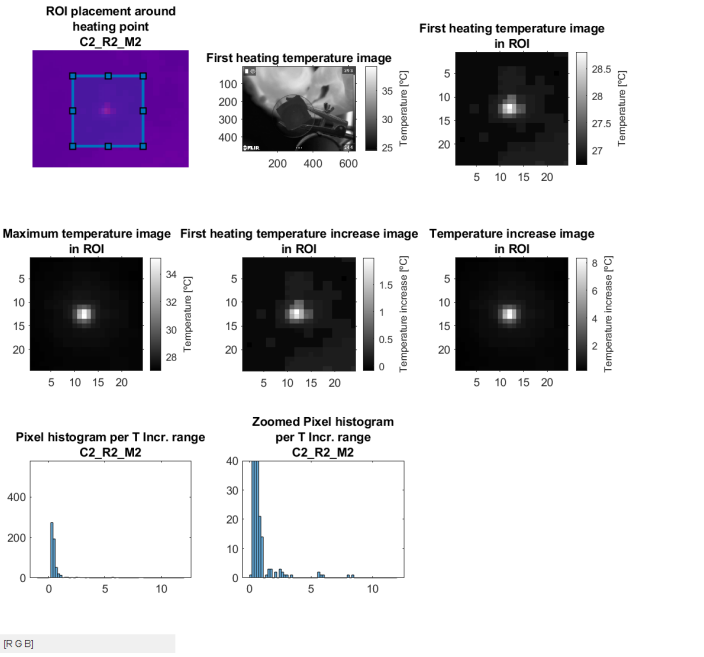

Fig. 79. Thermography images and histograms of Measurement C2_R2_M2

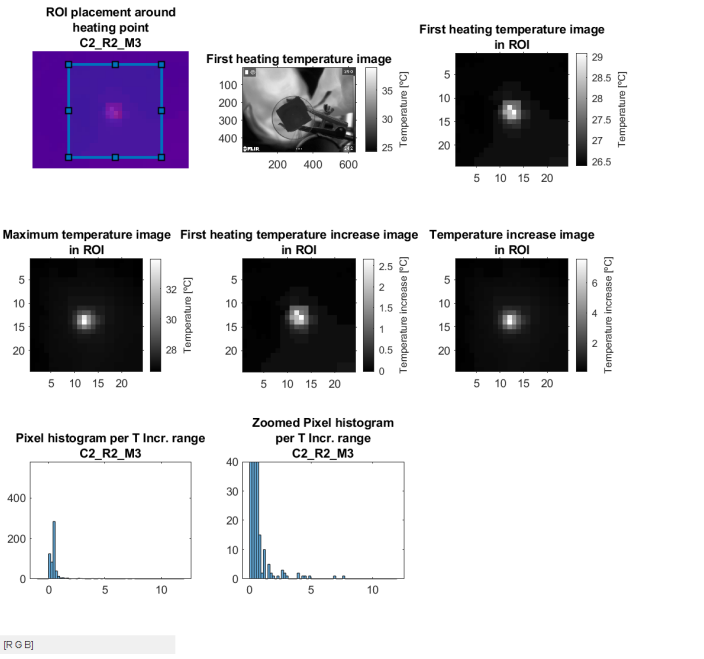

Fig. 80. Thermography images and histograms of Measurement C2_R2_M3

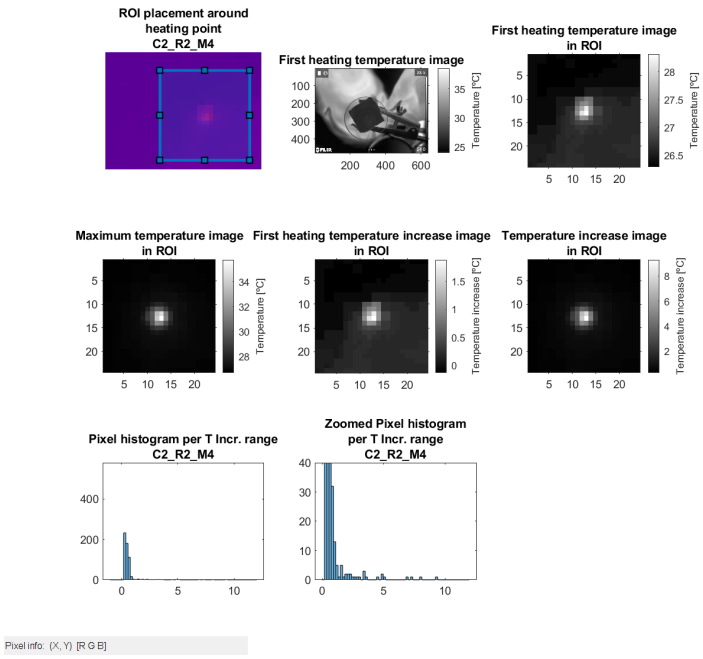

Fig. 81. Thermography images and histograms of Measurement C2_R2_M4

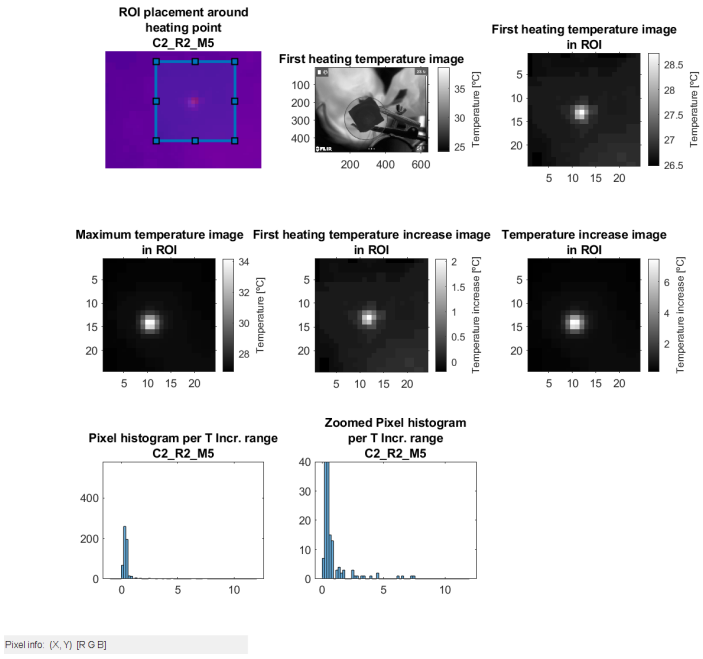

Fig. 82. Thermography images and histograms of Measurement C2_R2_M5

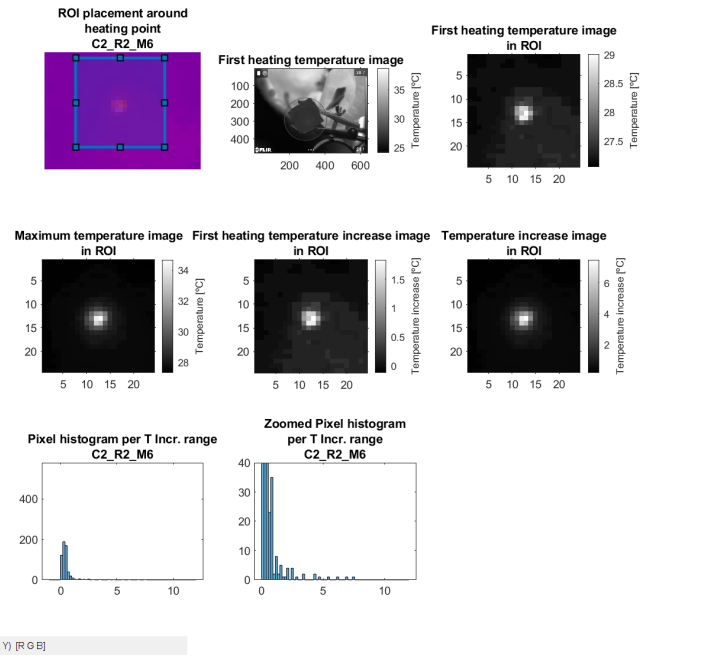

Fig. 83. Thermography images and histograms of Measurement C2_R2_M6

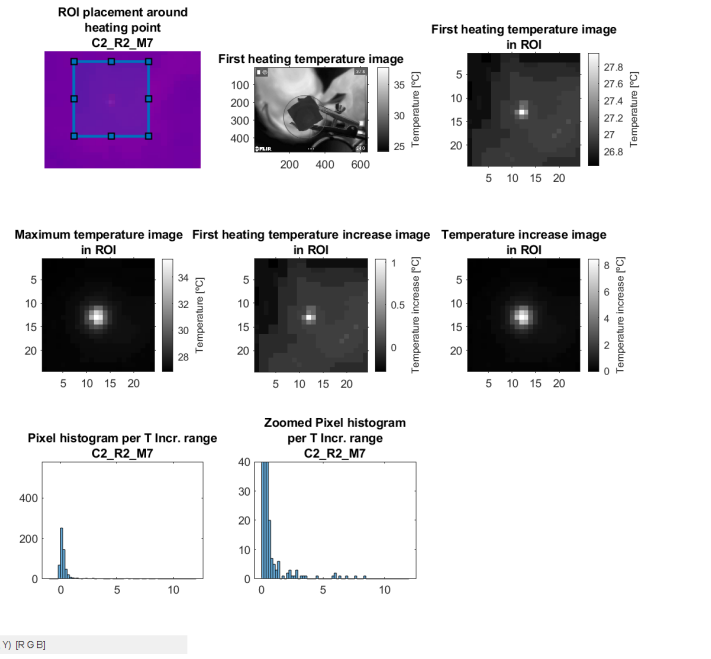

Fig. 84. Thermography images and histograms of Measurement C2_R2_M7

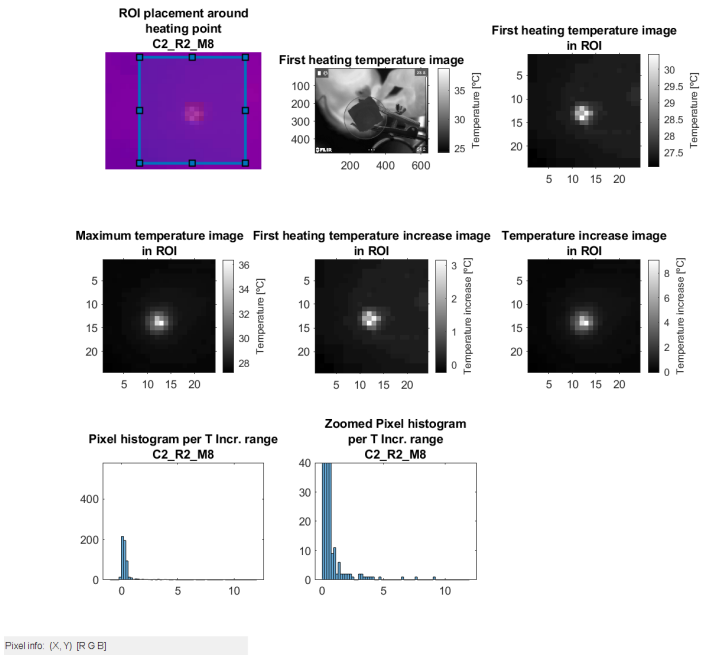

Fig. 85. Thermography images and histograms of Measurement C2_R2_M8

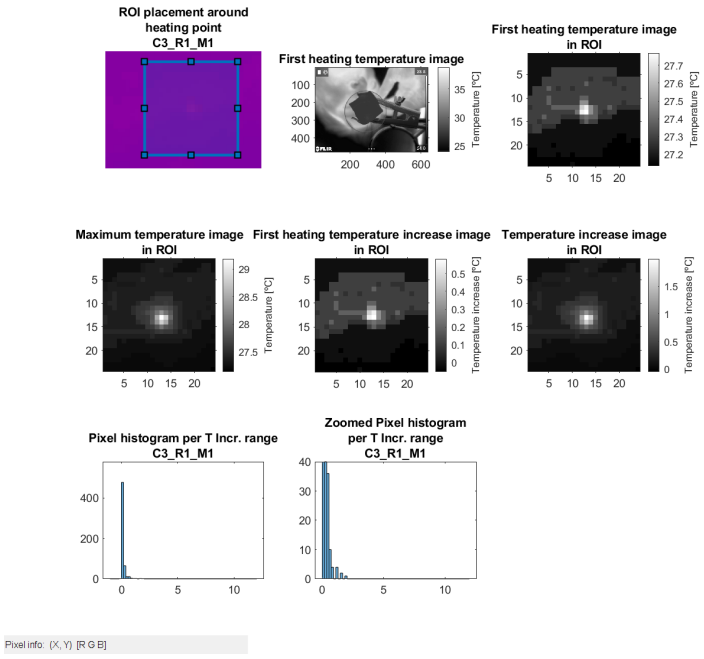

Fig. 86. Thermography images and histograms of Measurement C3_R1_M1

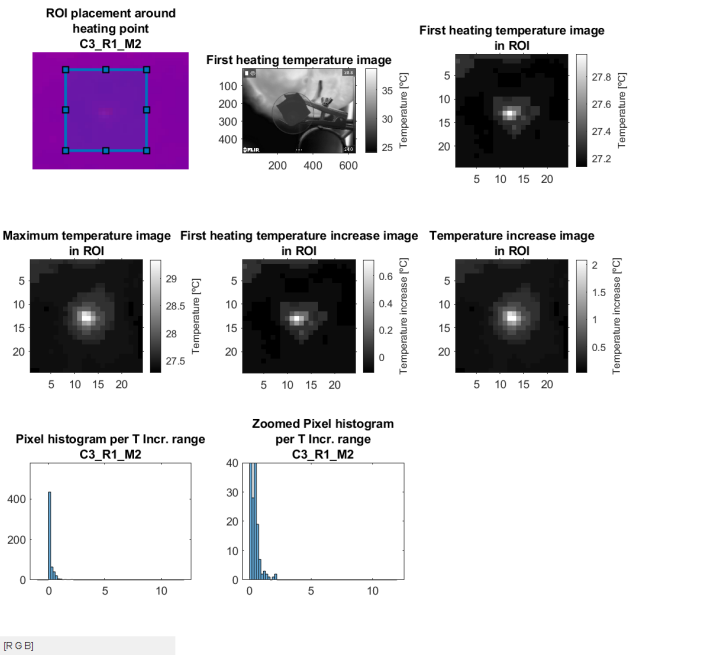

Fig. 87. Thermography images and histograms of Measurement C3_R1_M2

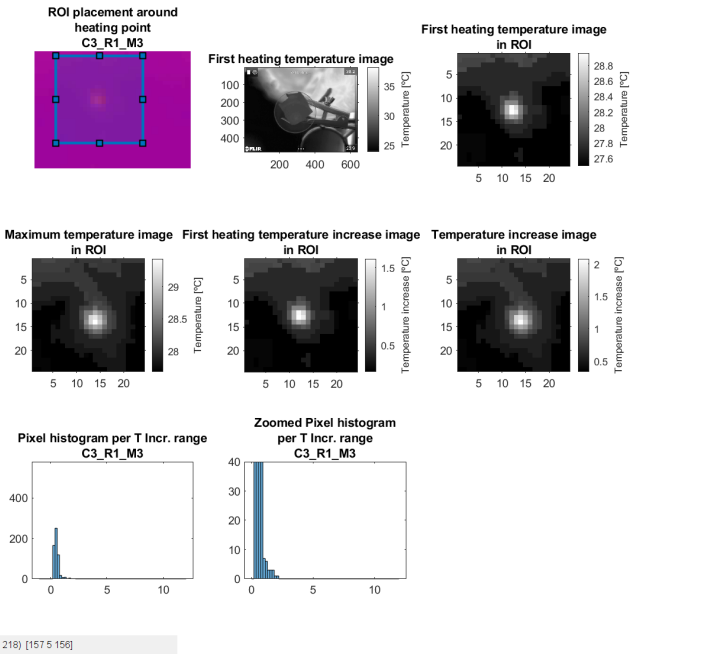

Fig. 88. Thermography images and histograms of Measurement C3_R1_M3

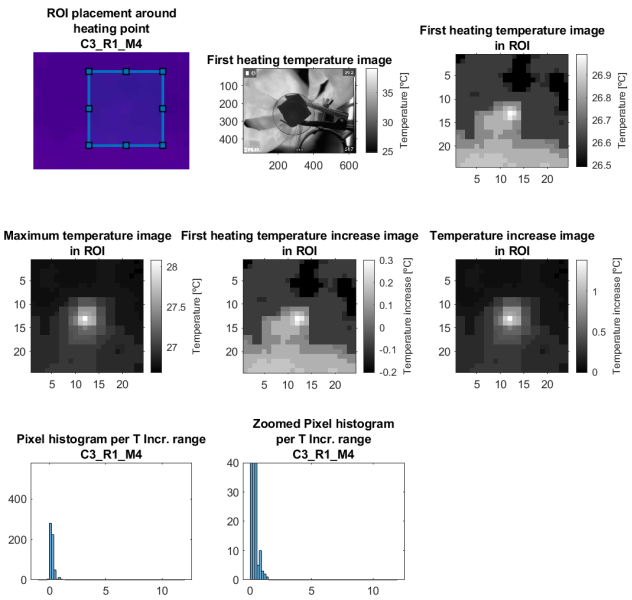

Fig. 89. Thermography images and histograms of Measurement C3_R1_M4

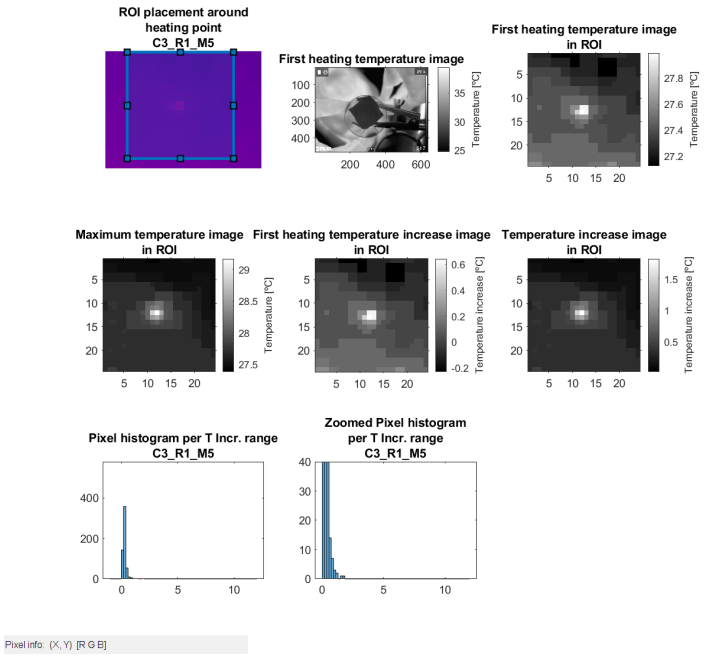

Fig. 90. Thermography images and histograms of Measurement C3_R1_M5

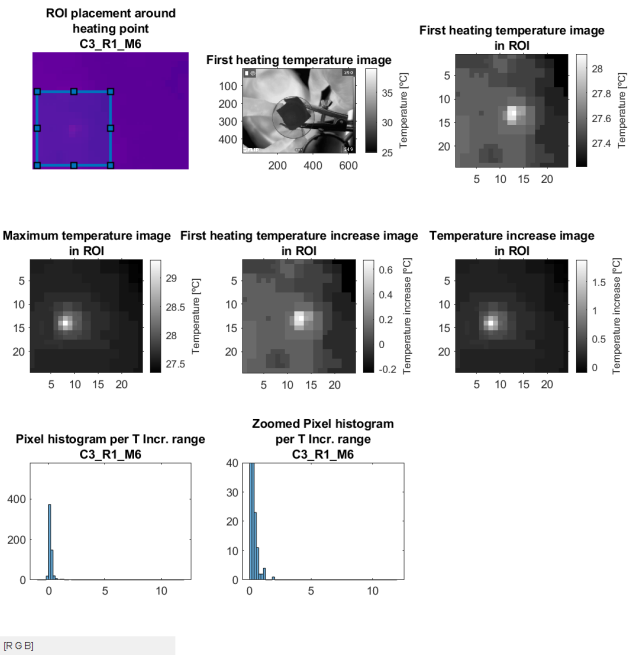

Fig. 91. Thermography images and histograms of Measurement C3_R1_M6

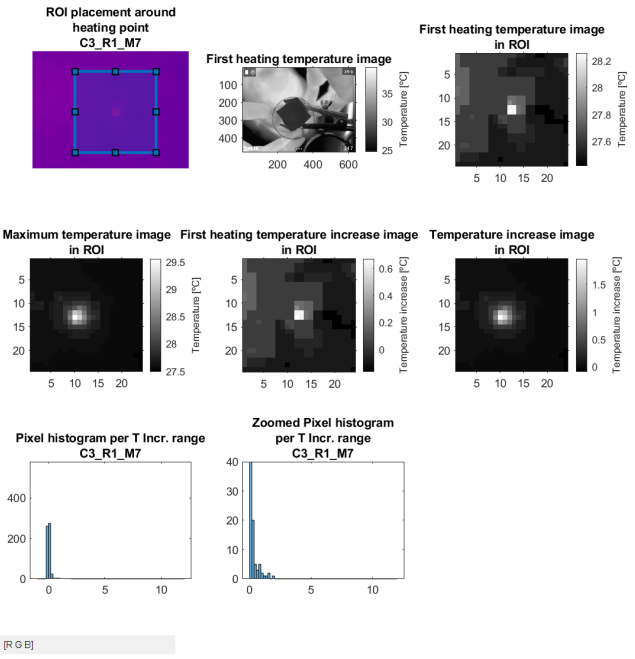

Fig. 92. Thermography images and histograms of Measurement C3_R1_M7

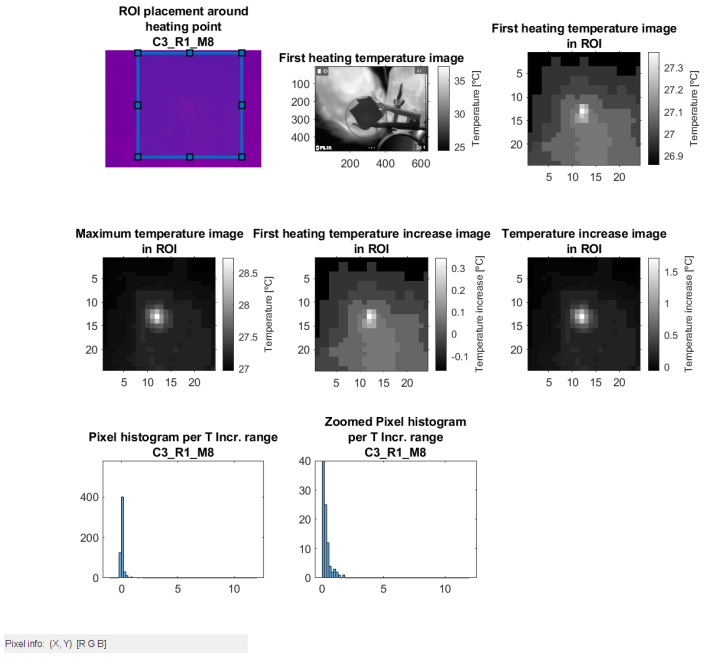

Fig. 93. Thermography images and histograms of Measurement C3_R1_M8

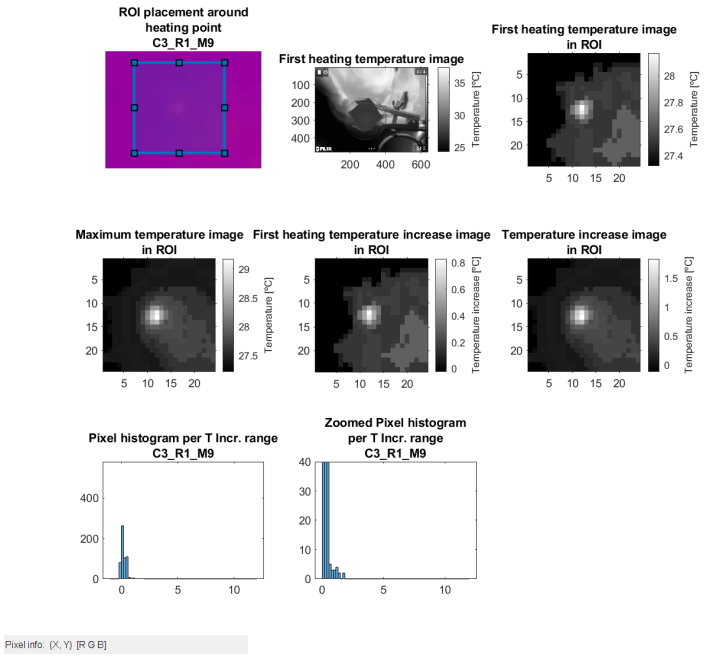

Fig. 94. Thermography images and histograms of Measurement C3_R1_M9

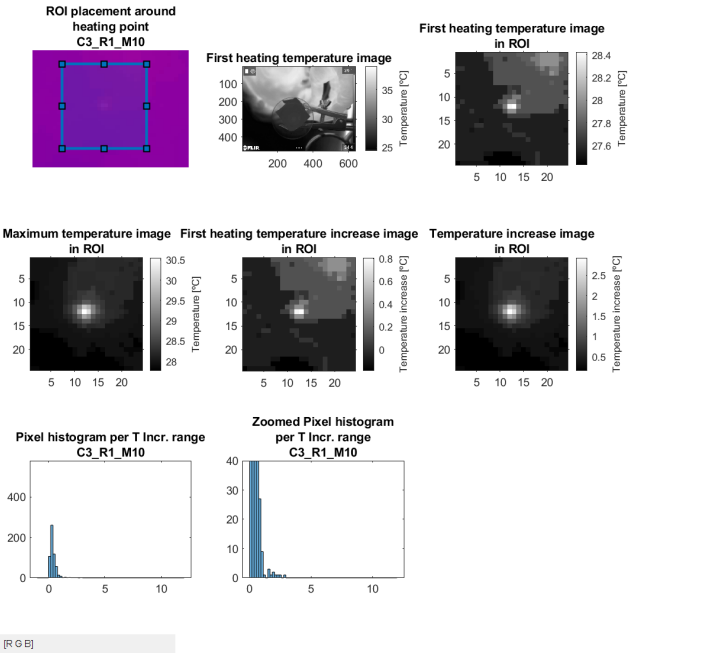

Fig. 95. Thermography images and histograms of Measurement C3_R1_M10

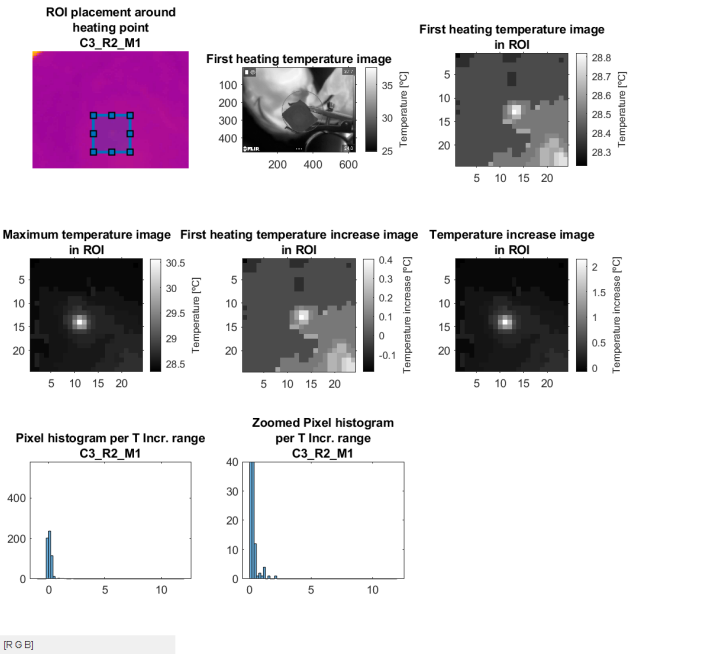

Fig. 96. Thermography images and histograms of Measurement C3_R2_M1

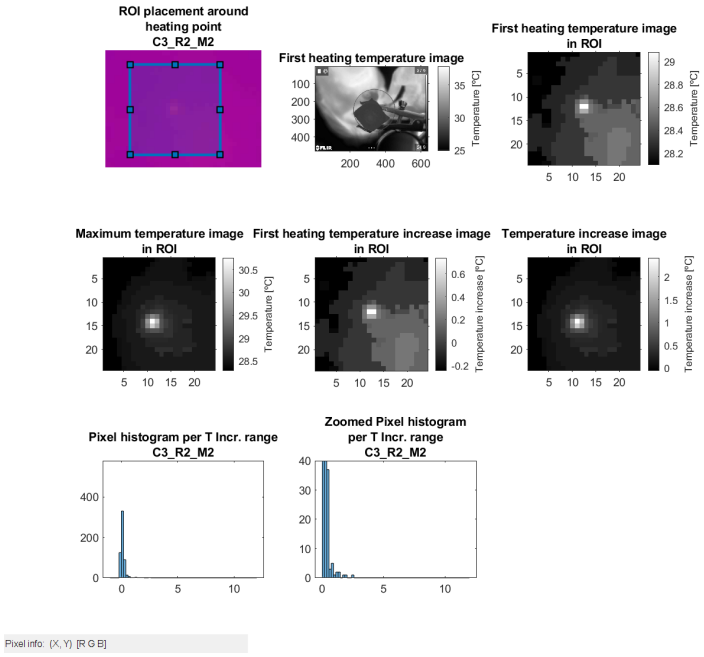

Fig. 97. Thermography images and histograms of Measurement C3_R2_M2

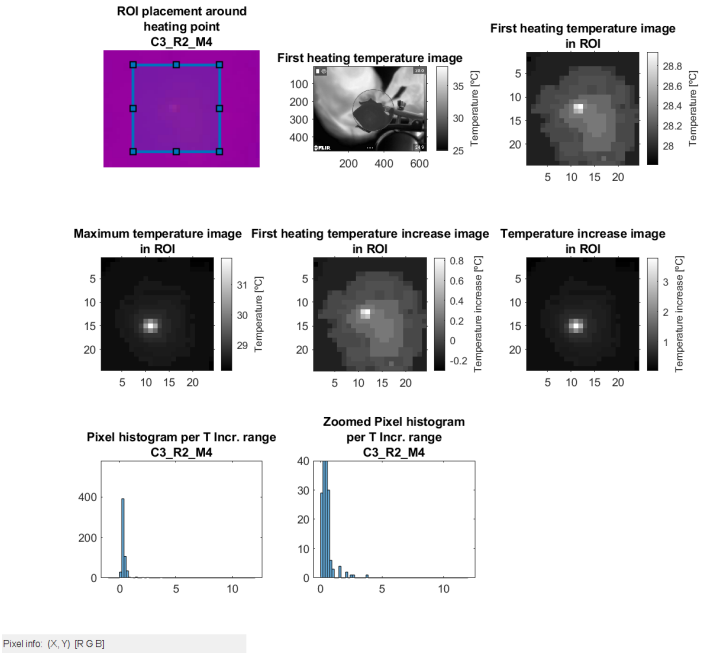

Fig. 99. Thermography images and histograms of Measurement C3_R2_M4

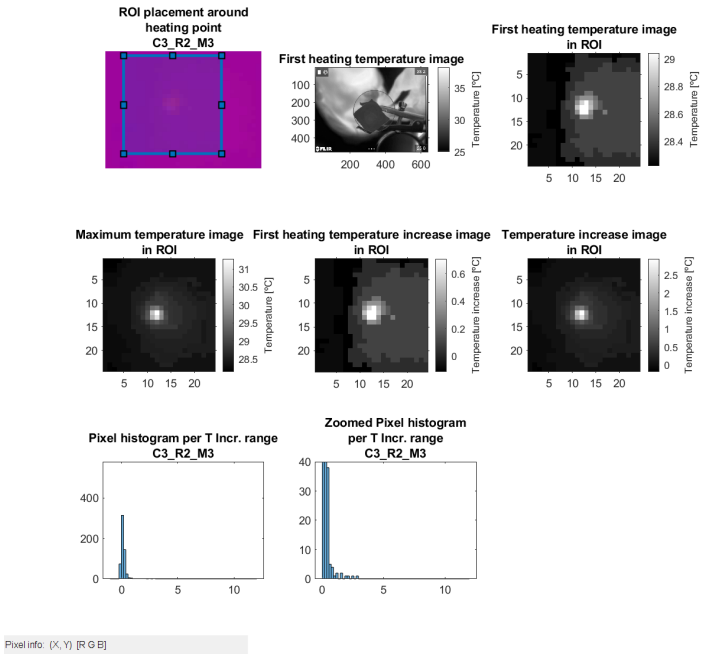

Fig. 98. Thermography images and histograms of Measurement C3_R2_M3

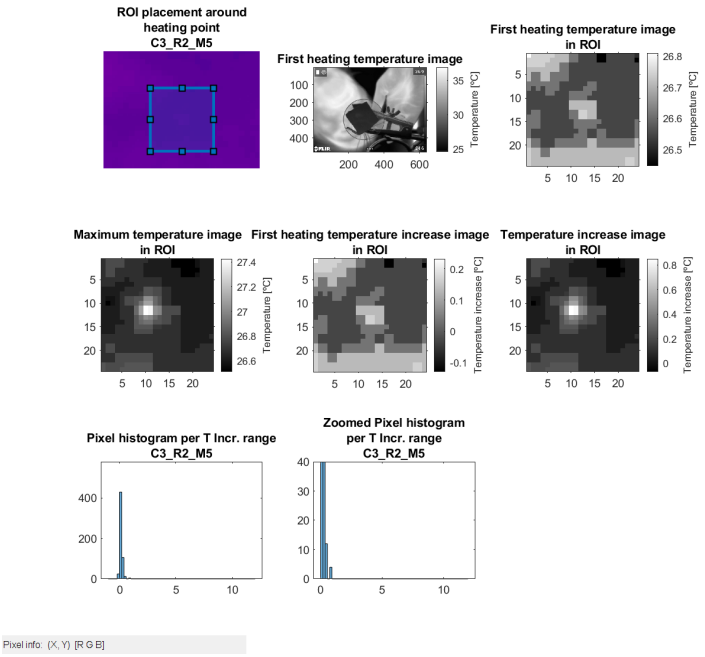

Fig. 100. Thermography images and histograms of Measurement C3_R2_M5

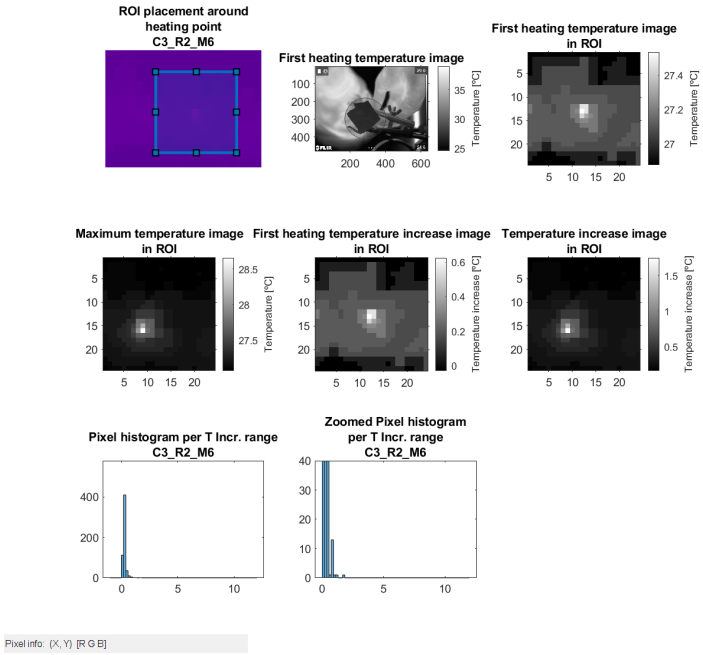

Fig. 101. Thermography images and histograms of Measurement C3_R2_M6

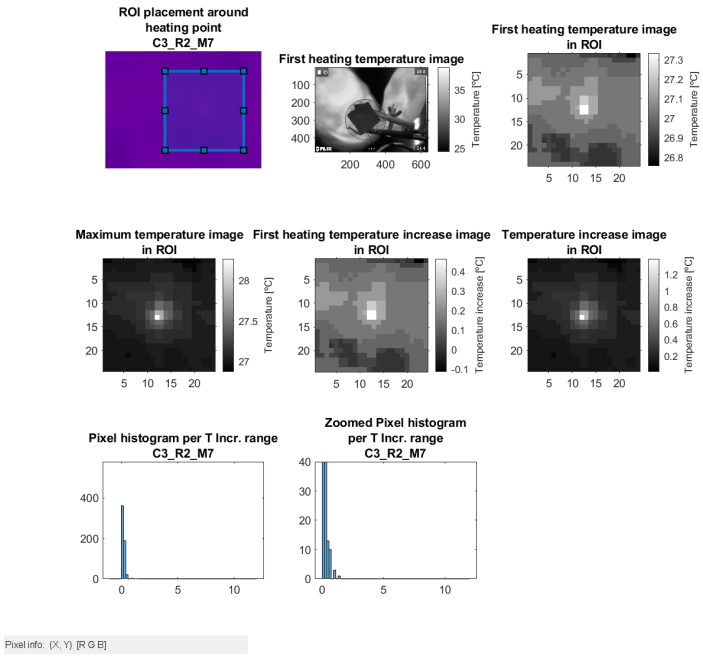

Fig. 102. Thermography images and histograms of Measurement C3_R2_M7

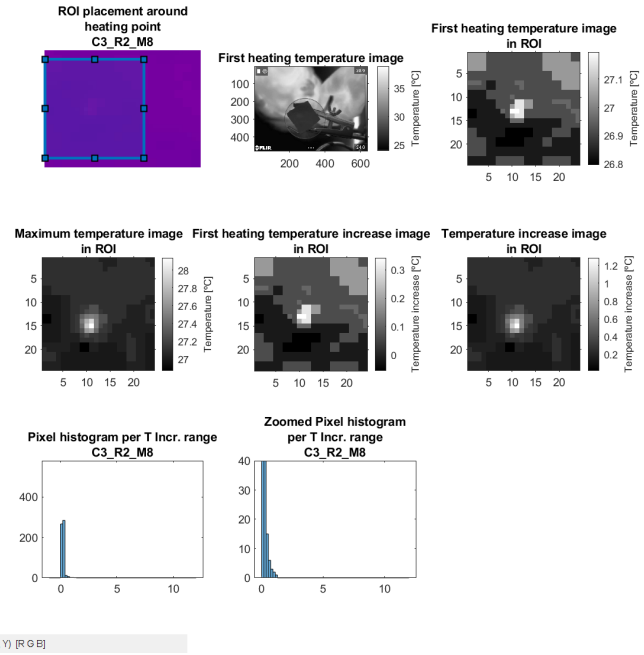

Fig. 103. Thermography images and histograms of Measurement C3_R2_M8

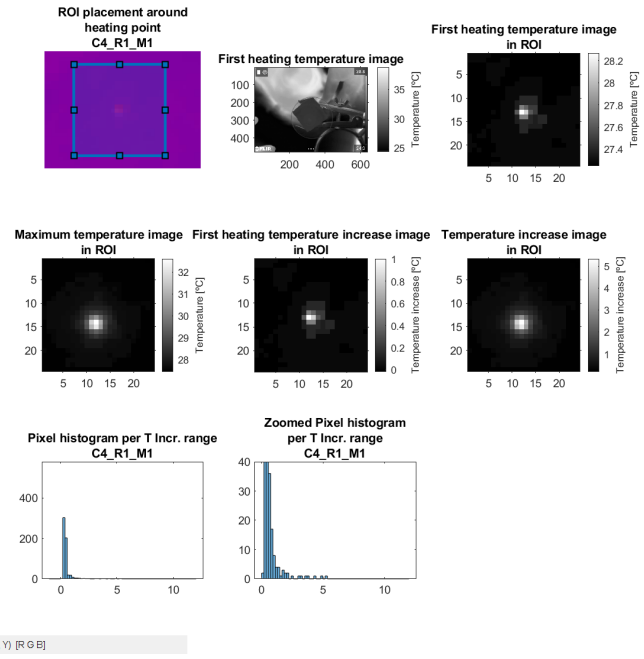

Fig. 104. Thermography images and histograms of Measurement C4_R1_M1

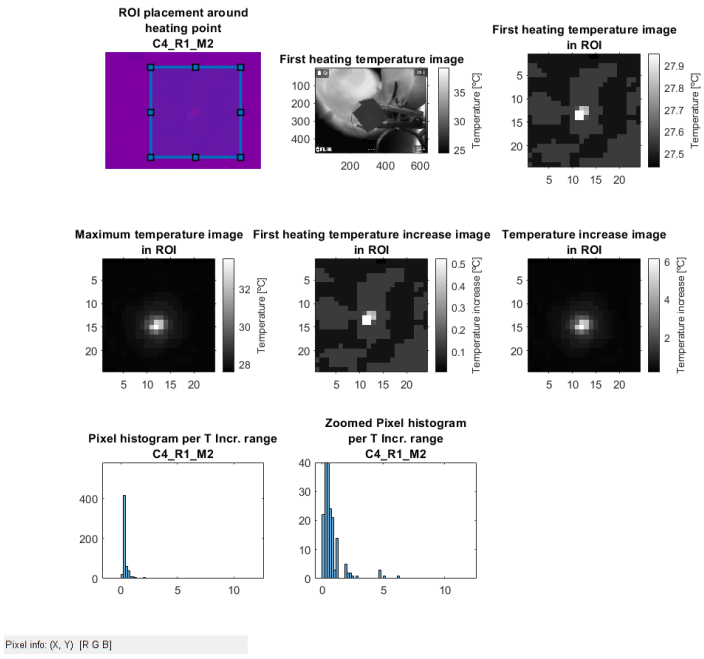

Fig. 105. Thermography images and histograms of Measurement C4_R1_M2

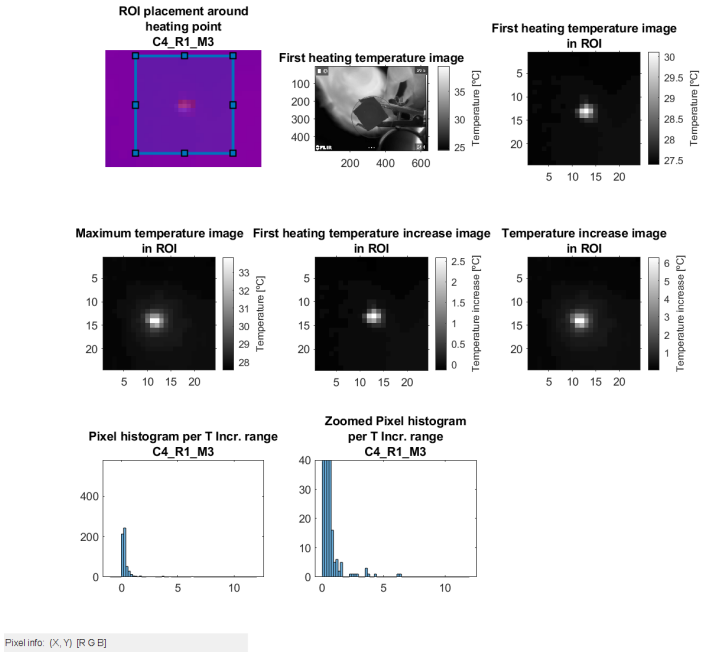

Fig. 106. Thermography images and histograms of Measurement C4_R1_M3

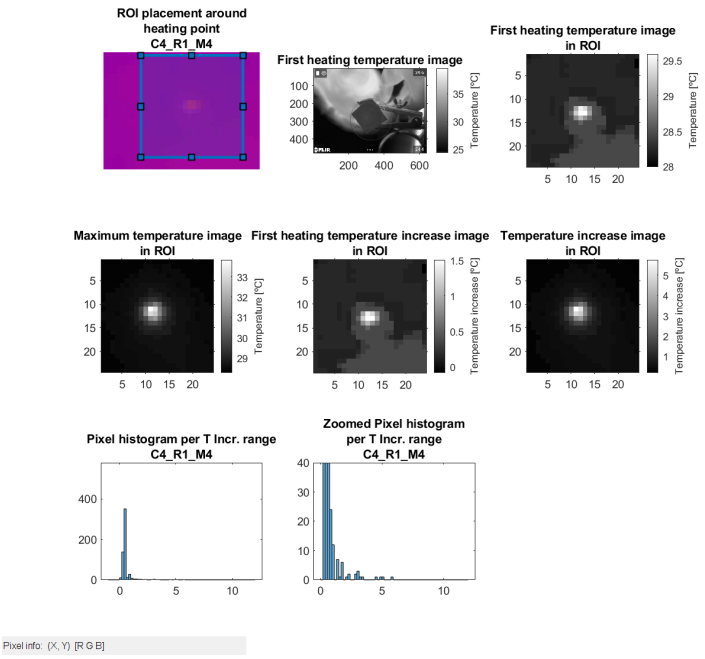

Fig. 107. Thermography images and histograms of Measurement C4_R1_M4

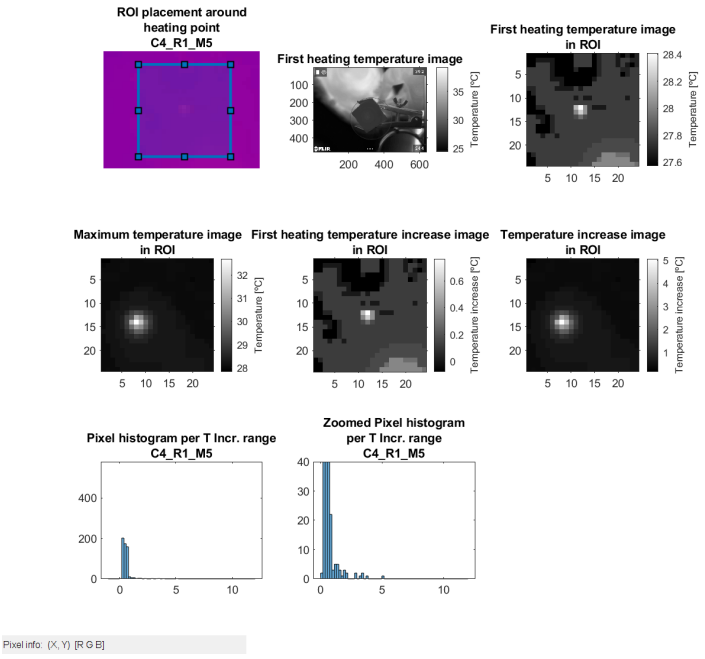

Fig. 108. Thermography images and histograms of Measurement C4_R1_M5

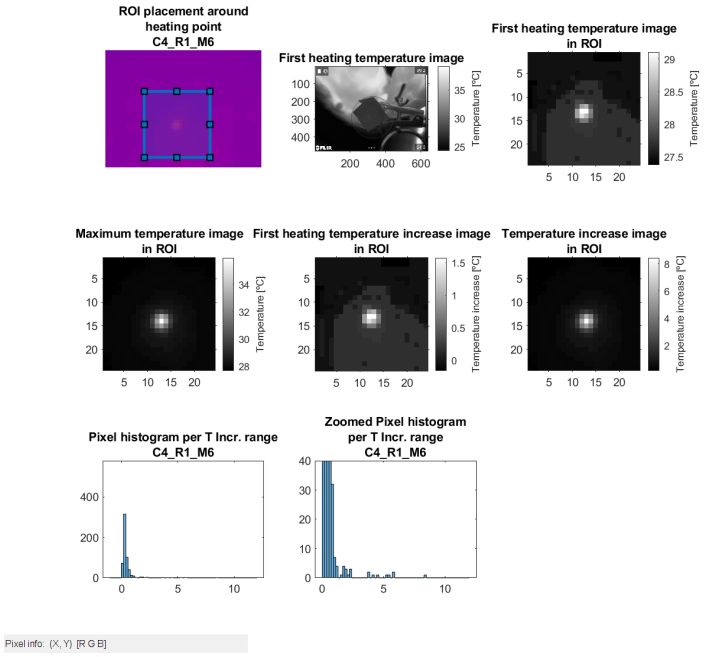

Fig. 109. Thermography images and histograms of Measurement C4_R1_M6

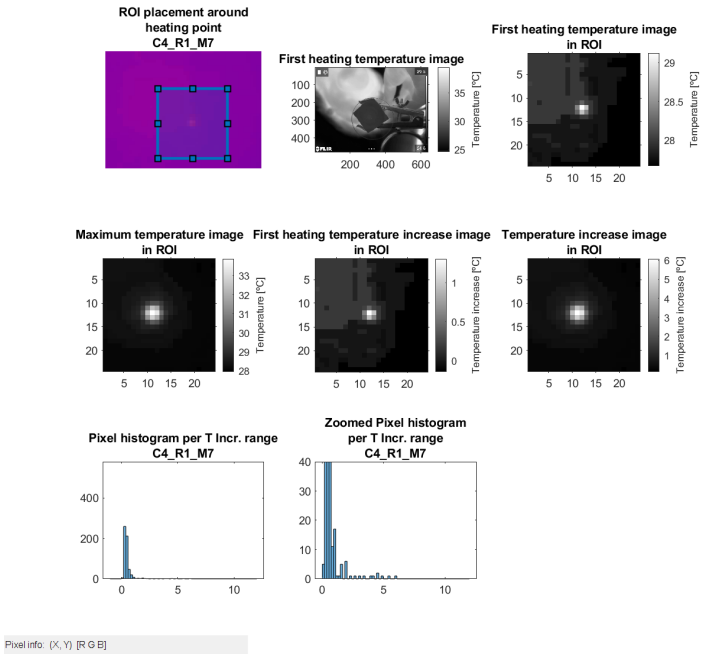

Fig. 110. Thermography images and histograms of Measurement C4_R1_M7

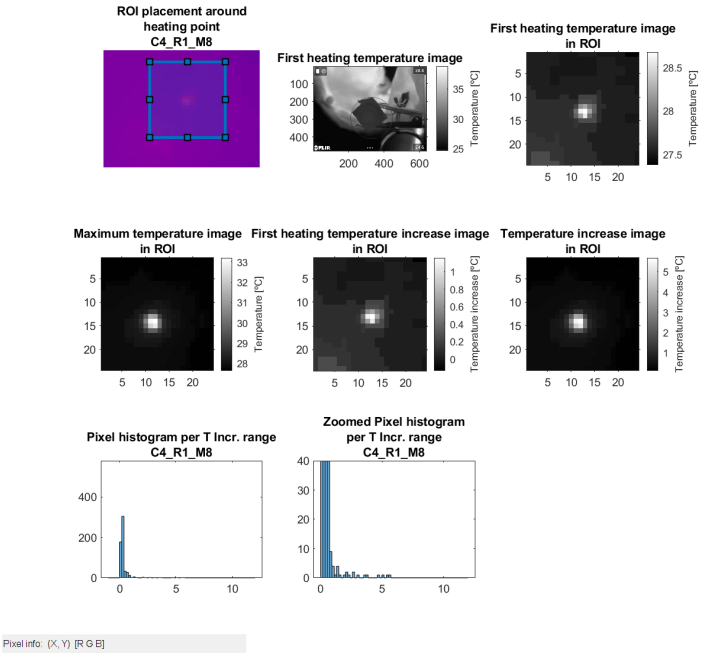

Fig. 111. Thermography images and histograms of Measurement C4_R1_M8

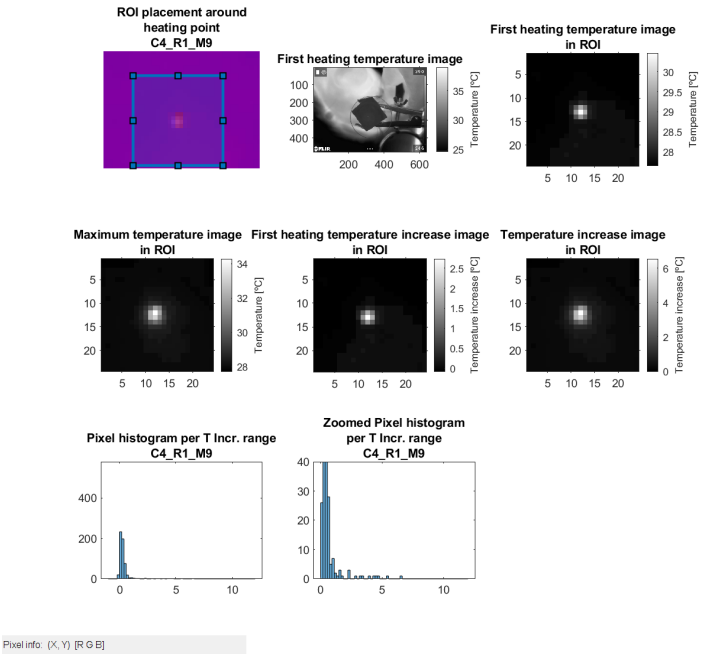

Fig. 112. Thermography images and histograms of Measurement C4_R1_M9

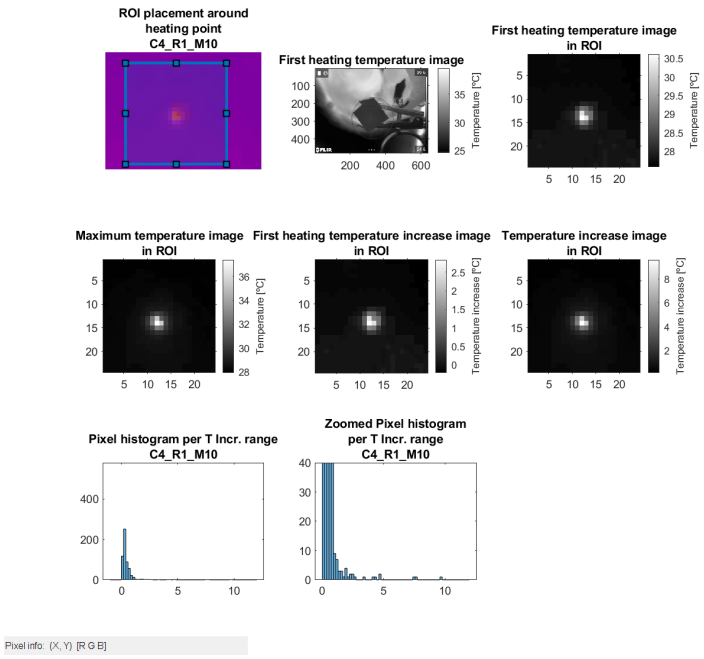

Fig. 113. Thermography images and histograms of Measurement C4_R1_M10

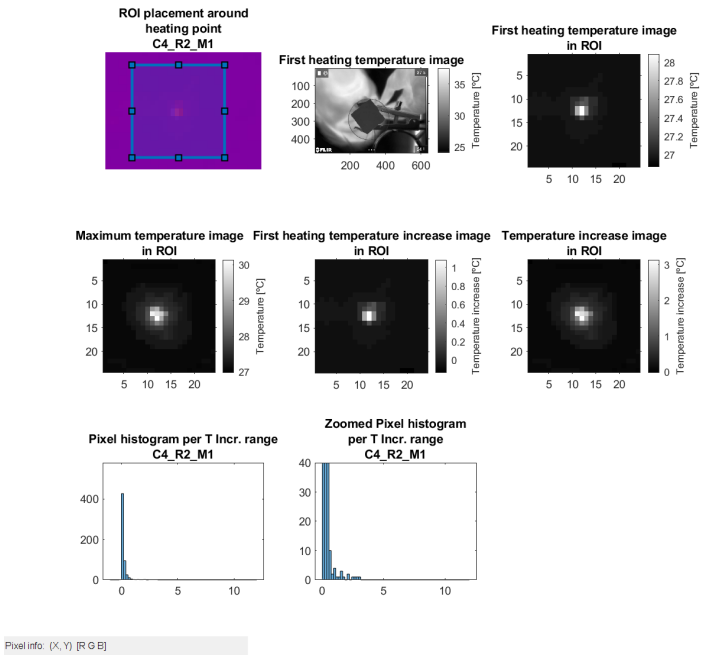

Fig. 114. Thermography images and histograms of Measurement C4_R2_M1

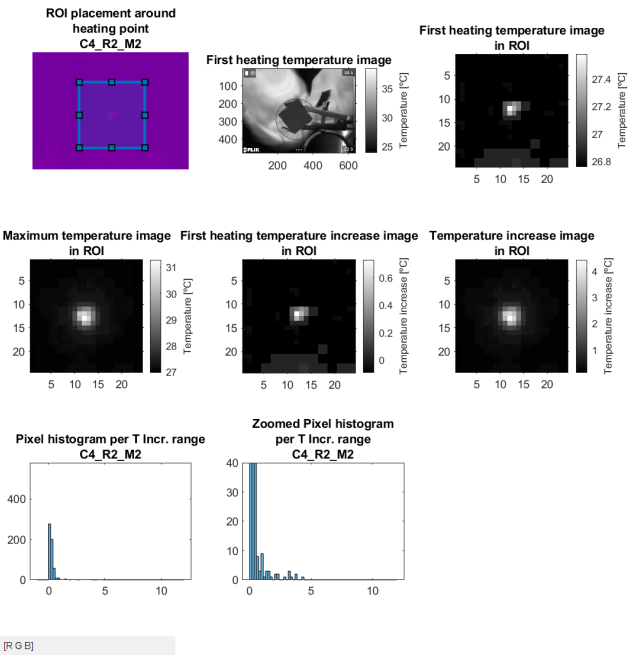

Fig. 115. Thermography images and histograms of Measurement C4_R2_M2

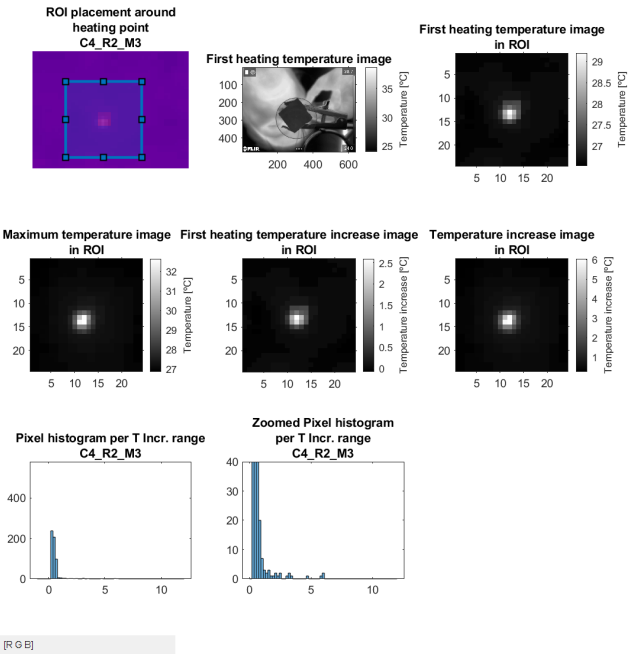

Fig. 116. Thermography images and histograms of Measurement C4_R2_M3

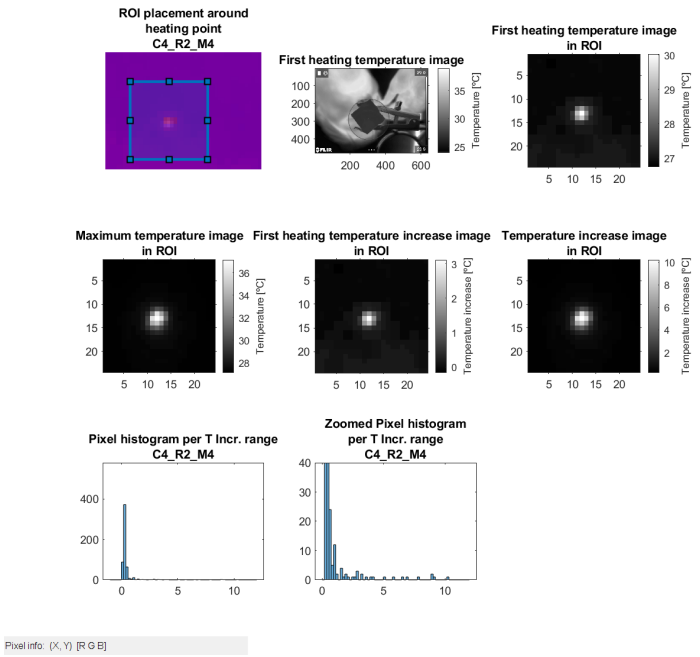

Fig. 117. Thermography images and histograms of Measurement C4_R2_M4

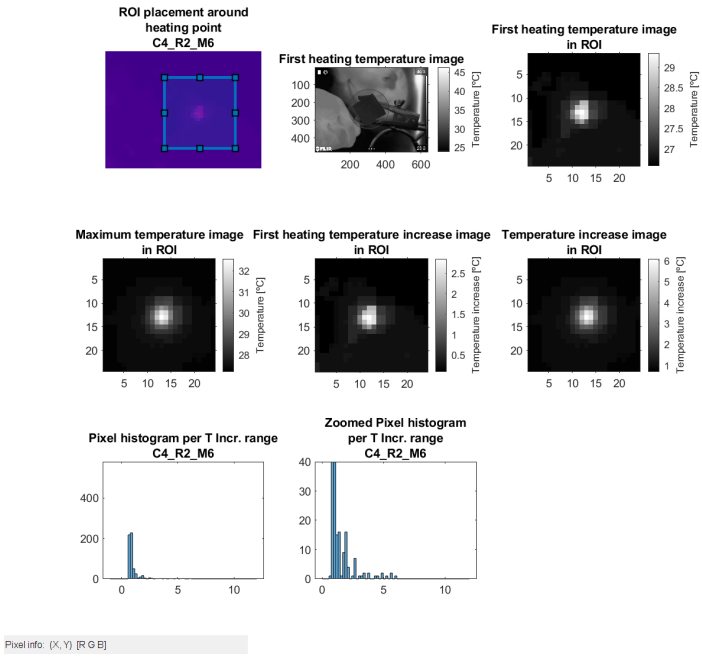

Fig. 118. Thermography images and histograms of Measurement C4_R2_M6

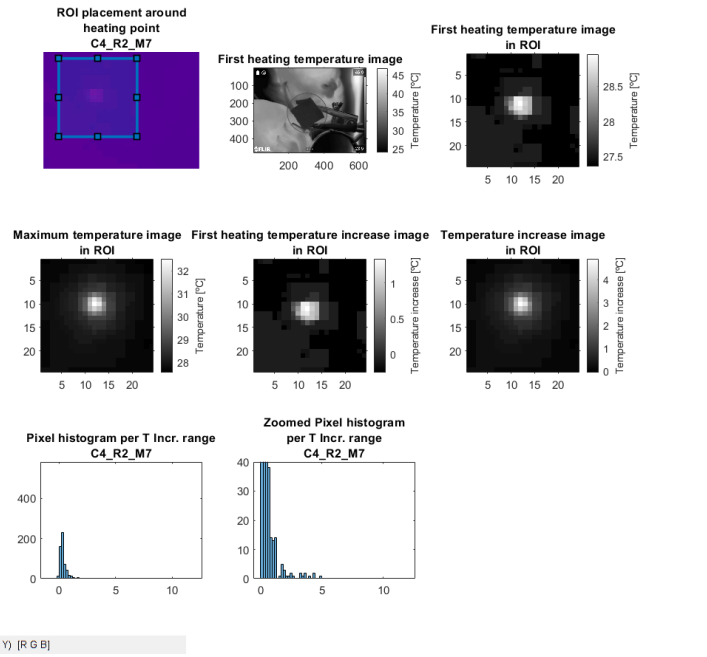

Fig. 119. Thermography images and histograms of Measurement C4_R2_M7

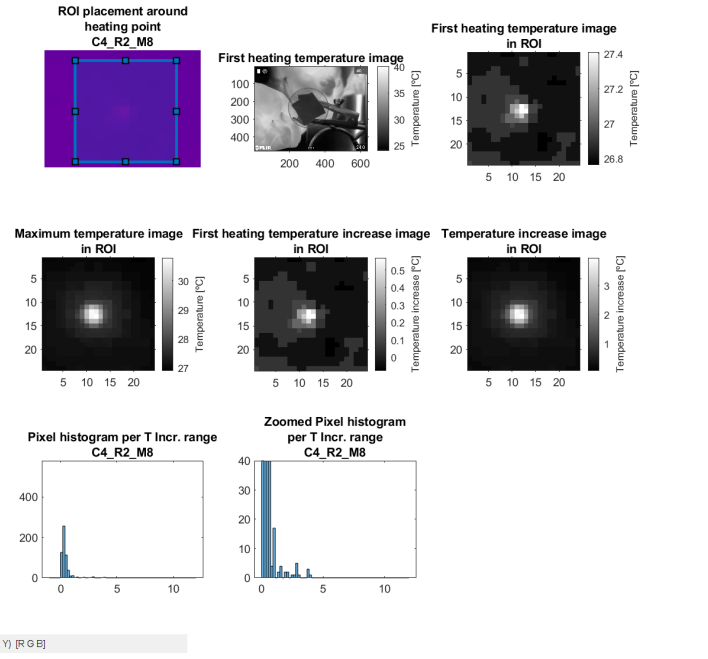

Fig. 120. Thermography images and histograms of Measurement C4_R2_M8

APPENDIX Q
ALL SENSOR TEMPERATURE GRAPHS

In this appendix, the graphs of the measurements of sensor 1 are shown per repetition. In these graphs, the real-time moment at which the corresponding thermography measurement shows the maximum temperature increase is denoted with an asterisk. The real time heating duration measured at the corresponding thermography measurement is indicated in orange. When different legends are present in these figures, the measurements to which these legends refer are indicated. These graphs are created using the script 'DataProcessing.m', which can be downloaded via this link.

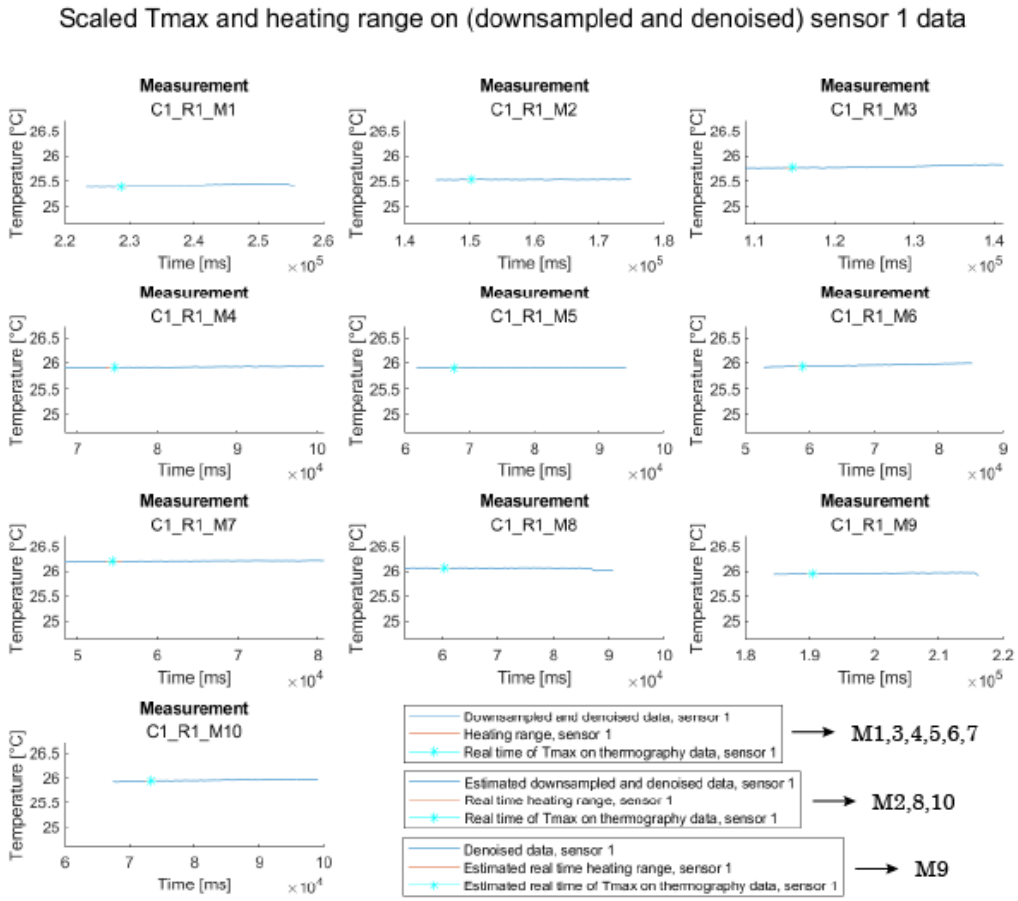

Fig. 121. Sensor measurements of Repetition C1_R1

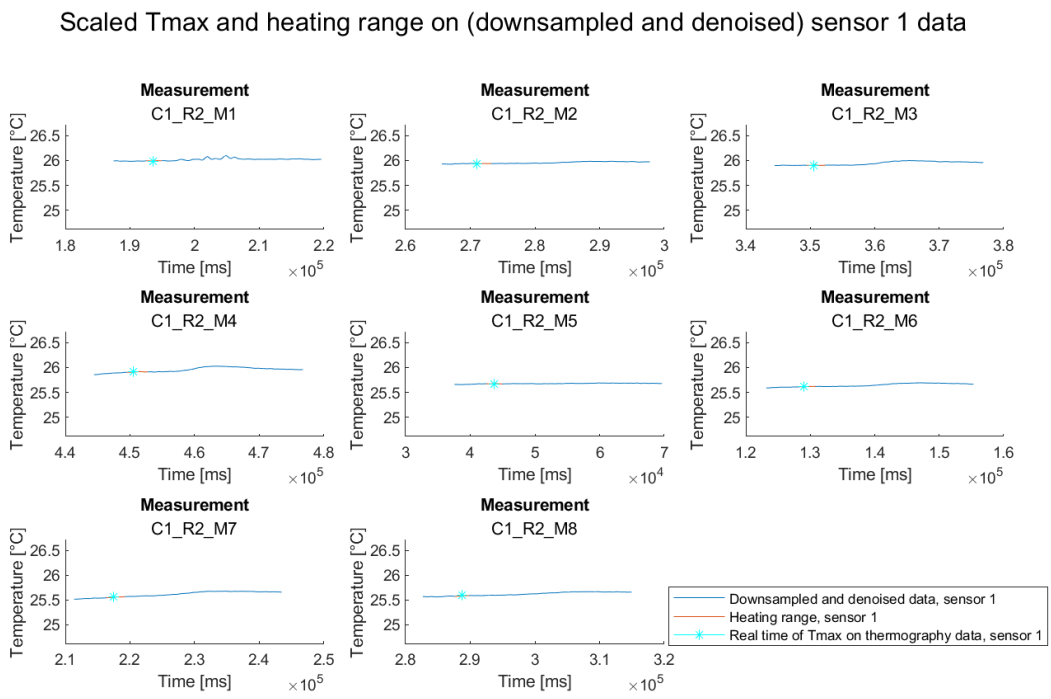

Fig. 122. Sensor measurements of Repetition C1_R2

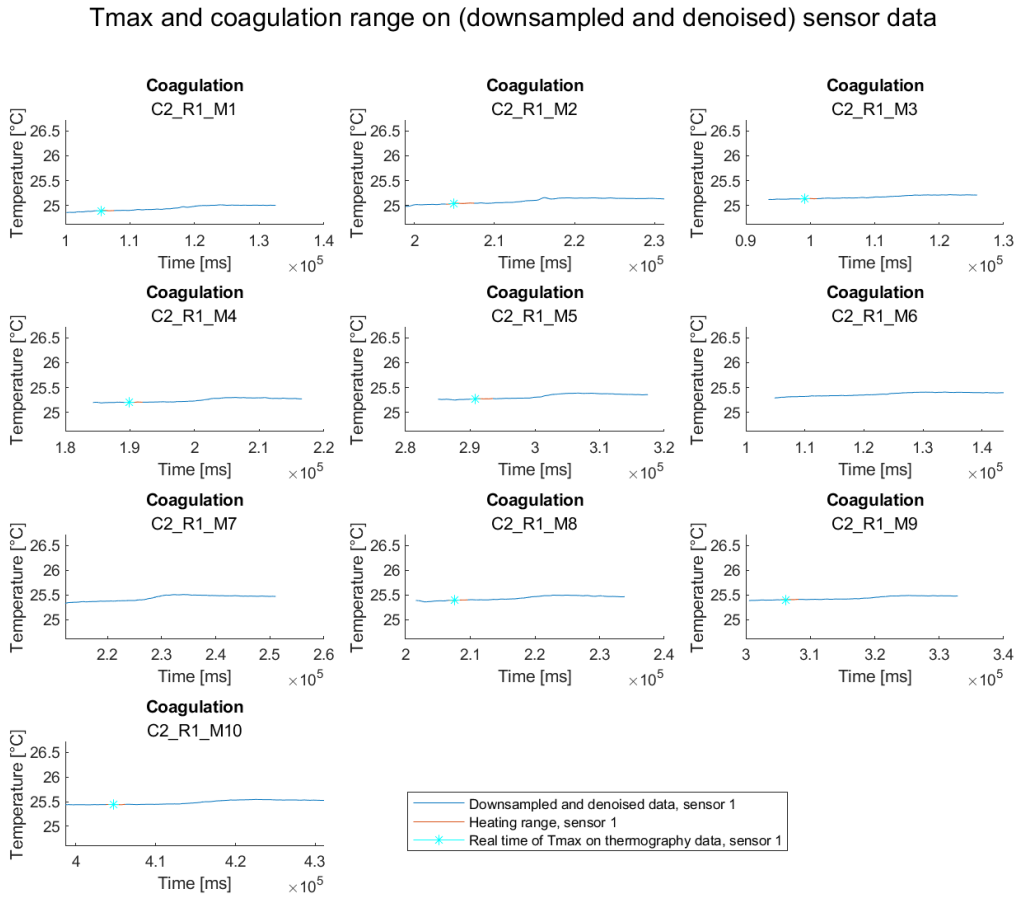

Fig. 123. Sensor measurements of Repetition C2_R1

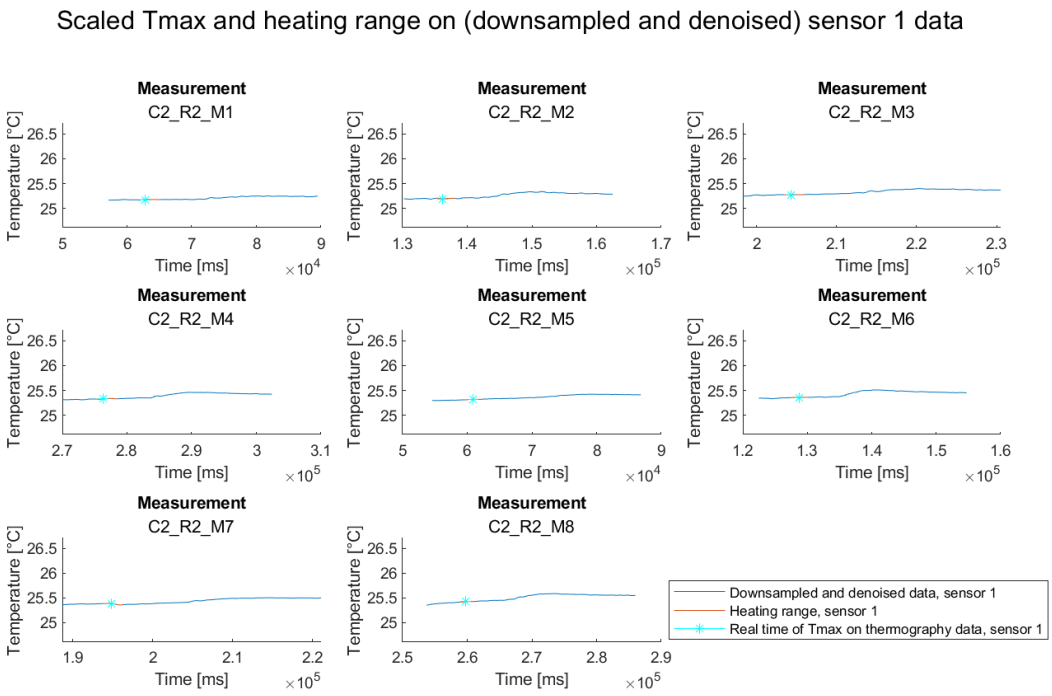

Fig. 124. Sensor measurements of Repetition C2_R2

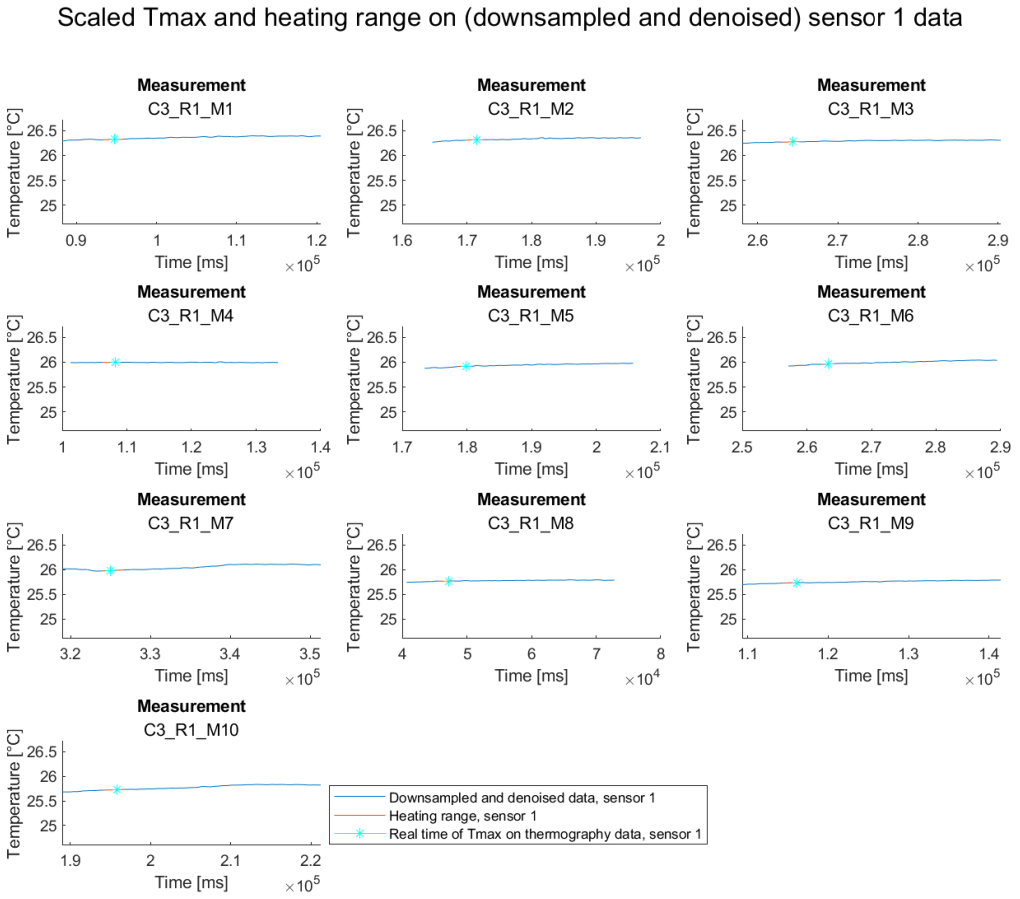

Fig. 125. Sensor measurements of Repetition C3_R1

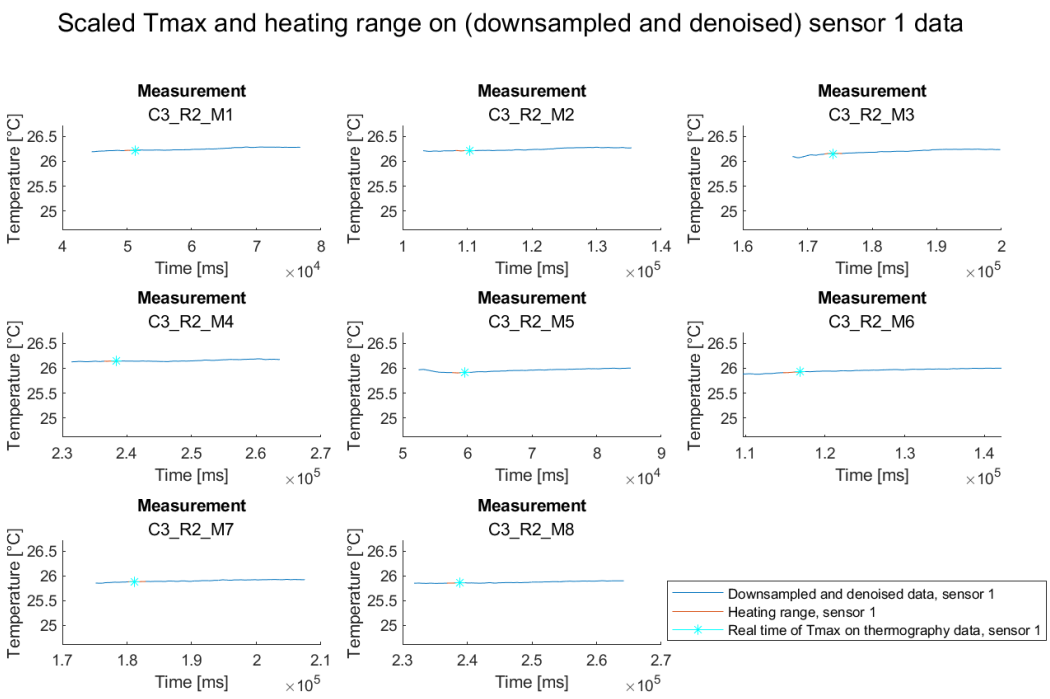

Fig. 126. Sensor measurements of Repetition C3_R2

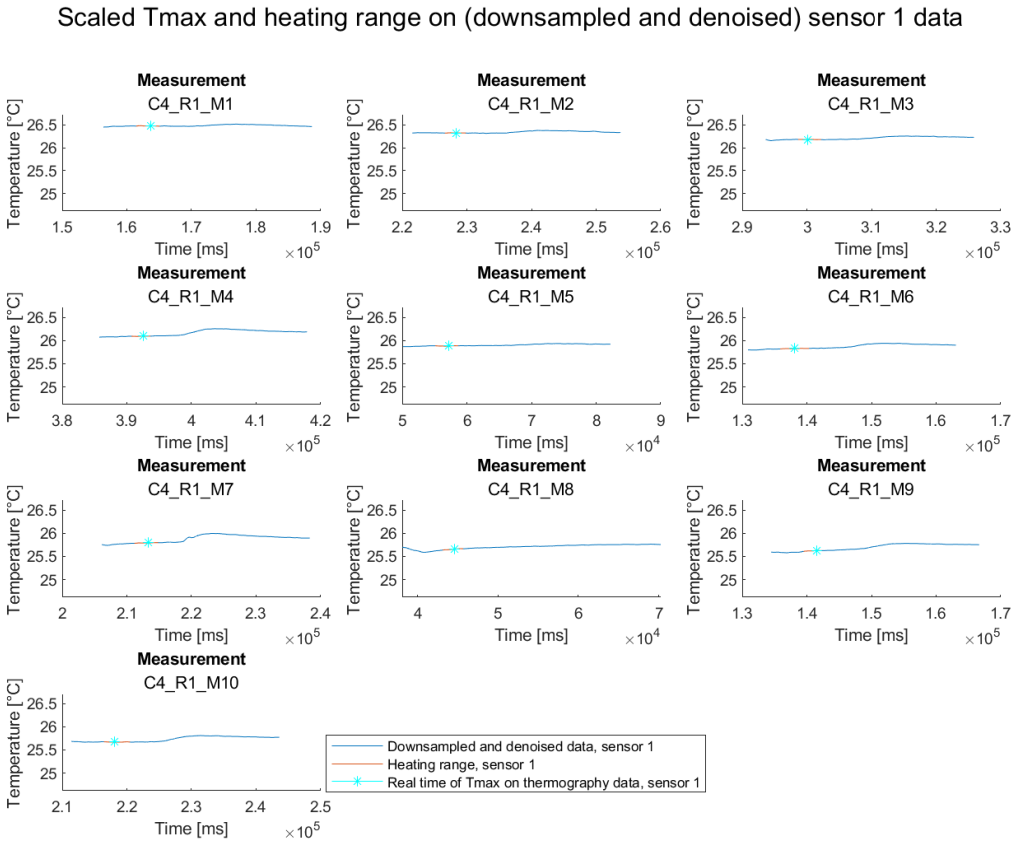

Fig. 127. Sensor measurements of Repetition C4_R1

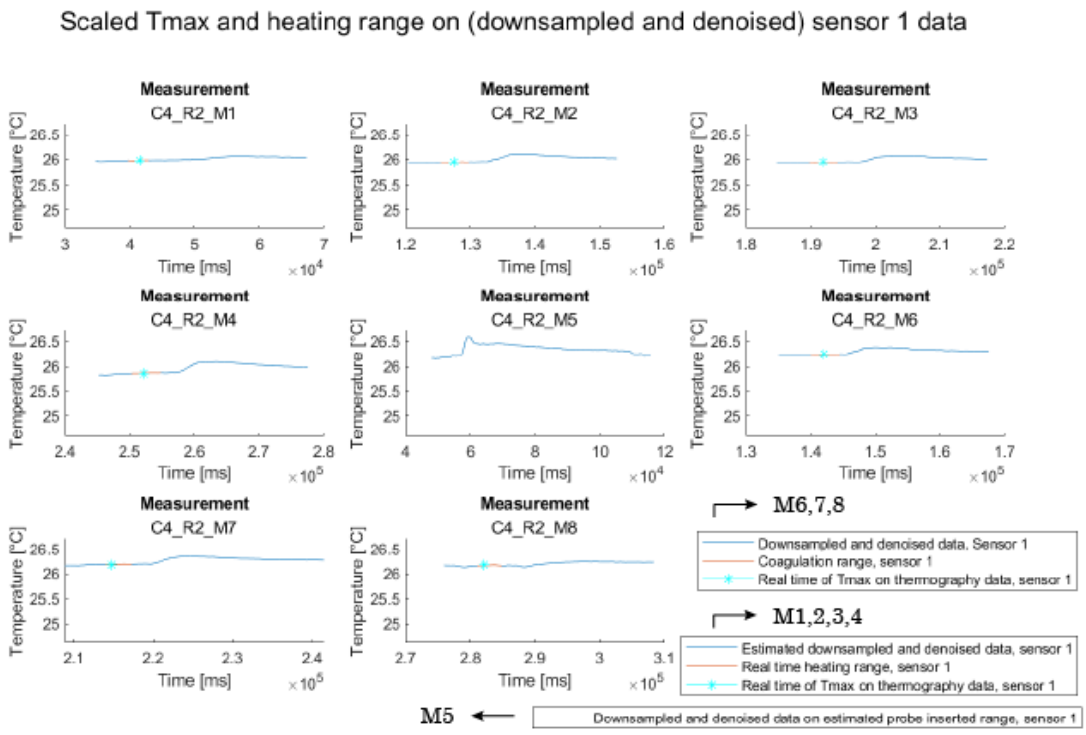

Fig. 128. Sensor measurements of Repetition C4_R2

APPENDIX R
SUBSET MEASUREMENTS LIST

The following measurements are included in the comparison of error and mean temperature increase.

- C1_R1_M1
- C1_R1_M3
- C1_R2_M1
- C2_R1_M1
- C2_R1_M2
- C2_R1_M3
- C2_R1_M4
- C2_R1_M5
- C2_R1_M6
- C2_R1_M7
- C2_R1_M8
- C2_R1_M9
- C2_R1_M10
- C2_R2_M1
- C2_R2_M2
- C2_R2_M3
- C2_R2_M4
- C2_R2_M5
- C2_R2_M6
- C2_R2_M7
- C2_R2_M8
- C3_R1_M2
- C3_R1_M7
- C3_R1_M10
- C3_R2_M1
- C3_R2_M2
- C3_R2_M3
- C3_R2_M4
- C4_R1_M1
- C4_R1_M2
- C4_R1_M3
- C4_R1_M4
- C4_R1_M5
- C4_R1_M6
- C4_R1_M7
- C4_R1_M8
- C4_R1_M9
- C4_R1_M10
- C4_R2_M1
- C4_R2_M2
- C4_R2_M3
- C4_R2_M4
- C4_R2_M6
- C4_R2_M7
- C4_R2_M8

APPENDIX S
EVALUATION OF HEATING DURATION

When looking at the mean heating duration, a higher energy value provides a higher mean duration. There is no direct trend for the same energy conditions or the same application time conditions. However, within both energy conditions, an application time of 2” result in longer a heating duration, with a minimum of 19 frames, which indicates that application time has a higher influence on the heating duration than the power setting.

The frame rate of the thermal camera leads to an average of 23 frames in 1” and an average of 46 frames in 2”. The amount of frames until maximum temperature in the conditions applying 1” (19 ± 6 and 21 ± 5 frames) and the conditions applying 2” (37 ± 8 and 41 ± 9 frames) almost represent the frame rate of the thermal camera. The difference between the amount of frames until the maximum temperature and the actual amount of frames per second could be explained by the assumption that there are a few frames at the beginning of the coagulation at which the heat is not yet transferred through the retinal tissue, or the assumption that the temperature increase in the first frames is too low in order to be identified visually.

Literature Review

Electrical Engineering Challenges of Intraocular Diathermy Forceps: A Narrative Literature Review

L. Grooten
Study Number: 4501373
Biomedical Engineering, Delft University of Technology

***Abstract*—*Introduction:* The intraocular diathermy forceps is thought to be beneficial to the conventional diathermy probe in controlling vessel bleeding during vitreous surgery. It is not researched why this instrument is not introduced to the clinical market yet.**
***Objective:* The aim of this literature review is to identify electrical engineering challenges in designing the intraocular diathermy forceps.**
***Methods:* Online databases Google Scholar, PubMed and ScienceDirect are used to identify five reviewed instruments, six electrical engineering aspects and the introductory theory.**
***Results:* The intraocular diathermy forceps shows a higher closure rate, lower energy requirements and lower application times than the conventional intraocular diathermy probe. In a clinical trial, the diathermy forceps showed a closure rate of 100%. In an open-sky experiment, the output current and the heat dissipation of the insulated diathermy forceps was lower than the uninsulated diathermy forceps and the conventional diathermy probe. Unequal cooling times, differences in fluid depth and the inability of thermography to measure retinal temperature underneath fluid leads to influenced current and heat dissipation results.**
***Discussion:* The results suggest that the diathermy forceps is beneficial but the challenges create a need for a larger quantitative clinical study and optimization of thermal spread measurement.**
***Conclusion:* Addressing the found challenges could lead to the introduction of the intraocular diathermy forceps and redesign of experimental methods could contribute to validation of intraocular diathermy instruments.**

***Index Terms*—Bipolar Microforceps, Challenges, Coagulation, Diathermy Forceps, Electrosurgery, Intraocular, Neurosurgical, Thermal Spread**

I. Introduction

During intraocular vitreous surgery, whereat vitreous humour is removed from the eye with a vitrectomy cutter in a laparoscopic approach, retinal breaks and vessel bleeding can occur [1]. To control this bleeding, intraocular diathermy is applied as can be seen in Figure 1.

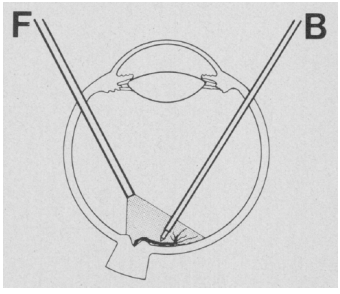

Fig. 1. Diathermy application with bipolar probe (B) and assisting fiber optic probe (F). Figure adapted from [2]

The intraocular diathermy instrument was initially developed as a monopolar system, but as this led to adversities, a bipolar probe is developed in 1983 [1]. Although there have been no major changes made in the design of the bipolar diathermy probe up to date, current use of this bipolar probe is thought to have adversities as well. This is because this probe is only applied to one side of the bleeding vessel, it blocks the surgeons view and it has to be exchanged with an additional instrument. The latter creates a delay which could lead to difficulties with bleeding control [3].

An instrument that has to be exchanged with the diathermy probe is the microforceps. This instrument is used for membrane peeling and removal during or after vitrectomy [4]. In attempt to provide mechanical compression at both sides of vessels and avoid instrument exchange, the intraocular diathermy forceps is developed by modifying the microforceps into a diathermy instrument [3].

Although this new instrument is patented and tested in an animal cadaver study as well as a clinical trial [5, 3, 6], this instrument is not introduced to the clinical market yet. Whether this is due to the lack of sufficient proof of superiority over the conventional diathermy, due to the need for design optimization of the diathermy forceps itself or due to the absence of need for diathermy optimization is not researched up to date. A literary analysis on electrical engineering challenges of the intraocular diathermy forceps could potentially provide insight in this question. Consequently, the generated knowledge from this literature could lead to future projects with the aim to improve the medical application of diathermy.

A conventional bipolar forceps exists and is widely used in other surgical areas [7]. However, the size and configuration of this instrument is not suitable for the micro laparoscopic approach and differs considerably from the intraocular diathermy instruments. To enhance areas of optimization of the intraocular diathermy forceps, challenges found in similar developments from other micro-surgical areas are included.

Hence, the aim of this work is to identify electrical engineering challenges in designing the intraocular diathermy forceps, by conducting a narrative review of existing literature concerning the intraocular diathermy forceps, similar bipolar microforceps developments and existing diathermy probes.

II. Methods

A first search is performed in order to identify the similar bipolar microforceps developments that are reviewed. In this search, potentially relevant articles are extracted from

databases Google Scholar and PubMed by using search terms including *diathermy*, *forceps*, *microforceps*, *bipolar*, *coagulation*, *miniaturized*, *23-gauge*, *single-shaft*, *development*, *microcoagulation*, *peeling device*, *tweezer*, *grasper*, *microsurgery* and *small-size*. These terms are used in different orders and combinations. The exact search strings used are described in Appendix A. For the Google Scholar searches, a publication year filter of 2000-2021 is applied. A few additional articles are identified from reference lists of found articles.

The reviewed developments are elected by filtering the found articles from the first search. Therefor the abstracts and introduction of these articles are scanned, and inclusion and exclusion criteria are applied. The main inclusion criterion is *'the article describes a surgical instrument (development) containing a peeling function as well as a bipolar diathermy function'*. Additional inclusion criteria specific for this instrument (development) included *'a maximum shaft or tube diameter of 2 mm'* and *'the peeling elements are metal-based'*.

The applied exclusion criteria are *'the article is not available in English language or English translation'*, *'the article cannot be downloaded or is not fully accessible online'* and *'the instrument development described in the article is a modification of a bipolar forceps (such as the Non-stick Bipolar Forceps of Kirwan Surgical Products Inc. [7])'*.

After applying these criteria, two articles containing similar instrument developments are selected for this review in addition to several articles concerning the intraocular diathermy forceps, the monopolar diathermy probe and the bipolar diathermy probe.

In order to identify the electrical engineering aspects for the analysis, a second search is performed on Google Scholar using search strings *'design AND challenges AND bipolar AND microforceps AND coagulation'* and *'electrosurgical principles'*, with a publication year filter of 2000-2021. As this search led to subjective selection of aspects, no filtering of the found literature is applied. Additional electrical engineering aspects are identified from specific design topics that are described in the articles concerning the instrument developments.

For the introductory theory section of each electrical engineering aspect, a separate search is conducted on several databases such as ScienceDirect, Google Scholar and PubMed. Search terms related to the specific electrical engineering aspect are used in combination with terms including *diathermy*, *electrosurgery*, *electrosurgical instruments*, *electrode* and *coagulation*. Relevant literature is detected by scanning the title and abstract. As these searches are based on a specific topic and the information is selected subjectively, the information is retrieved directly without filtering of search results.

III. Results

Instrument Description

The selected instruments for this review are the monopolar diathermy probe, the bipolar diathermy probe, the intraocular diathermy forceps, the neurosurgical bipolar microforceps and the bipolar grasping cautery tool. To provide an image of these instruments, their design and working principle are described in this section.

1) Monopolar and Bipolar Intraocular Diathermy Probe: The conventional instrument that is used for coagulation of vessels on the retina during intraocular surgery, is a bipolar diathermy probe. Before the use of this bipolar instrument, a monopolar configuration was used for intraocular diathermy which was introduced in 1974 by Parel et al [8]. In their approach, a simple metallic tube which is insulated except from the tip, is connected to the handle of a radio frequency (RF) unit. Subsequently, the tip acts as a monopolar electrode which emits RF electromagnetic waves. These waves travel through the body medium as return path back to the diathermy unit, while diathermizing nearby vessels directly [8].

The design of the bipolar diathermy probe was established by Parel et al. in 1983 [1]. The probe consists of an active platinum inner electrode core with a glass coaxial insulation layer around it, which allows for an outer coaxial electrode layer, in this case the return electrode made of stainless steel. The pencil-shaped handle of this probe has a length of 100 mm and diameter of 7 mm. The 22-gauge (0.7 mm) probe tip has a length of 32 mm and, except for the distal end, has an extra surrounding layer of matt Teflon coating. At the distal end, the probe tip is conically shaped [2]. During diathermy, the produced current will flow from the emitting electrode towards the nearby located coaxial return electrode [1], which emits more directed RF waves. Currently, clinically used bipolar probes are still based on this bipolar configuration but can differ in material, tip design and reusability.

Fig. 2. Conventional diathermy probe (DORC, the Netherlands). Adapted from [9]

Figure 2 depicts a reusable diathermy probe. Next to reusable probes, disposable designs are also used clinically. The bipolar pencil of the company Kirwan Surgical Products [10] (depicted in Figure 3) is used in one of the described studies. It consists of a stainless steel wire which is insulated circumferentially and surrounded by an outer stainless steel conducting tube except from the distal end of the tip. Two energy connector terminals are located at the proximal end of the plastic exterior harness [11].

Fig. 3. Disposable bipolar pencil (Kirwan Surgical Products, US). Adapted from [10]

2) Intraocular Diathermy Forceps: The intraocular diathermy forceps are a disposable microforceps modified into a bipolar diathermy instrument. The configuration of a microforceps without diathermy function consists of a round plastic squeeze handle that actuates a 30 mm long, 23-gauge

(0.58 mm) thin metal shaft along a fixed inner gripping core, in order to close the gripping tip jaws which emerge at the distal end of the shaft, as can be in Figure 4 [12].

Fig. 4. Disposable micro forceps. Adapted from [12]

The diathermy function of the intraocular diathermy forceps can be established by separating the core of the microforceps into two longitudinal halves isolated from each other and isolated from the surrounding tube. A cross-section this configuration is depicted in Figure 5. Each half, including corresponding jaw, can act as an electrode. Within the handle of the diathermy forceps, the two separate electrodes are connected to electric wires. At the proximal end of the forceps, each wire is connected to an electric terminal forming a connector. On this connector, a diathermy apparatus can be placed which applies electric signal to the terminals of the connector. Consequently, when using an electric RF signal with the diathermy apparatus, current will flow from the emitting to the returning jaw [5]. The connector is the only exterior design feature that differs from the exterior design of the microforceps, as can be seen in Figure 6.

In this review, this configuration is denoted as type 1 diathermy forceps. Both jaws may be coated with a Teflon-like coating except for its distal end [13]. In this case, the instrument is denoted as insulated diathermy forceps.

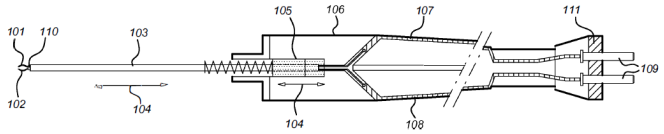

Fig. 5. Cross-section of intraocular diathermy forceps configuration. Adapted from [5]

Fig. 6. Exterior design of intraocular diathermy forceps. Figure provided by Van Overdam, amended from [14]

Another configuration is possible, where the inner core with both connected jaws is the emitting electrode and the outer tube serves as return electrode [3]. This configuration is denoted as type 2. In this review, the type 1 diathermy forceps is considered as default configuration if not indicated otherwise, because this configuration is used in subsequent technical [13] and clinical [6] studies.

3) Neurosurgical Bipolar Microforceps: The nickel-titanium alloy gripping elements of this forceps can be deformed elastically due to the elastic elongation property of this material [15]. As can be seen in Figure 7, near and inside the shaft, each of the two gripping elements is split into two limbs spaced from each other. The inner limb of each gripping element is surrounded by a highly temperature-resistant plastic guiding sleeve in which these limb can be moved along the axis. The outer limb of each gripping element is fixed beneath the coaxial outer shaft and the exposed region of the gripping element is elastically deformable. The gripping element will bend away from or towards the longitudinal axis when the inner limbs are pushed towards the tip or pulled away from the tip respectively along the axis. Each gripping element serves as an electrode, so this forceps can be used for coagulation. The inner limbs of each gripping element, which are guided through the guiding sleeve, reach to the other side of the instrument. Here, a first and second connector of an RF generator can be attached to each limb separately [16].

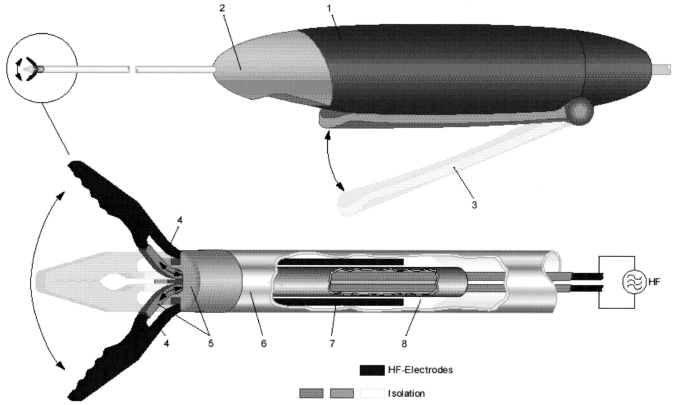

Fig. 7. Illustration of neurosurgical bipolar microforceps. Adapted from [15]

4) Bipolar Grasping Cautery Tool: Lutfallah et al. [17] attempted to developed a thin flexible bipolar cautery tool intended for minimally-invasive neurosurgery, which also serves as grasping forceps. The final design of this development consists of an actuation cable system and 3D printed plastic tips.

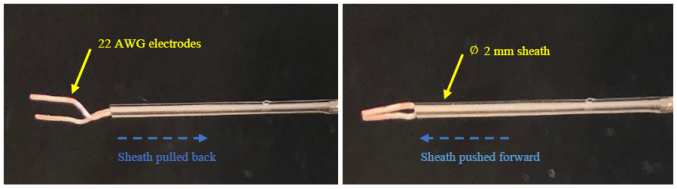

Fig. 8. Bipolar grasping forceps, wire prong design. Adapted from [18]

An earlier design version iteration is tested and reported by Lutfallah [18]. As can be seen in Figure 8, the basic principle of this version is similar to the diathermy forceps. The two solid-core 22 AWG wires, which are bend at the tips like prongs, can be closed by pushing the outer metal actuating

sheath with a diameter of 2 mm towards them. As the wires are insulated except the last 1 cm of the tips, one wire can serve as emitting electrode and one as return electrode. Due to the resemblance of this so called 'wire prong design' with the diathermy forceps, and the dissimilarities of the plastic actuated final design, only the wire prong version is considered in this review.

Electrical Engineering Aspect Analysis

This section contains the analysis of the following electrical engineering aspects: Diathermy Application, Effect of Current, Energy Requirement, Conduction, Thermal Effects and Insulation. Within each of these aspects, introductory theory related to diathermy is described and for each instrument the existing literature concerning the topic is provided.

A. Diathermy Application

In electrosurgery, a surgical effect is created by passing of RF alternating electrical current through tissue. The surgical effect of electrocoagulation, which is defined as "the tissue is heated below the boiling point and undergoes thermal denaturation" [19, Tab. 1], is used to achieve hemostasis, which is the control of bleeding of vessels. Following Joule's law of heating (described in subsection III-B) the resistance of the tissue to the passing electrical current leads to conversion of electrical energy to heat [19].

This heating effect was initially defined as diathermy in 1923 [20]. This term is still used nowadays, however, electrosurgery is often used as surgical term when describing coagulation [19]. As diathermy is generally used as term for coagulation during intraocular surgery, in this review the term diathermy is primarily used.

1) Intraocular Monopolar Diathermy Probe: In an animal study, Peyman et al. [21] evaluated the closure rate of intravitreal vessels of rabbits using a monopolar RF infusion probe (n=15). In fourteen rabbit eyes, immediate closure was seen. However, fluorescein angiography one week after intervention showed complete closure in only 53% (8/15) of the eyes. In order to evaluate these findings, the rabbits received a 15 mg injection of NH_4Cl in the vitreous cavity. Initially thirty rabbits were injected, however fifteen were selected by direct ophthalmoscopy on the absence of nasal temporal vessel damage and the absence of retinal tissue in one eye after four weeks [21].

2) Intraocular Bipolar Diathermy Probe: In an interventional case series, Van Overdam et al. [22] performed ligation of an important vessel prior to a surgical intervention in an attempt to reduce the risk of excessive bleeding. No instrumentation relevant to this review is tested here, but a consideration regarding bipolar diathermy is given in this study. The authors stated that if a diathermy instrument could completely shut engorged vessels, preventive ligation might be unnecessary. They concluded that as the existing bipolar diathermy probe can only coagulate vessels from one side, this instrument is not effective enough to substitute ligation of feeder vessels [22].

In a comparative animal cadaver study, Van Overdam et al. [3] compared the use of a conventional disposable diathermy probe (depicted in Figure 3) with the type 1 and type 2 intraocular diathermy forceps, on perfused porcine cadaver eyes ex-vivo with an open-sky approach (n=5). In this study, the closure rate (i.e. whether sufficient coagulation reaction is seen after first application) is evaluated, among other measurements. At the intraocular diathermy forceps, the current runs between the two jaws. Hence, vessels are expected to be coagulated more effectively from two sides [3].

As can be seen in Table I, results of the conventional diathermy probe showed closure rates of 60% (3/5) and 80% (4/5) at the inferior retinal artery and the inferior retinal vein, respectively [3]. Results of the diathermy forceps are described in subsubsection III-A3.

3) Intraocular Diathermy Forceps: Results of the type 1 diathermy forceps tests of the ex-vivo cadaver study of Van Overdam et al. [3], as described in the previous section, showed a closure rate of 100% (5/5) at both the artery and vein. The use of the type 2 diathermy forceps resulted in closure rates of 100% (5/5) and 80% (4/5) at the artery and the vein, respectively [3].

To test the diathermy performance of the intraocular diathermy forceps clinically, Van Overdam et al. [6] used this instrument for coagulation during in-vivo vitrectomy surgery for diabetic tractional retinal detachment (n=5). In all cases, haemorrhage could be stopped using the diathermy forceps and there were no post-operative complications [6]. Thus in this clinical study, the intraocular diathermy forceps had a closure rate of 100%.

4) Neurosurgical Bipolar Microforceps: Riegel et al. [15] tested the neurosurgical bipolar microforceps in a clinical study. At three illustrative cases, intraoperative coagulation with the bipolar microforceps was successful, leading to a closure rate of 100% depicted in Table I. In these cases, the patients received colloid cyst treatment, neuroendoscopic tumor resection and neuroendoscopic tumor cyst fenestration. In an additional fourth case, tumor biopsy was successfully performed with the bipolar microforceps. For this fourth case, no information regarding coagulation is provided by the authors [15].

5) Bipolar Grasping Cautery Tool: In the study of Lutfallah [18], the performance of the wire prong cautery forceps was tested by a qualitative cautery analysis. Here, a banana slice submerged in water was used as tissue simulation of brain tissue. The criteria for indication of successful cautery were a sizzling sound and visible darker spots at the surface when the electrically active tips would touch the tissue. In this analysis, all spots (n=6) indicated cautery, and the author concludes that the instrument functions as typical cautery tool in a less invasive approach [18].

B. Effect of Current

Following Joule's law of heating, depicted in Equation 1 [23, p. 256], the heat generated (Q) for tissue burn depends

on the resistance of the conductor (R), the current density (J) and the current duration (t).

$$Q = J^2 \times t \times R \tag{1}$$

Current density can be defined as "current per cross-sectional area" and has a squared dependency on the heat transformation. Hence in theory, smaller electrode surface area leads to more but localized heat. Therefore, while applying the same current value with a larger surface area, a longer application time is required in order to result in the same amount of heat. Applying higher currents while leaving the remaining variables constant, will result in more heat production [24].

Following Ohm's law in Equation 2 [25, p. 207], the current density (J) is equal to the electrical conductivity of the material (σ) times the electric field intensity (E).

$$J = \sigma E \tag{2}$$

The electric field intensity can be described by Equation 3 [25, p. 28-29], where q is the charge, ε is the permittivity of the material and r is the distance between the observation point and the charge.

$$E = \frac{q}{4\pi\varepsilon r^2} \tag{3}$$

1) Intraocular Monopolar Diathermy Probe: In a monopolar system, the human body serves as the return path. As can be seen in Figure 9 A, the monopolar probe does not direct the current towards a returning electrode, so a diffused energy beam spreads out from the tip. The current density is equal in the whole area of coagulation and this area is large. In this monopolar system, the most nearby tissue with the least conductive property will be coagulated [1].

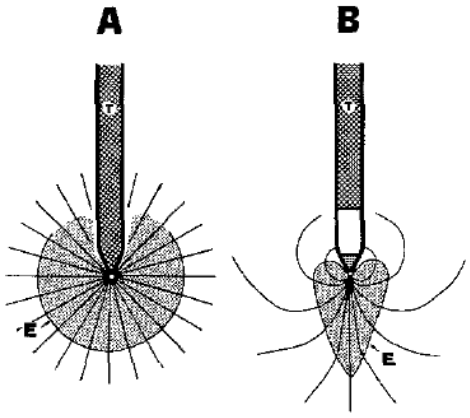

Fig. 9. Current lines and coagulation boundaries (E) of monopolar (A) and bipolar (B) probe. Adapted from [1]

2) Intraocular Bipolar Diathermy Probe: At a bipolar configuration, the distance between the emitting and returning electrode at the conical tip can be made smaller than with a monopolar configuration. This reduced path to ground ensures lower resistance of the current, which permits higher currents while using lower voltages. As depicted in Figure 9 B, the current is directed from the emitting tip electrode to the coaxial return electrode. The current density decreases further away from the tip and the energy is less diffused. Consequently, only desired nearby structures will be coagulated. The depth of the energy that is focused forwards, which actually leads to the coagulation, depends on the used frequency [26, 1].

3) Intraocular Diathermy Forceps: As the distance between the two jaw electrodes of the intraocular diathermy forceps is smaller than the distance between the axial tip and the sheet of the bipolar instrument, and the distance has a squared dependence on the energy decay following Equation 3, Riemens [13] argued that current density decreases even quicker around the jaws which results in an electric field that is more focused between the jaws. He also argues that an insulated version of the intraocular diathermy forceps (see Figure 13) has an even more focused electric field because of the short length of the electrode plate. As depicted in Figure 10 the electric field lines are only directed between the small portions of the jaws that are not insulated [13].

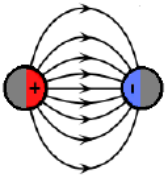

Fig. 10. Electric field lines insulated intraocular diathermy forceps. Figure adapted from [13]

In an experimental safety analysis, Riemens tested the insulated and an uninsulated type 1 intraocular diathermy forceps and a conventional bipolar diathermy probe (DORC, the Netherlands) on porcine cadaver eyes ex-vivo (n=3). At the insulated diathermy forceps, next to the basic internal insulation, both jaws are insulated as well, except from the tips. During calibration of the diathermy instruments, the ratio between input current and output current is measured with an oscilloscope and a high-frequency current transformer. Riemens stated that if this ratio appears to be constant and therefore is independent of the power supplied, this ratio can be used to derive the output current from the measured input current through the cable [13].

These calibration experiments showed a linear relationship between current input and output with corresponding ratios of 0.9540 and 0.9494 for the insulated and the uninsulated diathermy forceps, respectively. Use of the conventional diathermy probe resulted in a linear ratio of 0.9658. The author stated that ratios lower that 1 indicate that through the instrument, a small amount of current must be lost. As the ratios remain constant, the author used these ratios and the input currents to predict the output current of the instruments during experiments in three different media at power settings of 10%, 20% and 30%. These experiments were conducted ex-vivo inside opened porcine cadaver eyes containing media consisting of intravenous fluid (IV) (NaCl 0.9%), Eftiar Decalin (DORC, the Netherlands) or Balanced Salt Solution (BSS) [13]. NaCl 0.9% is a common IV fluid which is used for fluid resuscitation [27]. Eftiar Decalin is a perfluorocarbon

liquid, which serves as a fluorinated tamponading agent [28]. BSS is a solution used during vitrectomy to maintain fluid volume inside the eye [29].

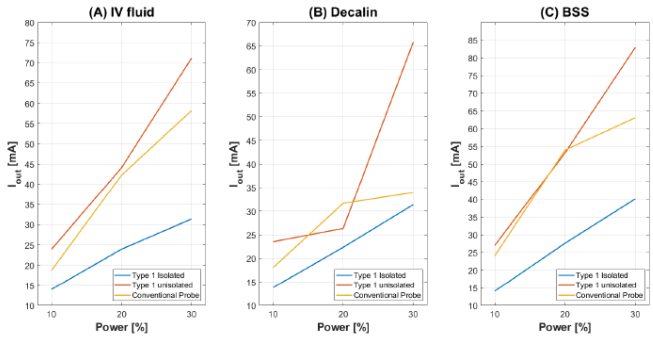

Fig. 11. Calculated output currents. Figure adapted from [13]

At each power setting and for all three media, the calculated output current of the insulated type 1 diathermy forceps appeared to be considerably lower than the uninsulated type 1 diathermy forceps and the conventional diathermy probe, as seen in Figure 11.

The author also observed the coagulation effect on the blood vessel and the presence of collateral damage on the retina during use of the diathermy instruments. Figure 12 displays the results of this observation.

	(A) IV Fluid			(B) Decalin			(C) BSS		
	Power			*Power*			*Power*		
	10%	*20%*	*30%*	*10%*	*20%*	*30%*	*10%*	*20%*	*30%*
Type 1 Isolated	– –	0	+	– –	0	+	– –	0	+
Type 1 Unisolated	– –	0	+	– –	0	++	– –	–	–
Conventional Probe	– –	+	++	– –	+	++	– –	0	+

Fig. 12. Coagulation effect on the blood vessel and the presence of collateral damage observed during use of diathermy instruments. "-- = no effect at all; – = almost no effect; 0 = normal (desired) coagulating effect; + = little collateral damage to the retina; ++ = way too much effect resulting in a damaged retina". Citation and figure adapted from [13, Fig. 4-1]

The author stated that it could be expected that lower output currents would result in too less coagulation effect. However according to Equation 6 which is described in upcoming subsection III-D, the electrode surface area and resistivity have an influence on the resistance. As the vessel clamped between the jaws of the insulated type 1 diathermy forceps leads to a high resistivity and the jaws have a small surface area due to the insulation of the jaws except their tips, the resistance is relatively high. Following Joule's law of heating Equation 1, in theory high resistance could compensate for low current. Hence, the author argued why it might be possible that lower current output could result in sufficient or even better coagulation while using the insulated type 1 diathermy forceps [13].

C. Energy Requirement

As mentioned in subsection III-A, electrical energy is converted to heat, which can result in the needed tissue denaturation but also unintended collateral damage. Next to the applied time, the heat (and thus tissue damage) depends on the resistance (R) and the current (I), which is equivalent to the output power (P) of the source, as depicted in Equation 4 [30, p. 446].

$$P = I^2 \times R \tag{4}$$

$$W = P \times t \tag{5}$$

The use of low power (P) and applied time (t), thus use of lower electrical energy (W) following Equation 5 [30, p. 440-441], could theoretically minimize collateral tissue damage.

Following early research which suggested that longer tissue contact results in more lateral heat [31], it is advised to use shorter application times with higher power in order to minimize collateral damage [19].

At electrosurgery, RF current can be applied by an electrosurgical unit (ESU). The frequency of the RF current can vary between 300 kHz and 5 MHz, depending on the desired surgical effect. Power sources with higher frequencies were also used in early experiments, as described in subsubsection III-C1 [32].

In the radio frequency spectrum, low-frequency ranges from 30 kHz to 300 kHz, medium-frequency ranges from 300 kHz to 3 MHz and high-frequency ranges from 3 MHz to 30MHz [33].

1) Intraocular Monopolar Diathermy Probe: In the preliminary animal study of Peyman et al. [21], described in subsubsection III-A1, a Cameron Miller diathermy unit was used to produce RF signal. At cases where no coagulum was formed on the tip, an energy level between 0.4 and 0.8 of the Cameron Miller diathermy unit and an application time of a few seconds was required in order to coagulate the intravitreal vessels. In cases where coagula adhered to the tip, this had to be removed. When not removed, higher energy levels were required [21].

For the clinical application of monopolar diathermy in the late seventies, a high-frequency 13 MHz short-wave diathermy power source, the MIRA (Midical Instrument Research Associates) unit, was used. During use of this high-frequency power source, leakage of electrical energy led to two cases in which the optic nerve was coagulated instead of bleeding vessels, resulting in the loss of light perception of the patients. As a consequence, the use of high-frequency monopolar diathermy was not recommended anymore [34].

2) Intraocular Bipolar Diathermy Probe: Next to a high-frequency system, a 0.1 MHz low-frequency configuration also appeared unfavourable for transvitreal diathermy. A low frequency system caused deep lesions and the high voltage requirement led to a sticky coagulum around the electrodes which tended to bond surrounding tissue to the electrodes [1, 35]. This phenomenon was also reported in an early study on intraocular coagulation [36]. As a compromise between high and low-frequency, the intraocular bipolar diathermy probe was initially powered with a 1.25 MHz medium-frequency shielded transistorized oscillator. The energy level

of this probe developed in the eighties can be adjusted from 0.1 tot 8.0 Joule (J) [2, 1].

Clinical trials evaluating the bipolar diathermy probe in 1983 show that low energy levels beneath 0.5 J are sufficient for small vessel coagulation without instrument contact [1]. In this study, direct probe contact and energy levels exceeding 0.5 J still led to bonding of tissue to the electrode tip. Hence, the authors recommended to be extremely careful during coagulation, especially near the optic nerve, and should begin with the lowest energy setting [1].

According to Van Overdam et al. [3], energy requirements are high in order to coagulate larger vessels properly with a bipolar diathermy probe, because the distal wall of the vessel is not in contact with the probe. The authors stated that these high energy levels could potentially lead to collateral damage. In their animal cadaver study (see description in subsubsection III-A2), the authors also evaluated the required energy and time needed for coagulation to investigate the energy requirements of a conventional bipolar diathermy probe [3]. In their experiment, a 450 kHz bipolar coagulator (Aesculap, Germany) with power steps of 0,1 Watt is used, with 1,5 Watt as starting power based on early findings of Parel et al. [1].

As can be seen in Table I, the tests with the conventional diathermy probe resulted in mean energy requirements of 2.1 J (standard deviation (SD)=0.8) and 2.4 J (SD=0.8) at the inferior retinal artery and the inferior retinal vein, respectively. The reported mean time needed was 1.4 seconds (SD=0.5) and 1.6 seconds (SD=0.5) at the artery and the vein, respectively [3]. Results of the diathermy forceps are described in subsubsection III-C3.

In the safety analysis described in subsubsection III-B3, the diathermy instruments are powered by an EVA eye surgical system (DORC, the Netherlands) with a frequency of 1 MHz. At 100% power, the system delivers 10 Watt. However, due to resistance in the cables of the test setup, the actual power decreases with a quadratic relationship. The application time was three seconds in all experiments of this safety analysis and the used power settings were 10%, 20% and 30% [13].

3) Intraocular Diathermy Forceps: To test if higher energy levels could be avoided using diathermy forceps instead of the bipolar probe, Van Overdam et al. [3] also measured the required energy and time needed for coagulation with use of the type 1 and type 2 diathermy forceps in their ex-vivo cadaver study (mentioned in subsubsection III-A2). Tests with the type 1 diathermy forceps resulted in mean energy requirements of 1.5 J (SD=0.0) and 1.5 J (SD=0.0) at the artery and the vein, respectively. Time needed for coagulation was 1.0 seconds (SD=0.0) and 1.0 seconds (SD=0.0) at the artery and the vein, respectively. The tests of the type 2 configuration resulted in mean energy requirements of 4.6 J (SD=3.3) and 5.4 J (SD=4.6) at the artery and the vein, respectively. Time needed for coagulation was 1.2 seconds (SD=0.8) and 1.4 seconds (SD=1.1) at the artery and the vein, respectively [3].

In the clinical study of Van Overdam et al. [6], described in subsubsection III-A3, the energy while using the diathermy forceps was not measured. However, the authors reported the indication that low energy levels were used as haemorrhage was effectively stopped and minimal collateral tissue coagulation was seen.

D. Conduction

As can be seen in Equation 6 [30, p. 279], the resistance (R) in an electrical system, depends on the length of the conductor (l), the surface area of the electrode (A) and the resistivity of tissue and fluid between electrodes (ρ).

$$R = \rho \frac{l}{A} \tag{6}$$

Resistance can also be defined as the lack of conductivity [37]. The electrical conductivity of a material is the ability to carry and conduct electrical current (which is the flow of electrons). The electrical conductivity is measured in Siemen per meter, whereas Siemen is equal to ohm^{-1} or 'mho' [38, 39].

The thermal conductivity of a material (κ) is the ability to conduct heat in watts per meter-kelvin (W/(m*K)). It can be derived from the Fourier law of heat conduction [40, 41]. In Equation 7 [40, p. 63], the ratio ΔQ/Δt is the heat flow rate, A is the surface area of the cross-section the conductor, Δt is the time, x is the distance between two temperature planes perpendicular to the surface area and ΔT is the temperature difference.

$$\kappa = \frac{\Delta Q}{A \Delta t} \frac{x}{\Delta T} \tag{7}$$

The thermal conductivity can be connected to the electrical conductivity (σ) by the Lorenz number (L) and the temperature (T) in the Wiedemann-Franz law, depicted in Equation 8 [42, p. 255].

$$\kappa = L \sigma T \tag{8}$$

As heat energy is spread out faster by highly conductive materials compared to tissue material with low conductive properties, high thermal and electrical conductivity of the surgical instrument could theoretically prevent overcoagulation [43].

Additionally, the conductivity of an insulating liquid can be influenced by several factors. The ionic concentration of the liquid could be altered by additives, metallic wear debris and other particles could contaminate the solution or lead to oxidation. As suggested by Abedian and Baker [44], the solution temperature also affects the electrical conductivity. In their work, they observed that sample temperature rises resulted in higher conductivity. They subsequently presented an empirical correlation between electrical conductivity and temperature of dielectric liquids [44].

1) Intraocular Monopolar Diathermy Probe: During monopolar diathermy the human body becomes the medium through which the current is conducted. Scar- and fatty tissue conduct less effective, so high-frequency diathermy could potentially damage surrounding tissue [1].

Parel et al. [1] reported that major changes in required energy levels of existing monopolar diathermy equipment were related to insufficient electrical conduction. The author argues that connection corrosion can occur due to "poor electrical

contacts within the handpiece microswitch, to the diathermy tip connection to the handpiece, or to the cable connections of the handpiece with the diathermy unit" [1, p. 33].

2) Intraocular Bipolar Diathermy Probe: To ensure continuous electrical conduction of the bipolar diathermy probe, Parel et al. [1] incorporated the probe and the cable in the instrument handle instead of using hand-switches. Experimental tests of various materials resulted in their choice for a platinum emitting electrode and a stainless steel return electrode. In these tests, a stainless steel emitting electrode disintegrated when exposed to high current density and an unsupported silver emitting electrode appeared to be malleable [1].

3) Intraocular Diathermy Forceps: In the study of Riemens [13] which is described in subsubsection III-B3, the cooling time of the intraocular fluid between the experiments with high energy requirements, was not sufficient for the fluid to reach room temperature at subsequent experiments. Following the observation that temperature rises result in higher conductivity of fluids, as described earlier this section, Riemens argues that the insufficient cooling time could have affected the conductivity of the media [13].

4) Neurosurgical Bipolar Microforceps: A nickel-titanium alloy is used for the gripping parts of the neurosurgical bipolar microforceps because of its elastic deformability of 10%. To provide continuous electrical conduction, the gripping members and limbs are one piece of this conductive material [16, 15]. The thermal conductivity of nickel-titanium (Nitinol) is 18 W/(m*K), which is lower than the thermal conductivity of stainless steel (29 W/(m*K)) [45].

5) Bipolar Grasping Cautery Tool: The conducting ability of the wire prong design of Lutfallah [18] was tested by performing power output tests. Here, average and maximum power outputs were measured from the electrosurgical unit (ESU). The average and maximum power was determined by the author from processed voltage waveforms which were obtained from a connected oscilloscope. With an average power of 21 Watt and a maximum power of 96 Watt at ESU setting 15/70, the maximum current output was calculated to be 1.4 Ampere. In order to conduct this current, a 28 AWG chassing wire should be used according to the author. This led to a safe choice of using 22 AWG copper wires in order to conduct at higher power settings [18].

The choice for copper wires was initially based on a comparison of the electrical conductivity property of this material ($5.85*10^7$ S/m [46]) with that of 304 Stainless Steel ($1.39*10^6$ S/m [47]) and Nitinol ($1*10^6$ S/m [48]) [18].

E. Thermal Effects

In theory, the thermal conductivity (κ) divided by the density ρ and the specific heat capacity (C_p) gives the thermal diffusivity (a) (Equation 9 [49, p. 127]).

$$a = \frac{\kappa}{\rho C_p} \tag{9}$$

Practically, thermal spread can be measured by histological analysis, thermography and thermistor resistance measuring. At histological test methods, thermal spread is inspected visually after application because thermal spread is considered as lateral damage spread. This is reflected as thermally-induced changes in cell and tissue morphology, spread away lateral from the actual burn location. To enhance this inspection, staining can be used [50].

At thermography, the distribution of surface temperature is used to inspect structural damage beneath the surface. Often this is done with an infrared camera which can measure surface temperature without direct contact [51]. It also can be performed real-time, however only during in situ surgery [52].

Dodde et al. [53] introduced another solution for real-time measuring thermal spread using thermistors placed on the electrosurgical instrument. Thermistors only depend on their own resistance, so no additional imaging or measurement instrumentation is needed. Hence, the authors argue that they also can provide real-time data during laparoscopic surgery [53]. The resistance of a thermistor changes when its temperature changes, so it is a temperature dependant resistance. The high change of resistance with temperature allows highly sensitive measurement [54, 55].

1) Intraocular Bipolar Diathermy Probe & Diathermy Forceps: In his study, Riemens [13] also mapped the heat dissipation on the surface of the fluid inside the opened porcine cadaver eyes during the diathermy experiments described in subsubsection III-B3. An infrared thermography camera (FLIR, U.S.) was used to see if the observed collateral damage depicted in Figure 12 could be related to heat dissipation. The author argued that the risk of collateral damage could be indicated by larger heat dissipation, as a greater energy spread could burn nearby tissue. Results showed that the heat was less dissipated at the insulated type 1 diathermy forceps, than the uninsulated diathermy forceps and the conventional bipolar probe. According to the author, this could mean that the energy is focused only on the target area and could be explained by the focused electrical field [13], as described in subsubsection III-B3.

The cooling time limitation of Riemens' study [13] mentioned in subsubsection III-D3, directly affected the measured temperature. Hence, the author suggested it could also have influenced the heat dissipation results.

F. Insulation

In order to provide a safe circuit that is directed at the region of interest and to prevent from burn, electrosurgical systems involve insulation [56]. The shaft and handle of diathermy instruments are insulated with isolation material. As heat transfer through the insulation layer must be prevented, the main property of insulation material is that it has a low thermal conductivity [57].

If there is a defect in the insulation layer, there is an insulation failure which can lead to electrosurgical burns, as there is an energy leak. Repeated use and insertion of instruments through trocar cannulas as well as sterilisation of reusable instruments can lead to insulation defects [58].

Capacitive coupling can also lead to insulation failure. This phenomenon can occur because alternating current is able

to transfer through insulation to adjacent conductive tissue, especially at monopolar systems. This could be avoided by using a limiting amount of voltage, short application time and proper insulation [59]. Additionally, Active Electrode Monitoring can also minimize this risk [58]. In bipolar cords there is no case of capacitive current as the currents are cancelled out because they flow in opposite directions [60].

1) Intraocular Bipolar Diathermy Probe: Parel et al. [2] indicated that before their introduction of the properly insulated bipolar probe, vitrectomy instruments were not designed with proper insulation around the shafts. They stated that this could have possibly led to complications like collateral tissue damage and external burns [2].

After performing material experiments for the development of the bipolar diathermy probe, glass was used as insulation material in between the central electrode and the coaxial return electrode. The use of Teflon and polyimide as inner insulation layer appeared to be fragile and led to fraying. This increased the surface of the inner electrode, which subsequently led to higher power requirements. However, black matt Teflon coating was suitable for outer insulation of the instrument from the medium and surrounding tissue [1].

2) Intraocular Diathermy Forceps: The insulation material of the intraocular diathermy forceps, which is used to insulate both core halves from each other and from the surrounding tube, can vary. The patent holder implies using electrically insulation adhesives like Araldite 2014-1 (Huntsman Advanced Materials), epoxy resins or other adhesives. He also mentions polyimide as possible insulation material, as it has tensile strength, chemical resistance and thermal stability. These properties make the material suitable for tubing of surgical instruments [5].

As described in subsubsection III-B3, an additional insulated version of the diathermy forceps is created. A Teflon-like insulation layer covers both jaws except from the contact points of the tips, as can be seen in Figure 13. This minimizes the surface area of the electrodes and prevents electric field lines in less direct paths [13].

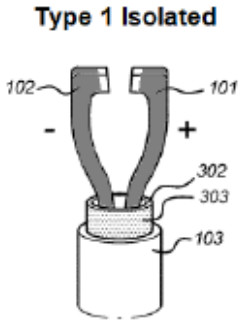

Fig. 13. Illustration of insulated version of the type 1 diathermy forceps. Adapted from [13]

3) Neurosurgical Bipolar Microforceps: Within the whole shaft of the neurosurgical bipolar microforceps [15], the two inner limbs are surrounded by polytetrafluoroethyle (Teflon) insulating tubes with a wall thickness of 50 μm. The authors mention that manufacturing of this insulation material may lead to technical problems and that 50 μm comes close to the maximum manufacturable thickness [15].

4) Bipolar Grasping Cautery Tool: The insulation material used around the electrode wires of the wire prong design is heat shrink (type 103-0801 Nordson Medical) [18].

IV. Discussion

A. Critical Evaluation of Electrical Engineering Aspects

In this section, the results within each electrical engineering aspect are evaluated and discussed.

1) Diathermy Application: In Table I, it can be seen that the type 1 intraocular diathermy forceps has a 100% closure rate at both the animal cadaver study [3] and the clinical trial [6]. It also exceeds the performance of the conventional diathermy probe, which shows closure rates of 60% and 80% in the cadaver study. These results indicate that the type 1 intraocular diathermy forceps performs as expected and that the performance of the conventional diathermy probe may be questioned. However, a sample size of five is considerably small in order to prove the significance of this indication. Hence, a larger quantitative clinical study should be performed, which is also suggested by the authors themselves [6].

Because the insulated type of diathermy forceps is only tested in porcine cadaver eye study with an open-sky approach, clinical closure rate results of this instrument are absent. Additionally, the closure rates of this cadaver study are qualitative because the coagulation is observed and rated by amount of effect. Hence, this instrument should be included in a large quantitative clinical study.

Although the neurosurgical bipolar microforceps also shows a closure rate of 100% in the clinical study described by [15], the three operations that were performed and the vessel types that were coagulated were different. Therefore, to prove high closure rate, this instrument should also undergo additional clinical trials with a larger sample size and at similar operations.

It is difficult to compare the performance of the neurosurgical bipolar microforceps with intraocular diathermy instruments, as the dimensions are larger and the internal environment of the brain differs from the internal environment of the eye. There might be studies which evaluate (dis)similarities of cerebrospinal fluid and vitreous humour, as well as comparisons of brain- and eye tissue and vessels. In order to conclude whether electrical engineering aspects of instruments used in these two surgical areas could be combined or compared quantitatively, it might be useful to investigate these studies.

During the experiments conducted by Riemens [13], described in subsubsection III-B3, the vitreous humour was not fully removed from the porcine cadaver eyes and led to sticking of this substance to the diathermy instruments. Clearing of these instruments became more difficult, which could have affected the performance of the instruments [13]. Ideally the safety analysis of Riemens should be repeated at which the vitreous humour should be removed thoroughly.

As described in subsubsection III-A5, the criteria which the author of the wire prong cautery tool used for indication of

TABLE I
APPLICATION TISSUE, SAMPLE SIZE, CLOSURE RATE, MEAN AND STANDARD DEVIATION OF REQUIRED ENERGY AND TIME OF EXPERIMENTS CONDUCTED WITH REVIEWED DIATHERMY INSTRUMENTS

Study	Application [tissue]	n [#]	Closure rate [%]	Energy [J]	Time [s]
Monopolar Diathermy Probe					
Peyman et al. [21]	In vivo rabbit intravitreal vessel	15	53	N/A	N/A
Bipolar Diathermy Probe					
Van Overdam et al. [3]	Ex vivo porcine inferior retinal artery	5	60	2.1±0.8	1.4±0.5
	Ex vivo porcine inferior retinal vein	5	80	2.4±0.8	1.6±0.5
Intraocular Diathermy Forceps Type 1					
Van Overdam et al. [3]	Ex vivo porcine inferior retinal artery	5	100	1.5±0.0	1.0±0.0
	Ex vivo porcine inferior retinal vein	5	100	1.5±0.0	1.0±0.0
Van Overdam et al. [6]	In vivo human retinal blood vessel	5	100	N/A	N/A
Intraocular Diathermy Forceps Type 2					
Van Overdam et al. [3]	Ex vivo porcine inferior retinal artery	5	100	4.6±3.3	1.2±0.8
	Ex vivo porcine inferior retinal vein	5	80	5.4±4.6	1.4±1.1
Neurosurgical Bipolar Microforceps					
Riegel et al. [15]	In vivo cerebral vessels and cyst membrane vessels	3	100	N/A	N/A

successful cautery, were sizzling sounds and visible darker spots detectable on a watered banana slice [18]. These qualitative criteria may lead to subjective results and resemblance of the tissue simulation method to real brain tissue could be questioned. Additionally, the qualitative cautery performance results are not comparable with the diathermy performance of the other instruments. Hence, when adapting electrical engineering aspects of this development, its reliability should be questioned.

The comparison of instrument performance appears to be difficult. To enhance this in future studies, as well as performance evaluation of a redesign of the intraocular diathermy forceps, diathermy application sites and test conditions should be kept similar as much as possible.

2) Effect of Current: From the results of Riemens analysis described in subsubsection III-B3, it appears that the bipolar diathermy probe tends to overcoagulate resulting into little or even major collateral damage even though the surface area is designed to be considerably small. The insulated type 1 diathermy forceps operates with lower output currents while performing as desired. The explanations for this output current values given by the author sound plausible, as the isolation theoretically provides high resistance and an even more focused electrical field than the uninsulated diathermy forceps. Evidence for these explanations could result from a clinical study, as Riemens analysis is the only study to date which tested the insulated version of the intraocular diathermy forceps.

If the output current cannot be measured directly, an alternative methodology is required. In the case of Riemens analysis, an additional hypothesis must first be proven true. This involved extra test setup components like an oscilloscope and a high-frequency current transformer which consequently could lead to additional current loss or noise in the results [13]. These factors should be considered when creating an alternative test methodology and its feasibility at an actual clinical study should be of importance.

3) Energy Requirement: In early research, when the monopolar diathermy probe was tested and used, exact energy levels were not measured. Only the frequency and indicative power levels of the diathermy unit are mentioned, which cannot be compared with the energy requirement results of currently tested diathermy instruments.

It is more difficult to quantitatively measure energy requirements when testing diathermy instruments, as the moment of successful coagulation, at which the application time is based, is qualitatively determined by the person who applies diathermy.

Quantitative energy measurements can be compared easily. From Table I it is clear that the type 1 diathermy forceps has the lowest energy requirement and the shortest application time. It again complies to the expectation of the authors, which is that the high energy levels needed at bipolar diathermy could be avoided using the diathermy forceps instead. An alternative configuration like in the type 2 diathermy forceps, can lead to major increases of energy levels, in this case up to 5.4 J (SD=4.6).

When applying the quadratic relationship mentioned in subsubsection III-C2, corresponding output power at the three used power settings (10%, 20% and 30%) would ideally be 0.1 Watt, 0.4 Watt and 0.9 Watt, respectively. Applying Equation 5 would theoretically lead to required energies of 0.3 J, 1.2 J and 2.7 J when applying the instruments for three seconds. From Figure 12, is appears that 20% power only results in a normal desired coagulating effect. Hence in this study, a power setting of 0.4 Watt, application time of 3 seconds, and an energy requirement of 1.2 J appears to be ideal. This energy requirement is even lower than the least energy value in Table I, but this is possible as the application time of 3 seconds is approximately two or three times larger than all evaluated instruments. Because it is advised to use shorter application times with higher power [19], 3 seconds of diathermy application might not be favourable during clinical operations. Thus, this study is lacking an optimal energy requirement evaluation. This adds up to the need for a clinical study as mentioned at subsubsection IV-A2.

The electrode configuration of the diathermy forceps has a high influence on the energy requirement. Energy depends

on power, which relies on the current and the resistance. The current depends on the current density and the area. As described in subsection III-B, the distance between the active and permitting electrode has a squared dependency on the current density. The current density also has a squared dependency on the generated heat. Taking these arguments into account, the type 2 configuration might lead to high energy requirements due to the higher distance between the jaws and the core. This also could be the explanation on why the type 1 diathermy forceps has lower energy and application time requirements than the bipolar probe. Following this argument and literature described earlier, in a redesign of the diathermy forceps the electrode configuration should also be designed with the lowest electrode distance possible. At the type 1 configuration, this is equal to the distance between the jaws and relies on the thickness and stiffness of the vessel which is clamped between it during diathermy. It could be interesting to evaluate if an extra clamping force on the jaws could lead to more compressed vessels. In this case, the distance between the jaws decreases which could lead to lower resistance and consequently lower energy requirement.

4) Conduction: For the early development of diathermy, the challenge was to provide continuous electrical conduction. This problem was solved in the bipolar probe as it only consists of the conducting electrodes inside the handle and the conducting material was selected after experimental tests.

At the intraocular diathermy forceps, this electrode system must be combined with an actuation system inside the handle. Consequently, the continuity of electrical conduction might be a point of attention, as this system could be fragile or sensitive to fatigue.

If the intraocular diathermy forceps were to be redesigned, material selection process should include good thermal and electrical conductivity properties as selection criteria. It also could involve tests equivalent to the conduction ability experiment of the wire prong design of Lutfallah [18]. This experiment also served for determination of the diameter of the copper wires. As the intraocular diathermy forceps is a more complex instrument which not exclusively consist of metal wires through a shaft, this particular experiment setup should be modified for instrument with smaller dimensions.

Copper or copper alloys, with high thermal and electrical conductivity, could theoretically reduce the amount of sticky tissue on electrodes of electrosurgical instruments [61, 62, 63]. However, the use of copper is not considered for electrosurgical instruments as it is not biocompatible. Nickel is a biocompatible material with a higher thermal conductivity than stainless steel, which also could minimize tissue sticking [64]. A nickel titanium alloy is used in the elastically deformable system of the neurosurgical bipolar microforceps. This alloy has a lower electrical and thermal conductivity than stainless steel. As a lower conductivity of the instrument material could theoretically increase the risk of overcoagulation as described in subsection III-D, the lower conductivity should be considered when choosing for this material.

If the deformable actuation system of the neurosurgical bipolar microforceps would be adapted in the redesign of the intraocular diathermy forceps, its guiding sleeve actuation system must be manufactured such that it fits inside the metal shaft of 0.6 mm. As this does not seem feasible, the selection of Nitinol or Nickel for the intraocular diathermy forceps as conductive material is not a logic choice.

As a consequence of the insufficient cooling time in between experiments of Riemens' experiments [13], the heat will be conducted through the media more easily and this could result in higher temperature values at the surface of the media. Following Equation 7, the temperature difference between the diathermy application on the retina and the surface temperature of the media will in this case be smaller, thus more accurate. However, as the temperature of the medium itself is higher before applying diathermy, the temperature results after diathermy consequently are higher. This direct influence on the measured temperature leads to less accurate results. The latter two arguments lead to contradictory accuracy of results, which indicates that the cooling down and the conductivity of the medium are interesting challenges to investigate. Especially as this challenge occurs during clinical use. This is because the diathermy application recurrence might increase at major haemorrhages and there might not be any time for cooling down of the surrounding fluid.

This varying recurrence of use during surgical operations also leads to a design criterion which ensures safe use at all extremities. Hence, it might be useful to test the cooling results and conductivity of the fluid at varying and extreme repeated use. This way one could determine if there could be a relationship between these cooling results, the conductivity of the fluid medium and the potential influence on energy requirement or collateral tissue damage. The tissue damage could also be evaluated by means of thermal spread as mentioned in subsection III-E.

When comparing the intraocular instruments with the neurosurgical instruments, the different conductivity properties of the surrounding tissue and fluid could be considered as well, in case that the conductivity of environment considerably affects the energy requirement and tissue damage.

5) Thermal Effects: The accuracy of histological analyses can be questioned as permanent damage is also dependent on the application time next to the exposure temperature itself [52]. Hence, with histological analysis, the spread detected could be less due to shorter application times while the initial area of heat actually was high. Vice versa, application time is directly related to the produced heating inside the tissue [24], so one could argue that the heat detected by thermography already includes the application time.

At ex vivo studies and in situ surgeries there are more possibilities for examination of thermal effect, because a thermography camera can be placed above the surface and there is enough open space for other temperature measuring equipment. This also applies to the heat dissipation experiments of Riemens [13], described in subsubsection III-E1. The downside of this open-sky thermography method, is that only the surface temperature of the fluid layer on top of the retina is measured. So, the exact local temperature of the coagulation site or the instrument inside the medium cannot be known. Another drawback of this method is that the depth of the fluid layer is not equal because the round shape of the eye is

remained. This leads to influenced temperature results because at locations where the distance between the application site and the liquid surface is higher, the fluid is cooler at the surface. This can be explained by Equation 7. Because the temperature difference depends on the distance between two temperature planes divided by the thermal conductivity, a higher distance leads to a higher temperature difference.

It might be interesting to eventually measure temperature and thermal spread in a clinical trial. At intraocular surgery, the diathermy instrument must fit through trocar cannulas of 23 gauge which are placed through the eyeball. This means a potential measurement module should be smaller than 0.6 mm in order to fit through the trocars as well. Micro thermistors with a diameter of 0.3 mm are available [65], but it might be difficult to place such a thermistor on a diathermy probe or forceps. Additionally, it should be questioned whether the use of such a thermistor should be biocompatible and suited for intraocular use. If a separate measuring instrument solely containing a micro thermistor would meet the latter mentioned requirements, such a tool might be inserted through an adjacent cannula next to the diathermy instrument. In this setup, the thermistor could be located near the site of coagulation which could allow for internal measurements. However, the exact location of the thermistor relatively to the coagulation site might not be known or be controlled and the feasibility of such a test setup should be considered.

6) Insulation: For the early developments of monopolar intraocular diathermy systems, proper insulation and the risk of capacitive coupling were apparent challenges. Although there is no risk of capacitive coupling at bipolar systems, insulation material tests are important to evaluate other unwanted effects such as fraying. It appears that polytetrafluoroethylen (Teflon) is a suitable biocompatible external insulation material, but not for internal insulation.

The dimensions of (internal) components of intraocular instruments are limited, so the thickness of insulation layers is of importance. Manufacturing of thin insulation layers on micro scale appears to be a challenge. Hence, it is space-saving to add a fixation property to an internal insulation layer, like the insulation adhesives suggested for the intraocular diathermy forceps [5]. The choice for this particular adhesive material as well as other insulation materials varies widely and the biocompatibility of the insulation material which is in contact with human tissue should be considered as well.

The choice for heat shrink tubing is plausible at a preliminary design concepts like the wire prong design. Polyethylene terephthalate shrink tubing is available with a diameter of 0.006–0.020 inch (0.15-0.51 mm) and a wall thickness of 0.0001–0.0005 inch (0.0025-0.013 mm) [66]. Although these dimensions are considerably small, the application of heat shrink wires at the intraocular diathermy forceps does not appear feasible, as is described in subsubsection IV-A4. Except when rigorous changes in its design would be carried out, heat shrink as internal insulation material could possibly be investigated.

At disposable instruments, external insulation layers are less sensitive to failures caused by repeated use. If a reusable version of the diathermy forceps would be considered, it might be useful to evaluate the cleanability of this insulation layer in order to prevent insulation failures. Hereby, (internal) corrosion and the risk of material desorption or wear debris should be evaluated.

B. Future Recommendations

This review is focused on different electrical engineering aspects of the intraocular diathermy forceps design. Consequently, suggestions provided in the critical evaluation of all aspects could be considered for future optimization of this instrument or to contribute to science and validation of intraocular instruments. In order for the current intraocular diathermy forceps design to be introduced to the clinical market and to enhance optimization of this instrument, future studies described in this section are recommended.

The critical evaluation of various electrical engineering aspects indicate that additional quantitative clinical studies are needed in order to confirm the apparent benefits of the intraocular diathermy forceps. Additionally, the insulated type should be tested clinically on its safe use and closure rate, and should subsequently be included in the broader additional quantitative clinical study. This ideally should be done by means of a large sample size at which energy requirement and local (instrument) heating is measured.

If it appears unfeasible to include all these measurements in a clinical study, an additional animal cadaver study for the remaining measurements could be conducted at which operative variables are kept closest to surgical reality as possible. This should include thoroughly removing vitreous humour.

In case that it would be difficult to measure energy requirement in a clinical study directly, an alternative test methodology could be considered at which the required energy could be calculated. If this appears to be impossible, the output current could be calculated in the same fashion, which indirectly says something about the energy requirement.

From an engineering approach, an experimental validation method could be designed to proof superiority of the diathermy forceps. Thermal spread measurement can be optimized by addressing the found challenges concerning cooling time, the difference between fluid surface temperature and actual retinal temperature as well as the influence of unequal fluid depth. With this new validation method, the correlation between liquid conductivity and retinal thermal spread could give insight in the safe use of diathermy instruments.

There are no design flaws of the intraocular diathermy forceps indicated by this review. It appears that the insulation layer on the jaws of the insulated intraocular diathermy forceps works even better than the initial design of the instrument [13]. However, to optimize the performance of this version in a future project, the application process and design of the insulation layer could be analysed.

C. Limitations

In this section, the limitations of reviewed articles and the limitation of this review itself is described. At various

electrical engineering aspects, information of different instruments is lacking. Particular measurements are not carried out and (material) design choices are not always provided by developers.

As the focus of this review is on electrical aspects, other design aspects including ergonomics, ease of use and manufacturing (costs) are left aside.

Evaluation of thermal effect at the neurosurgical instruments is absent. Additionally, heat measurements are not included yet in clinical studies. Therefore, thermal results of the safety analysis of Riemens [13] could not be compared with other studies.

In Table I, for the bipolar diathermy probe, only the comparative study with the diathermy forceps is included. This review lacks results from an experiment conducted with different types of bipolar diathermy probes, although it is likely that such an experiment has been performed.

By applying the inclusion criterion '*the article describes a surgical instrument (development) containing a peeling function as well as a bipolar diathermy function*', articles containing other intraocular diathermy combinations, like a scissors-diathermy combination suggested by Van Overdam [5] or a 'fiberoptic diathermy tissue manipulator' [67, p. 803] are filtered out. Analysis of these diathermy combinations could potentially provide additional challenges and optimization input for the design of the intraocular diathermy forceps.

Despite being of academic value, it should be mentioned that the data and information described in the animal cadaver study of Riemens [13], is not published. Nevertheless, the study results and arguments are interesting to consider when designing such instruments and are therefore included in this review.

It should be reminded that the wire prong design of Lutfallah [18] is a preliminary version of the final design of the developer. The author did publish an article on the final version in proceeding with co-workers [17]. As certain aspects of this final design might still be usefull, the exclusion of this instrument (based on subjective exclusion criteria) could be a limitation of this review.

Although the project of is not published, the results of the preliminary wire prong design could be considered academically valuable as it concerns a master thesis project. However, because this design is not developed any further, and clinical or animal studies are lacking, its results are mainly projected on the design (challenges) of the intraocular diathermy forceps. This could lead to the consideration of unreliable material- and design choices when not criticized thoroughly.

Overall, this review includes statements and arguments provided by authors of included studies. These may be subjective and should also be viewed with a critical eye. Suggestions provided in the critical evaluation and future recommendations of this review, based on these suggestions and arguments, may therefore be biased. Additionally, it should be noted that the information for this review is selected by subjective inclusion criteria and the results are not compared systematically but reviewed with a narrative approach.

It would take a high amount of time and effort to perform all additional studies provided by this review. Selection of these studies in the future would depend on the approach and goal of the researcher concerned.

V. Conclusion

The aim of this literature review was to identify electrical engineering challenges in designing the intraocular diathermy forceps. From the evaluation of the analyzed electrical engineering aspects, the following key challenges are identified. A larger quantitative clinical study including the insulated and uninsulated type of the intraocular diathermy forceps should be performed in order to prove the indication of its superior diathermy performance, lower output currents and lower energy requirements. Unequal cooling times in between thermal validation experiments can influence the conduction of the surrounding fluid, but this is a realistic challenge as the frequency of instrument use varies during surgeries. The main challenge in using thermal spread measurement as an indication of safe diathermy use is that the open-sky thermography method measures surface temperature of the covering fluid instead of the actual temperature at the diathermy application site on the retina. Additionally, the unequal depth of the covering fluid layer leads to varying temperature differences between the measured surface temperature and the actual retinal temperature. Addressing the three latter challenges could result in a new experimental validation method at which a relationship between the conductivity of the fluid and the actual thermal spread on the retina can potentially be found. As the dimensions of (internal) components of intraocular instruments are limited, the choice for internal insulation of the intraocular diathermy forceps remains a challenge but is solvable by adding a fixation property to the internal insulation layer.

The evaluation of existing literature with the found challenges as result, gives insight into the question whether the current use of intraocular diathermy could be improved by using the intraocular diathermy forceps. Addressing all these challenges could lead to the introduction of the intraocular diathermy forceps because the results indeed suggest that this instrument is beneficial. The proposed future (re)design of experimental methods could contribute to this and to the general validation of intraocular diathermy instruments.

REFERENCES

[1] Jean-Marie Parel, Robert Machemer, Guy E. O'Grady, Gerard W. Crock, and Izuru Nose. Intraocular diathermy coagulation. *Graefe's Archive for Clinical and Experimental Ophthalmology*, 221(1):31–34, Aug 1983. ISSN 1435-702X. doi: 10.1007/BF02171728.

[2] Jean-Marie Parel, Guy E. O'Grady, and Robert Machemer. A Bipolar Coaxial Microprobe for Safe Transvitreal Diathermy. *Archives of Ophthalmology*, 99(3):494–497, Mar 1981. ISSN 0003-9950. doi: 10.1001/archopht.1981.03930010496024.

[3] Koen A. van Overdam, Emine Kilic, Robert M. Verdijk, and Sonia Manning. Intra-ocular diathermy forceps. *Acta Ophthalmologica*, 96(4):420–422, Jun 2018. ISSN 1755375X. doi: 10.1111/aos.13619.

[4] Jean-Baptiste Ducloyer, Juliette Ivan, Alexandra Poinas, Olivier Lebreton, Alexandre Bonissent, Paul Fossum, Christelle Volteau, Ramin Tadayoni, Catherine Creuzot-Garchet, Yannick Le Mer, Julien Perol, June Fortin, Anne Chiffoleau, Fanny Billaud, Catherine Ivan, and Michel Weber. Does internal limiting membrane peeling during epiretinal membrane surgery induce microscotomas on microperimetry? Study protocol for PEELING, a randomized controlled clinical trial. *Trials*, 21(1):500, Jun 2020. ISSN 1745-6215. doi: 10.1186/s13063-020-04433-9.

[5] Koen-Willem Adriaan van Overdam, Jun 2017. WO Patent 2017/102975 A1.

[6] Koen Overdam, Jerrel Pawiroredjo, Dinesh Jiawan, and Sonia Manning. First-in-human study of the safety, effectiveness and ease of use of the intra-ocular diathermy forceps during vitrectomy. *Acta Ophthalmologica*, 97(8), Dec 2019. ISSN 1755-375X, 1755-3768. doi: 10.1111/aos.14134. URL https://onlinelibrary.wiley.com/doi/abs/10.1111/aos.14134.

[7] Amir Samii and Manuel Dujovny. Kirwan® "non-stick" bipolar forceps. *Surgical Neurology*, 45(3):297–298, Mar 1996. ISSN 0090-3019. doi: 10.1016/0090-3019(95)00414-9.

[8] J. M. Parel, R. Machemer, and W. Aumayr. A new concept for vitreous surgery. 4. Improvements in instrumentation and illumination. *American Journal of Ophthalmology*, 77(1):6–12, Jan 1974. ISSN 0002-9394.

[9] DORC. Endo-diathermy handle, straight pointed tip. (23 gauge / 0.6 mm). URL https://dorcglobal.com/product/endo-diathermy-handle-straight-pointed-tip-23-gauge-06-mm. Accessed: Apr. 14, 2021.

[10] Kirwan Surgical Products. BIPOLAR PENCILS. URL http://www.ksp.com/product/bipolar-pencils. Accessed: April. 29, 2021.

[11] Lawrence T. Kirwan Jr. Disposable bipolar coagulator, Feb 1992. URL https://patents.google.com/patent/US5089002A/en?oq=+5%2c089%2c002%2c. US Patent 5,089,002 A.

[12] Vitreq. Improved Intraocular Surgical Control and Precision in Surgical Maneuvers, 2020. URL https://www.vitreq.com/uploads/MAR.BR001-1574288-01_US_BVI_Vitreq_Micro_Forceps_and_Scissors.pdf. Accessed: Mar. 30, 2021.

[13] Boyd Riemens. Safety of Intraocular Diathermy Forceps, Dec 2020. Internship Report Delft University of Technology.

[14] Vitreq. MICRO FORCEPS & SCISSORS, 2020. URL https://www.vitreq.com/uploads/MAR.BR001-Vitreq_BVI_Brochure_Micro_Forceps_Scissors_JUN2020-V04.pdf.

[15] Thomas Riegel, Dirk Freudenstein, Olaf Alberti, Frank Duffner, Dieter Hellwig, Volker Bartel, and Helmut Bertalanffy. Novel multipurpose bipolar instrument for endoscopic neurosurgery. *Neurosurgery*, 51(1):270–274, Jul 2002. ISSN 0148-396X. doi: 10.1097/00006123-200207000-00046.

[16] Volker Bartel. Surgical instrument for minimally invasive surgery, Oct 2002. URL https://patents.google.com/patent/US6464703B2/en?q=forceps&inventor=Volker+Bartel&patents=false&oq=Volker+Bartel+forceps. US Patent 6,464,703 B2.

[17] Claudia Lutfallah, Thomas Looi, and James Drake. A novel bipolar cautery tool for minimally-invasive neuroendoscopic procedures. In *2020 42nd Annual International Conference of the IEEE Engineering in Medicine & Biology Society (EMBC)*, page 6062–6065. IEEE, Jul 2020. ISBN 978-1-72811-990-8. doi: 10.1109/EMBC44109.2020.9176415. URL https://ieeexplore.ieee.org/document/9176415/.

[18] Claudia Lutfallah. 2 mm Bipolar Cautery Instrument for Robot-Assisted Neuroendoscopy, Nov 2020. URL http://hdl.handle.net/1807/103692. Master Thesis University of Toronto.

[19] Arash Taheri, Parisa Mansoori, Laura F. Sandoval, Steven R. Feldman, Daniel Pearce, and Phillip M. Williford. Electrosurgery: Part I. Basics and principles. *Journal of the American Academy of Dermatology*, 70 (4):591.e1–591.e14, Apr 2014. ISSN 0190-9622. doi: 10.1016/j.jaad.2013.09.056.

[20] W. J. Turrell. Treatment by Diathermy. *Br Med J*, 1 (3239):143–145, Jan 1923. ISSN 0007-1447, 1468-5833. doi: 10.1136/bmj.1.3239.143.

[21] Gholam Peyman, Jeff Koziol, Donald Sanders, and Joseph Vlchek. Studies on Intravitreal Blood Vessels. III. Effectiveness of Intraocular Diathermy on Blood Vessel Closure; a Comparison with Argon Laser. *Investigative ophthalmology*, 13:369–76, Jun 1974.

[22] Koen A. van Overdam, Tom Missotten, Emine Kilic, and Leigh H. Spielberg. Early surgical treatment of retinal hemangioblastomas. *Acta Ophthalmologica*, 95(1):97–102, 2017. ISSN 1755-3768. doi: 10.1111/aos.13223.

[23] Nicolas Aigner, Christian Fialka, Angelika Fritz, Otto Wruhs, and Gerald Zöch. Complications in the use of diathermy. *Burns*, 23(3):256–264, 1997. ISSN 0305-4179.

[24] Nader N. Massarweh, N. Cosgriff, and D. Slakey. Electrosurgery: history, principles, and current and future uses. *Journal of the American College of Surgeons*, 2006.

doi: 10.1016/J.JAMCOLLSURG.2005.11.017.

[25] Fawwaz T. Ulaby, Eric Michielssen, and Umberto Ravaioli. *Fundamentals of applied electromagnetics*. Pearson Education, 6th internat. edition, 2010. ISBN 978-0-13-255008-6.

[26] George W. Tate, William L. Hutton, Albert Vaiser, and William B. Snyder. A coaxial electrode for intraocular diathermy. *American Journal of Ophthalmology*, 79(4): 691–693, Apr 1975. ISSN 0002-9394. doi: 10.1016/0002-9394(75)90813-2.

[27] Fei-Hu Zhou, Chao Liu, Zhi Mao, and Peng-Lin Ma. Normal saline for intravenous fluid therapy in critically ill patients. 21:11–15, Feb 2018. ISSN 1008-1275. doi: 10.1016/j.cjtee.2017.04.012.

[28] Ashish Markan, Aman Kumar, Jayesh Vira, Vishali Gupta, and Aniruddha Agarwal. Advances in the tools and techniques of vitreoretinal surgery. *Expert Review of Ophthalmology*, 15(6):331–345, Nov 2020. ISSN 1746-9899. doi: 10.1080/17469899.2020.1810018.

[29] Thomas H. Williamson. *Intraocular Surgery: A Basic Surgical Guide*. Springer International Publishing, 2016. ISBN 978-3-319-27988-6. doi: 10.1007/978-3-319-27990-9. URL https://www.springer.com/gp/book/9783319279886.

[30] Narinder Kumar. *Comprehensive Physics XII*. Laxmi Publications, 2004. ISBN 978-81-7008-592-8. Google-Books-ID: yGjmnAAACAAJ.

[31] Kenneth L Kalkwarf, Robert F Krejci, and Allen R Edison. A method to measure operating variables in electrosurgery. *Journal of Prosthetic Dentistry*, 42(5): 566–570, 1979.

[32] John Pearce. *Electrosurgical Unit (ESU)*. American Cancer Society, 2006. ISBN 978-0-471-73287-7. doi: 10.1002/0471732877.emd103. URL https://onlinelibrary.wiley.com/doi/abs/10.1002/0471732877.emd103.

[33] Mark Holker. *27 - Radiowave propagation*, page 27–1. Butterworth-Heinemann, Jan 1993. ISBN 978-0-7506-1162-6. doi: 10.1016/B978-0-7506-1162-6.50033-2. URL https://www.sciencedirect.com/science/article/pii/B9780750611626500332.

[34] Robert Machemer. Letter to the editor. *American journal of ophthalmology*, 83:282, 1977.

[35] GA Peyman and D Sanders. Intraocular diathermy. In Irvine A and O'Malley C, editors, *Advances in vitreous surgery*, page 436–447. Charles C. Thomas, 1976.

[36] GA Peyman and NA Dodich. Experimental intraocular coagulation. *Ophthalmol. Surg*, 3:32, 1972.

[37] Covidien. Principles of Electrosurgery, 2008. URL https://www.asit.org/assets/documents/Prinicpals_in_electrosurgery.pdf. Accessed: Apr. 29, 2021.

[38] David M. Gray. *Conductivity-Electric*, page 429–433. American Cancer Society, 2005. ISBN 978-0-471-47844-7. doi: 10.1002/047147844X.pc146. URL https://onlinelibrary.wiley.com/doi/abs/10.1002/047147844X.pc146.

[39] Ronald Miller, Wesley Bradford, and Normand Peters. *Specific Conductance: Theoretical Considerations and Application to Analytical Quality Control*. Jan 1986. doi: 10.13140/RG.2.1.4766.9609.

[40] D. Ratna. *3 - Thermal properties of thermosets*, page 62–91. Woodhead Publishing, Jan 2012. ISBN 978-0-85709-086-7. doi: 10.1533/9780857097637.1.62. URL https://www.sciencedirect.com/science/article/pii/B9780857090867500031.

[41] Terry M. Tritt. *Thermal Conductivity: Theory, Properties, and Applications*. Springer Science & Business Media, May 2005. ISBN 978-0-306-48327-1. Google-Books-ID: whJNfKmziiIC.

[42] GÖRAN GRIMVALL. *CHAPTER 16 - THERMAL CONDUCTIVITY*, page 255–285. Elsevier Science B.V., 1999. ISBN 978-0-444-82794-4. doi: 10.1016/B978-044482794-4/50017-6. URL https://www.sciencedirect.com/science/article/pii/B9780444827944500176.

[43] Ananth K. Vellimana, Daniel M. Sciubba, Joseph C. Noggle, and George I. Jallo. Current Technological Advances of Bipolar Coagulation. *Operative Neurosurgery*, 64(Suppl 1):ONS11–ONS19, Mar 2009. ISSN 2332-4252, 2332-4260. doi: 10.1227/01.NEU.0000335644.57481.97.

[44] Behrouz Abedian and Kenneth Baker. Temperature effects on the electrical conductivity of dielectric liquids. *IEEE Transactions on Dielectrics and Electrical Insulation*, 15(3):888–892, Jun 2008. ISSN 1070-9878. doi: 10.1109/TDEI.2008.4543127.

[45] Jay Tu and Nicolas Reeves. Feasibility study of microneedle fabrication from a thin nitinol wire using a cw single-mode fiber laser. *Open Engineering*, 9:167–177, Jun 2019. doi: 10.1515/eng-2019-0023.

[46] Kenneth M Ralls, Thomas H Courtney, and John Wulff. *Introduction to materials science and engineering*, volume 688. Wiley New York, 1976.

[47] William D. Callister. *Materials science and engineering: an introduction*. Wiley & Suns, 5th ed edition, 2000. ISBN 978-0-471-32013-5.

[48] Malcolm Keith Stanford. *Thermophysical properties of 60-nitinol for mechanical component applications*. National Aeronautics and Space Administration, Glenn Research Center, 2012.

[49] Roberto C. Dante. *9 - Metals*, page 123–134. Woodhead Publishing, Jan 2016. ISBN 978-0-08-100619-1. doi: 10.1016/B978-0-08-100619-1.00009-2. URL https://www.sciencedirect.com/science/article/pii/B9780081006191000092.

[50] Susan Roweton, Beth Johnson, Julie Kurtenbach, G. Young, and J. Dunne. Comparison of Two Histological Test Methods for the Measurement of Thermal Spread Associated With Energized Vessel Sealing. *Journal of Testing and Evaluation*, 44:20140233, May 2016. doi: 10.1520/JTE20140233.

[51] M. Shiwa and T. Kishi. *NDT-based Assessment of Damage: An Overview*, page 1–8. Elsevier, Jan 2005. ISBN 978-0-08-043152-9. doi: 10.1016/B0-08-043152-6/02032-5. URL https://www.sciencedirect.com/science/article/pii/B0080431526020325.

[52] P. A. Campbell, A. B. Cresswell, T. G. Frank, and A. Cuschieri. Real-time thermography during energized vessel sealing and dissection. *Surgical Endoscopy*, 17 (10):1640–1645, Oct 2003. ISSN 0930-2794, 1432-2218. doi: 10.1007/s00464-002-8781-2.

[53] Robert Dodde, Albert Shih, and Arnold P. Advincula. A novel technique for demonstrating the real-time subsurface tissue thermal profile of two energized surgical instruments. *Journal of Minimally Invasive Gynecology*, 16(5):599–603, Sep 2009. ISSN 1553-4650. doi: 10.1016/j.jmig.2009.05.018.

[54] C. Crean, C. Mcgeouge, and R. O'kennedy. *11 - Wearable biosensors for medical applications*, page 301–330. Woodhead Publishing Series in Biomaterials. Woodhead Publishing, Jan 2012. ISBN 978-1-84569-935-2. doi: 10.1533/9780857097187.2.301. URL https://www.sciencedirect.com/science/article/pii/B9781845699352500115.

[55] KAI Siren, GUNNAR Rosén, JÁNOS Vad, and PETER V. Nielsen. *12 - EXPERIMENTAL TECHNIQUES*, page 1105–1195. Academic Press, Jan 2001. ISBN 978-0-12-289676-7. doi: 10.1016/B978-012289676-7/50015-1. URL https://www.sciencedirect.com/science/article/pii/B9780122896767500151.

[56] Peter Kleinhenz and Christine Vogdes. ELECTRONICS : Comparing Insulating Materials for Electrosurgical Instruments, Feb 1996. URL https://www.mddionline.com/news/electronics-comparing-insulating-materials-electrosurgical-instruments. Accessed: Apr. 30, 2021.

[57] Dipak K. Sarkar. *Chapter 2 - Steam Generators*, page 39–89. Elsevier, Jan 2015. ISBN 978-0-12-801575-9. doi: 10.1016/B978-0-12-801575-9.00002-0. URL https://www.sciencedirect.com/science/article/pii/B9780128015759000020.

[58] T. G. Vancaillie. Active electrode monitoring. *Surgical Endoscopy*, 12(8):1009–1012, Aug 1998. ISSN 1432-2218. doi: 10.1007/s004649900769.

[59] Ibrahim Alkatout, Thoralf Schollmeyer, Nusrat A. Hawaldar, Nidhi Sharma, and Liselotte Mettler. Principles and Safety Measures of Electrosurgery in Laparoscopy. *JSLS : Journal of the Society of Laparoendoscopic Surgeons*, 16(1):130–139, 2012. ISSN 1086-8089. doi: 10.4293/108680812X13291597716348.

[60] George Vilos, Kim Latendresse, and Bing Siang Gan. Electrophysical properties of electrosurgery and capacitive induced current. *The American Journal of Surgery*, 182(3):222–225, Sep 2001. ISSN 0002-9610. doi: 10.1016/S0002-9610(01)00712-7.

[61] Oleg D. Neikov, Stanislav S. Naboychenko, and Irina B. Murashova. *Chapter 19 - Production of Copper and Copper Alloy Powders*, page 571–614. Elsevier, second edition edition, 2019. ISBN 978-0-08-100543-9. doi: https://doi.org/10.1016/B978-0-08-100543-9.00019-1. URL https://www.sciencedirect.com/science/article/pii/B9780081005439000191.

[62] David C. Auth. Non-sticking electrocautery system and forceps, Jan 1985. URL https://patents.google.com/patent/US4492231A/en. US Patent 5,196,009.

[63] Yong H. Zhu, Wolff M. Kirsch, and Zhen-Sheng Tang. Endoscopic bipolar coagulation device, Jun 1995. URL https://patents.google.com/patent/US5423814A/en. US Patent 5,423,814.

[64] Jonathan O. Thorne. Non-stick electrosurgical forceps, Mar 2001. URL https://patents.google.com/patent/WO2001015615A1/en. WO Patent 01/15615 A1.

[65] ATC Semitec. Semitec F-micro Miniature Temperature Sensors, n.d. URL https://atcsemitec.co.uk/product/f-micro-miniature-temp-sensor/. Accessed: May. 31, 2021.

[66] Nordson MEDICAL. PET HEAT SHRINK TUBING TECHNICAL INFORMATION, n.d. URL https://www.nordsonmedical.com/Components-and-Technologies/Heat-Shrink-Tubing/PET-Heat-Shrink-Tubing/Technical-Information/. Accessed: Aug. 5, 2021.

[67] Brooks W. McCuen and Dyson Hickingbotham. A fiberoptic diathermy tissue manipulator for use in vitreous surgery. *American Journal of Ophthalmology*, 98(6):803–804, Dec 1984. ISSN 0002-9394. doi: 10.1016/0002-9394(84)90703-7.

APPENDIX

APPENDIX A - FIRST SEARCH STRINGS

Google Scholar (publication year filter 2000-2021):
'diathermy micro-forceps'
'bipolar AND microforceps AND coagulation'
'single-shaft AND diathermy AND forceps'
'single-shaft AND bipolar AND microforceps AND coagulation'
'single-shaft AND "diathermy forceps"'
'development AND diathermy AND forceps AND 23-gauge AND coagulation'

PubMed:
'miniaturized bipolar microforceps'
'miniaturized diathermy forceps'
'23-gauge diathermy forceps' 'Microcoagulation forceps'
'23-gauge bipolar forceps'
'bipolar peeling device'
'single-shaft bipolar forceps'
'single-shaft diathermy tweezer'
'micro coagulation tweezer'
'coagulation bipolar grasper'
'coagulation AND "bipolar forceps" AND 'microsurgery'
'coagulation AND forceps AND small-size'
'small-size diathermy forceps'

Additional References

[1] Matteo Fallico et al. “Scleral Buckling: A Review of Clinical Aspects and Current Concepts”. en. In: *Journal of Clinical Medicine* 11.22 (Jan. 2022), p. 314. ISSN: 2077-0383. DOI: 10.3390/jcm11020314.